A NOVEL REMOTE SENSING SYSTEM USING REFLECTED GNSS SIGNALS

BY

ROOHOLLAH PARVIZI

Submitted in partial fulfillment of the
requirements for the degree of
Doctor of Philosophy in Mechanical and Aerospace Engineering
in the Graduate College of the
Illinois Institute of Technology

Seebany Datta-Barua

Digitally signed by Seebany Datta-Barua
DN: cn=Seebany Datta-Barua, o=Illinois Institute of Technology, ou, email=sdattaba@iit.edu, c=US
Date: 2020.07.17 11:00:16 -06'00'

Approved ______________________
Advisor

Chicago, Illinois
July 2020

ACKNOWLEDGMENT

It has been a long journey and many people have supported me to reach the point where I am standing now. I humbly thank all of them for their help and support. My advisor, Professor Seebany Datta-Barua, I thank her for providing me both the opportunity to join the Space Weather Lab at IIT, especially the GNSS-R group, and for allowing me the intellectual freedom to investigate an area of interest that borders other fields. Thanks to Professors Boris S. Pervan, Geoffrey Williamson, and Ankit Srivastava for serving on my defense committee. I am also grateful to Professor Pervan for providing insights, giving me access to NavLab instruments and for reviewing this dissertation.

Thanks in particular to the GNSS-R group: Norikazu Honda, Erik Donarski, James Henry, Houshine Sabbagh Zadeh, Kierra Herron, Ander Rangil Nieto, Li Pan, and Shahrukh Khan for their help in data campaigns, data processing and hardware setup during tests. I also thank former and current space-weather lab members Ningchao Wang, David Stuart, Aurora Lopez, Vaishnavi Sreenivash, and Yang Su for their help during the data campaign during the tough and extreme weather conditions. They have helped and supported me to improve the quality of my research work. The friendships that we forged in our most challenging times will always remain throughout our future endeavors.

Thanks to Cagatay Tanil, for his support and friendship. Thanks to Setfan Stevanovic for helping and advising about the USRP setup.

Great thanks to my parents Rezayat Parvizi and Fatemeh Soghra Hejazi. I am grateful beyond words for all the personal sacrifices they have so willingly made in order to encourage me to strive and to make so many opportunities available to me. I truly appreciate your support and endless love. I am greatly indebted to you. Also, special thanks for my father and mother in law, Hassan and Nahid Esmaeilpour

for your support, patience, love and compassion.

I thank my brothers Mojtaba Parvizi and Mahdi Parvizi and my sister Fatemeh Parvizi for their years of love and understanding, and wish them all the best in their lives.

Special thanks to Sepideh, my beautiful, lovely wife. This could not be done and accomplished without your patience and support. Thank you for understanding me and loving me. I am grateful for being with you.

Thanks to the Chicago Park District for providing the Research Access Permit for all field tests. This work was funded by the National Aeronautics and Space Administration (NASA) award NNX15AV01G.

TABLE OF CONTENTS

Page

ACKNOWLEDGEMENT iii

LIST OF TABLES vii

LIST OF FIGURES xiii

ABSTRACT xiv

CHAPTER

1. INTRODUCTION 1
   - 1.1. Overview 1
   - 1.2. Previous work in GNSS Reflectometry 4
   - 1.3. Contributions 6

2. BACKGROUND 11
   - 2.1. Overview 11
   - 2.2. GNSS signal 11
   - 2.3. GNSS receiver 13
   - 2.4. GNSS front-end 13
   - 2.5. GPS signal acquisition 15
   - 2.6. Reflected GPS signal characteristics 23

3. SENSOR SYSTEM DESIGN AND FABRICATION 28
   - 3.1. Overview 28
   - 3.2. Single USRP 30
   - 3.3. Dual-USRP configuration 47
   - 3.4. USRP GPS-disciplined oscillator (GPSDO) 51
   - 3.5. Auxiliary sensors 52

4. FIELD TESTS 54
   - 4.1. Overview 54
   - 4.2. Data Campaign 1 55
   - 4.3. Data Campaign 2 57
   - 4.4. Data Campaign 3 58
   - 4.5. Data Campaign 4 58
   - 4.6. Data Campaign 5 59
   - 4.7. Data Campaign 6 60
   - 4.8. Data Campaign 7 61
   - 4.9. Data Campaign 8 62

- 4.10. Data Campaign 9 62
- 4.11. Data Campaign 10 64
- 4.12. Data Campaign 11 64

5. NEW SIGNAL PROCESSING METHOD FOR ACQUISITION . 78

- 5.1. Overview 78
- 5.2. Proposed acquisition method 79
- 5.3. Signal acquisition methods evaluated 82
- 5.4. Experimental evaluation 89
- 5.5. Results 91
- 5.6. Conclusion 98

6. EVALUATION OF GNSS-R USING AUXILIARY SENSORS . . 103

- 6.1. Overview 103
- 6.2. Method for comparison of GNSS-R power to surface type . 105
- 6.3. Data Campaign 8 (Location B) ice analysis 107
- 6.4. Data Campaign 11 mixed ice-and-water analysis 113

7. CONCLUSION 124

- 7.1. Summary 124
- 7.2. Future Work 127

APPENDIX 130

A. SPECULAR POINT POSITION 130

B. SURFACE REFLECTIVITY (SR) COMPUTATION 134

C. POINT CLOUD PROCESSING 138

BIBLIOGRAPHY 141

LIST OF TABLES

Table Page

3.1 RF gain requirement experimental tests of USRPs in the lab. . . . 42

3.2 Low pass filters tested. 43

3.3 Configurations in which low pass filters are studied. All filters are implemented with MATLAB built-in functions. 43

3.4 USRP gain configurations for each IIT baseball field experiment. . . 44

3.5 Signal acquisition results for five low-pass filters, with 6 different configurations each, that are applied to the experiment II data. N and $R = l^{q}_{\hat{f}_D}$ stand for number of acquired satellites and the acquisition meteoric (Eq. 2.3), respectively. 45

4.1 Lake Michigan data collection campaign information Test 1. 67

4.2 Lake Michigan data collection campaign information Test 2 68

4.3 Lake Michigan data collection campaign information Test 3. 69

4.4 Lake Michigan data collection campaign information Test 4. 70

4.5 Lake Michigan data collection campaign information Test 5. 71

4.6 Lake Michigan data collection campaign information Test 6. 72

4.7 Lake Michigan data collection campaign information Test 7 73

4.8 Lake Michigan data collection campaign information for Data campaign 8 for both locations (A and B). 74

4.9 Lake Michigan data collection campaign information Test 9 75

4.10 Lake Michigan data collection campaign information Test 10 76

4.11 Lake Michigan data collection campaign information Test 11 77

5.1 Signal acquisition methods compared. 83

5.2 Results of Comparisons 1-3 using the direct GPS signal. 101

5.3 Results of Comparisons 4-5 using the reflected GPS signal. 102

B.1 Gain lost of the reflected antenna based on the Phi angle 137

LIST OF FIGURES

Figure Page

1.1 A Global Navigation Satellite System (GNSS) is a constellation of satellites (space segment) and users (ground segment). Image credit [3]. 1

1.2 How GNSS helps a user on Earth use to compute position. 2

1.3 GNSS reflected signals are a remote sensing source for study of Earth's environment. The properties of the reflected signal received depend in part on the surface which they are reflected. 3

1.4 MODIS instrument satellite image of Lake Michigan on 8 March 2014 [4] 4

1.5 The conceptual objective of this work is the hardware and software design and use of a GNSS-R system to receive signals reflected from surface ice and water. 7

2.1 GPS L1 signal structure. Image modified from [5]. 12

2.2 GNSS receiver block diagram as implemented in this work. 14

2.3 GPS signal acquisition process. To detect the GPS signal, the incoming C/A code is correlated with a receiver-generated replica of the C/A code. For a visible satellite the correlation output has a triangle shape. 15

2.4 Correlation of a real GPS signal, M_1 is the primary peak and M_2 is secondary peak. 16

2.5 Example of the acquired GPS signal (visible satellite) (left) and not acquired (invisible satellite) (right). 17

2.6 Correlation process of the GPS signal. 19

2.7 illustration defining the specular point at which α_r quals β_i and the glistening zone. 24

2.8 Iso-range ellipsoids (black) and iso-Doppler hyperbolas (red). . . . 25

2.9 Relation between the spatial and Delay Doppler domain. 25

3.1 Schematic of the GNSS-R sensor system. 28

3.2 USRP N210 Hardware. 31

3.3 USRP in-lab testing configuration. A simulated noise-free GPS L1 signal is input as sample data. A static roof-mounted GPS antenna is used for the GPSDO timing reference. 32

3.4 Initial data processing flow from the USRP output to the SDR. The SDR flowchart is inside the red box. 34

3.5 USRP test configuration with a simulator for various RF gains. . . 35

3.6 Sample data in time domain (top left); frequency domain (top right); histogram of the digitized samples (bottom). Parameters are: sample rate=10 MHz and gain=5 dB. 36

3.7 Time series of USRP sample data over the initial 0.06 seconds of the data-set. 37

3.8 USRP data after truncating the first 0.06 seconds. 37

3.9 Data input to the SDR after truncating the first two seconds, in the time domain (top left); frequency domain (top right); histogram of the digitized samples (bottom). Parameters are: sample rate=10 MHz, gain=5 dB. 38

3.10 Updated data process before input to the SDR. 39

3.11 Test configuration to study USRPs with various GPS signal power to determine in-line gain requirements. 40

3.12 Time domain, frequency domain, and histogram of the samples for RF gain test 4: (left subplots) USRP with 0 dB RF gain. (right subplots) USRP with 31 dB RF gain. The test is conducted with a simulated GPS noise-free signal with -95 dBW input power. . . . 40

3.13 Signal acquisition results for RF gain test 4: (left) USRP with 0 dB RF gain. (right) USRP with 31 dB RF gain ([52]). 41

3.14 Left: Google Map satellite image of sensor location for the field test. The white cross indicates sensor location. Right: Photo of the experiment hardware setup, with distances notated. 44

3.15 Time domain; frequency domain and histogram of the samples of experiment II (RF gain= 0 dB, GPS in-line gain = 30 dB) before (left) and after Chebyshev filtering (right). 45

3.16 Signal acquisition results for experiment II (RF gain= 0 dB, GPS inline gain = 30 dB) before (left) and after filtering (right). After filtering, two more satellites are acquired. 46

3.17 Frequency Response of the designed low pass filter 46

3.18 Final Signal preconditioning process before feeding to the SDR . . 47

3.19 Dual-USRP system using a MIMO cable with a primary and secondary USRP. 48

3.20 Dual-USRP System using a gigabit ethernet switch. 48

3.21 Dual USRP System set up for testing with simulator. Facilities provided by the NavLab at IIT. 49

3.22 Screen capture of buffer overflow indication error, which occurs when the write-to-medium rate drops below 20 MB/s. 50

3.23 Dual-USRP system using a MIMO cable with GPSDO internal clocks. 50

3.24 Dual-USRP system using a gigabit ethernet switch with GPSDO internal clocks. 51

4.1 Google Map of all data campaign locations at Lake Michigan. [33] 54

4.2 Schematic of sensor mounting system and relevant coordinate systems. Left: view from the side. Right: View from above. 55

4.3 Left: Photo of the experiment hardware setup for Test 1-East. Right: Google Map satellite image of sensor location for Test 1-East. The yellow arrow describes the boom direction $\hat{b}$. 56

4.4 Left: Photo of the experiment hardware setup for Test 1-West. Right: Google Map satellite image of sensor location for Test 1-West. The yellow arrow describes the boom direction $\hat{b}$. 56

4.5 Schematic of sensor mounting system and relevant coordinate systems. (Above) Side view. (Below) Top view. 59

4.6 Left: Photo of the experiment hardware setup for Test 5. Right: Google Map satellite image of sensor location for Test 5. The yellow arrow describes the boom direction $\hat{b}$. 60

4.7 Left: Photo of the experiment hardware setup for Test 6. Right: Google Map satellite image of sensor location for Test 6. The yellow arrow describes the boom direction $\hat{b}$. 61

4.8 Left: Photo of the experiment hardware setup for Test 7. Right: Google Map satellite image of sensor location for Test 7. The yellow arrow describes the boom direction $\hat{b}$. 62

4.9 Left: Photo of the experiment hardware setup for Test 8 Location A. Right: Google Map satellite image of sensor location for Test 8 Location A. The yellow arrow describes the boom direction $\hat{b}$. . . 63

4.10 Left: Photo of the experiment hardware setup for Test 8 Location B. Right: Google Map satellite image of sensor location for Test 8 Location B. The yellow arrow describes the boom direction $\hat{b}$. . . . 63

4.11 Left: Photo of the experiment hardware setup for Test 9. Right: Google Map satellite image of sensor location for Test 9. The yellow arrow describes the boom direction $\hat{b}$. 64

4.12 Sensor system schematic with three cameras. 65

4.13 Left: Photo of the experiment hardware setup for Test 10. Right: Google Map satellite image of sensor location for Test 10. The yellow arrow describes the boom direction $\hat{b}$. 65

4.14 Left: Photo of the experiment hardware setup for Test 11. Right: Google Map satellite image of sensor location for Test 11. The yellow arrow describes the boom direction $\hat{b}$. 66

5.1 Illustration of the auto-correlation function before (a) and after (b) the proposed method (MDI). 80

5.2 Comparison between (a) coherent integration, (b) conventional differential integration, and (c) modified differential integration. . . . 81

5.3 Coherent integration via Fast Fourier Transform (Method 1) . . . 84

5.4 Standard incoherent detection (Method 2) 86

5.5 Conventional differential coherent integration (Method 3) 88

5.6 “Modified Differential” correlator tested in this work. 89

5.7 Visible satellite list and sky plot at the time of the data analyzed. 90

5.8 Comparison 1 result: acquisition metric for methods 1-4 using $T_1 = T_2 = 2$ ms of direct signal data. 91

5.9 Comparison 2 result: acquisition metric for methods 1-4 using $T_1 = T_2 = 10$ ms of direct signal data. 93

5.10 Test 3 result: acquisition metric for methods 1 and 4 using $T_d = T_1 = 1$ ms of direct signal data. 94

5.11 Test 5 result: acquisition metric for methods 4 using $T_1 = T_2 = 10$ ms of reflected signal data. 96

5.12 Auto-correlation of PRN 16 for the reflected signal. 97

5.13 Auto-correlation of PRN 27 for the reflected signal. 98

5.14 Auto-correlation of PRN 07 for the reflected signal. 99

6.1 Cartoon of a surface with SPs (red) from satellites 1 to n scattering power toward the reflected antenna. 103

6.2 Flowchart describing the process by which the surface type for a reflecting satellite is verified and the satellite selected for analysis, followed by computation of the GNSS reflected signals' characteristics for the selected satellite (SV). 105

6.3 Sky plot for Data Campaign 8 (Location B). 107

6.4 Scatter plot of sensor position estimated with GPS L1 direct antenna data for Data Campaign 8 (Location B) relative to average position (red). 108

6.5 SP-lidar-camera map in ENU coordinates with origin at the reflected antenna. The green cross marks the reflected antenna position, SPs are blue circles, lidar point cloud is yellow dots, and camera pixels are projected in the trapezoidal area. 109

6.6 Delay Doppler Map of PRN 07 of reflected signals 110

6.7 MDI Auto-correlation of the PRN 07 of reflected signal (right) 5. . 111

6.8 Signal-to-noise ratio (SNR) of PRN 07 from Data Campaign 8 (Location B) of reflected signal for 1 second. 112

6.9 Surface reflectivity (SR) of PRN 07 from Data Campaign 8 (Location B) of reflected signal for 1 second. 113

6.10 Yuma almanac-based sky plot at 11:58 Central Time (CT) for Data Campaign 11. 114

6.11 SP-lidar-camera maps of Data Campaign 11 at (a) 11:58 CT and (b) 12:18 CT. The Sensor origin is marked with a green cross. The Lidar point cloud is marked with orange dots. The Camera image from the central camera is projected onto the map in color. Specular points are blue labeled by satellite PRN number. 115

6.12 Signal-to-noise ratio (SNR) of PRN 16 over time, in minutes since 11:57 CT. Blue indicates times visually identified on the SP-lidar-camera map to correspond to water reflection, and red indicates times corresponding to ice reflection. 116

6.13 Surface reflectivity (SR) of PRN 16 over time, in minutes since 11:57 CT. Blue indicates times visually identified on the SP-lidar-camera map to correspond to water reflection, and red indicates times corresponding to ice reflection. 118

6.14 SP-lidar-camera maps of Data Campaign 11 at (a) 11:58 CT and (b) 12:18 CT. Sensor origin is marked with a green cross. Lidar point cloud are orange dots. Camera image from the central camera is projected onto the map in color. Specular points are blue labeled by satellite PRN number. 120

6.15 SP-lidar-camera maps of Data Campaign 11 at 13:03 CT. Sensor origin is marked with a green cross. Lidar point cloud are orange dots. Camera image from the central camera is projected onto the map in color. Specular points are blue labeled by satellite PRN number. 121

6.16 Signal-to-noise ratio (SNR) of PRN 27 over time, in minutes since 12:43 CT. Blue indicates times visually identified on the SP-lidar-camera map to correspond to water reflection, and red indicates times corresponding to ice reflection. 122

6.17 Surface reflectivity (SR) of PRN 27 over time, in minutes since 12:43 CT. Blue indicates times visually identified on the SP-lidar-camera map to correspond to water reflection, and red indicates times corresponding to ice reflection. 123

A.1 Geometry for specular point position estimation. Left: side view of the plane of propagation for the specularly reflecting ray. Right: top view of the horizontal plane and position of the satellite and SP. 131

B.1 Left: Boom coordinate system of the tripod $\hat{x}, \hat{b}, \hat{u}$. Right: the reflected antenna coordinate system $\hat{x}$, $\hat{s}$, $\hat{a}$ and definition of antenna-zenith angle ϕ. 135

C.1 Lidar processing flowchart 139

ABSTRACT

This dissertation presents a method to remotely sense freshwater surface ice and water using reflected signals from Global Navigation Satellite Systems (GNSS). A portable ground-based sensor system is designed and built for collecting both scattered Global Positioning System (GPS) signals and independent validation data (lidar and camera) from the surface. GPS front-end signals are collected from both a direct receiving antenna facing upward and from a reflection-receiving antenna facing downward. Multiple data campaigns are conducted on the Lake Michigan waterfront in Chicago.

A customized software receiver tests a new signal processing method to detect and acquire Global Navigation Satellite System (GNSS) signals reflected from the lake surface ice and collected by a downward-facing antenna. The method, modified differential coherent integration, multiplies time-shifted auto-correlation samples. The new method is evaluated against three conventional integration methods (coherent, incoherent, and differential integration) with signals from the direct antenna. With front-end samples from the reflection antenna, the new method is the only one of the four methods compared that acquires satellites in the reflected GPS signals, with three acquired using 10 ms of integration.

The lidar surface scans are mapped with camera images and estimated reflection points to indicate the surface reflection type and to provide surface height relative to the sensors. For one satellite whose specular point is estimated to be on the ice surface, a Delay Doppler Map (DDM), signal-to-noise (SNR) ratio, and surface reflectivity (SR) are computed with the modified differential coherent integration method using the GPS data collected from the downward pointing reflection antenna. The DDM shows that, with modified differential integration, the satellite can be acquired in the reflected signal.

For two satellites whose reflection points scan across ice and water over time the SNR and SR are computed over time. The SR is shown to be lower for liquid water than lake ice. This system concept may be used in the future for more complete mapping of phase changes in the cryosphere.

CHAPTER 1

INTRODUCTION

1.1 Overview

Figure 1.1. A Global Navigation Satellite System (GNSS) is a constellation of satellites (space segment) and users (ground segment). Image credit [3].

A Global Navigation Satellite System (GNSS) is a constellation of satellites that orbit earth, originally designed for providing position, navigation and timing (PNT) for users on the ground. Figure 1.1 illustrates an example GNSS constellation. Each satellite broadcasts a microwave signal; users receiving signals from multiple satellites use them to estimate position by calculating the distance, or range, from each satellite. For 3-dimensional position estimation, at least 4 satellites are required to estimate position as well as time, as in Figure 1.2.

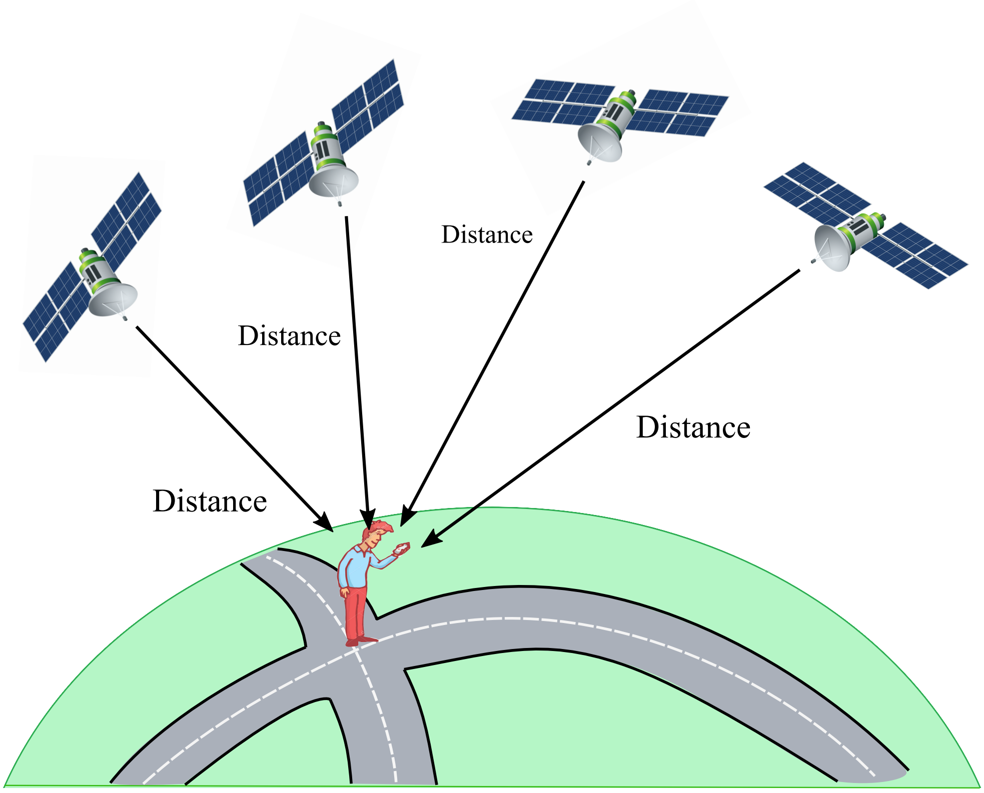

Figure 1.2. How GNSS helps a user on Earth use to compute position.

The United States (US) GNSS is known as the Global Positioning System (GPS). Used worldwide for PNT, GPS is a well-known example of GNSS. Another GNSS is GloNASS, the Russian satellite-based positioning system. GPS and GloNASS are fully operational GNSS systems at the present. In addition, China's BeiDou Navigation Satellite System (BDS) and the European Union's Galileo will be completely in service by the end of 2020 [1].

A reflected GNSS signal is often eliminated as multipath. When used for positioning, the direct and reflected signals both arrive at the receiver's antenna with different time delays (i.e., ranges) because of the additional path length (as in Figure 1.3), and therefore can increase uncertainty in the position estimate. Yet GNSS signals' global coverage and widespread availability make them a potentially exceptional source for remotely sensing Earth's environment, possibly at lower cost than other surface sensing devices. GNSS reflectometry (GNSS-R) is the study of the characteristics of a reflected signal to infer properties of the surface from which it reflects. In particular, liquid water and ice have been shown to return detectable reflected signals in the past [14][26][41][67]. A GNSS-R system remotely sensing surface water versus ice conditions can be useful for coastal or climate monitoring, particularly in inaccessible regions of the world.

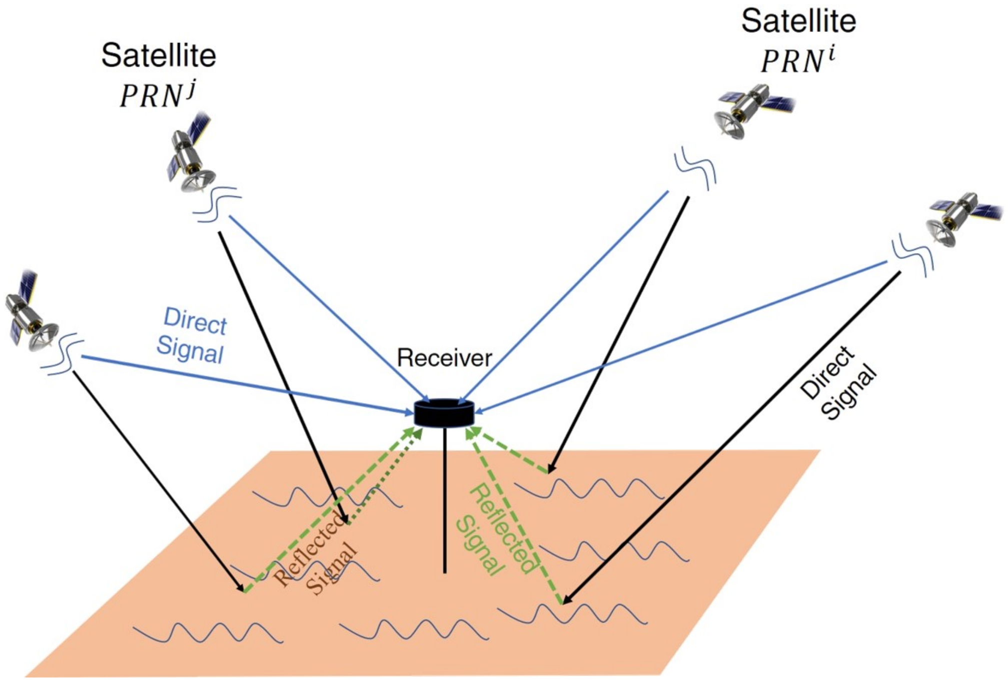

Figure 1.3. GNSS reflected signals are a remote sensing source for study of Earth's environment. The properties of the reflected signal received depend in part on the surface which they are reflected.

Existing ice and water measurement systems include optical and thermal band imaging such as that of the Moderate-resolution Imaging Spectroradiometer (MODIS) on the Terra and Aqua satellites. Figure 1.4 is a MODIS visible satellite image of Lake Michigan that was taken on 8 March 2014. In this picture, the lake surface is partly obscured by clouds, making it difficult to distinguish between ice and water on the lake surface. Also, these instruments provide imaging coverage of Earth's water resources, but the pixel width is 250 m. The optical bands are used only in

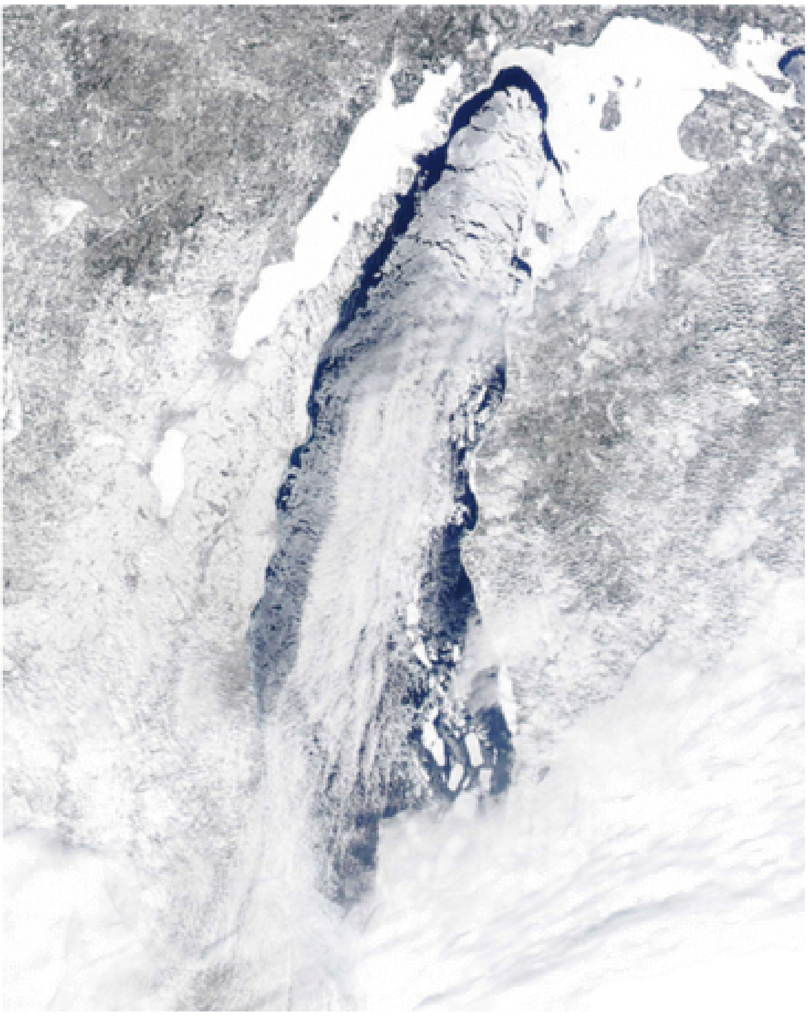

Figure 1.4. MODIS instrument satellite image of Lake Michigan on 8 March 2014 [4]

daytime and limited to cloud-free conditions [24][56]. GNSS-R has the potential to be a complementary data source with the advantages of lower cost, the possibility for widespread coverage and availability at better resolution, operating day and night, not limited by cloud cover or precipitation.

1.2 Previous work in GNSS Reflectometry

GNSS-R is a form of bistatic radar whose concept dates back to Martin-Neira [41]. GNSS-R uses scatterometry, measurement of a scattered signal, to determine the surface properties of the reflecting surface [25]. GNSS-R has been explored with ground [23][37], airborne [50][59], and most recently, space-borne platforms such as TechDemoSat-1 and CYclone GNSS (CYGNSS) [13][28][59] for the receiver.

An existing reflectometry technique for cryospheric sensing is based on using a single zenith antenna for GNSS interferometric reflectometry (GNSS-IR). Such methods use variations in the signal-to-noise ratio of low-elevation satellites as a direct and reflected signal constructively and destructively interfere when both are received at the antenna [36][38]. GNSS-IR typically uses commercial off-the-shelf receivers. The SNR interference patterns have a simple relationship to the surface height in the vicinity of the antenna, changing as snow accumulates. The method is also sensitive to firn density using the vertical coordinates. The GNSS-IR method has been used for re-analyses of historic data, and has shown that surface heights in Antarctica can be accurately measured at about 2 cm over months and years [54][55] . GNSS-IR is useful for year-long records of changes to the surface.

However, as changes occur seasonally or faster, and for more challenging terrain, a separate antenna to collecting the reflected signal may provide higher spatial and temporal resolution. A two-antenna system for sensing wet vs. dry snow has recently been tested in a high-alpine environment using commercially available receivers [34]. Two-antenna GNSS-R receiver systems such as GOLD-RTR have also been developed and deployed for sea ice and dry snow altimetry using measurement of polarization [22][23]. Some receiver designs have used software receivers [32], again using interferometry for altimetry [49]. Separately from altimetry, an important feature to be able to sense is melt-water on the surface of snow/ice. It may occur as a result of differential heating and ablation. [40] reviewed seismologic signatures of firn layers and the importance of melt-water in the seismological response. [11][35] proposed that dielectric variations would result in scattered intensity variations. [61] developed theory and simulations of different surface and subsurface dielectric scattering.

To overcome power losses due to scatter, a dedicated GNSS-R receiver designed to measure the reflected signals needs more advanced signal processing than typical methods used for a directly received GNSS signal [64]. Normally, coherent and/or incoherent detection are widely used in conventional receivers to increase the signal-to-noise ratio of Global Positioning System (GPS) signals for acquisition and tracking [7][43][58][63]. Whether for navigation in challenging environments or for remote sensing, detecting the reflected GNSS signal in order to study its properties can be challenging [27][29][39].

1.3 Contributions

In this research we want to answer the question, “Can we distinguish surface ice from water with a dedicated downward-facing GNSS receiver?” To answer this question, we need to know:

1. What sensors are needed to collect the GNSS-R signals?
2. Where and when should we collect the relevant data?
3. Can existing baseline methods detect reflected GNSS signals? If not, what method can do so?
4. Are the received GNSS-R signals reflected from an ice surface or they are reflected from a water surface?

Figure 1.5 shows the objective of this work, which is to design a sensor system, deploy it at a site with mixed surface conditions, and analyze the reflected GNSS signals for various surface conditions (i.e., ice and water).

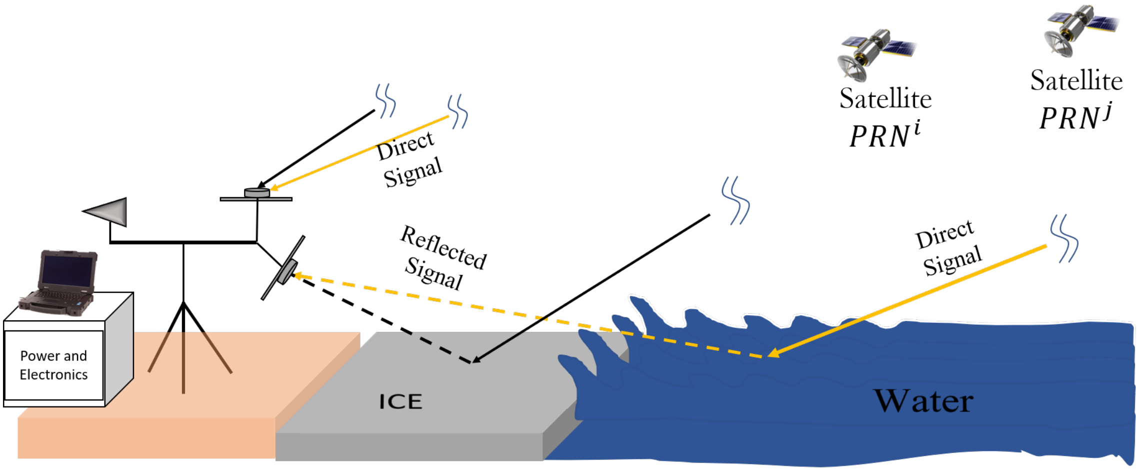

Figure 1.5. The conceptual objective of this work is the hardware and software design and use of a GNSS-R system to receive signals reflected from surface ice and water.

To develop GNSS-R as an ice and water surface discriminator, this work makes the following contributions:

1. **Sensor system design and fabrication.** A set of sensors is grouped to collect direct and reflected GNSS-R signals (Figure 1.5). These sensors are collocated with independent sensors that provide reference evidence of the surface type.
2. **Sensor system field deployment.** Eleven field tests are conducted at the Lake Michigan shore. Data collection campaigns are carried out during different seasons of the year. GNSS-R power characteristics, such as signal-to-noise ratio, surface reflectivity, and Delay Doppler Maps (DDMs) are generated.
3. **New signal processing method for acquisition.** To detect the reflected GNSS signal, a new signal processing method is introduced in this work. The method, modified differential integration (MDI), is defined and evaluated in comparison to previously developed methods: coherent, incoherent and differential coherent integration. To assess MDI, directed and reflected GPS signals

that were collected during the data campaigns (contribution 2) are used.

4. **Analysis of surface-reflected GNSS signals.** The GNSS-R signals are evaluated using the auxiliary sensors. The data collected from other sensors, a camera and a lidar, is used to identify the surface type. The signals of satellites whose reflection points are on a particular surface type are analyzed. Specifically, the signal-to-noise ratio, surface reflectivity, and Delay Doppler Map are computed.

The next subsections describe each of these contributions in more detail.

1.3.1 Sensor system design and fabrication. Our sensor suite includes two antennas, two universal software radio peripherals, a lidar, a camera, weather station, and supporting electronics. GNSS antennas with right hand circular polarization for direct signals and left hand circular polarization for reflected signals are used, respectively. Universal software radio peripherals (USRPs) play the role of the front-end receiver for GNSS signals. One USRP for direct signals (USRP-dir) and the other one for reflected GNSS signals (USRP-ref) are used. The lidar and camera are collocated with USRPs as auxiliary parts of the sensor suite.

1.3.2 Sensor system field deployment. To study GNSS-R signals from differing water phases, data campaigns are conducted at a freshwater site with seasonal ice formation. Eleven data campaigns are conducted at the shore of Lake Michigan at 31st Street, Chicago, Illinois, for different surface conditions during various seasons in years 2018-2020. Sensor position and attitude, gain and sampling configuration, and lake surface condition, are recorded for each campaign. Each test collects data from one or more of the instruments: two GNSS receivers, lidar, camera, and weather station. In data campaigns 1-4, sensor components are tested, and the system design is tested and updated progressively. Each test experience helps improve the sensor design and configuration. Campaigns 5-8 are used for gathering data from the complete system for analysis. We learn from campaigns 5-8 that the single camera covers an insufficient field of view, so two more cameras are added to the system for data campaigns 9-11. In Data Campaign 9, three cameras are set up and tested for sufficient data rate, power consumption and no buffer overflows. In data campaigns 10 and 11, a heterogeneous ice and water surface is sensed with the three-camera GNSS-R system design.

1.3.3 New signal processing method for acquisition.

Conventional acquisition methods are found to be insufficient to consistently acquire reflected GNSS signals from the field campaigns. In order to detect the GNSS-R signals, a new signal processing method is presented in this work. This new signal processing method, modified differential integration (MDI), is studied alongside established signal processing methods for detecting GNSS signals: coherent integration, incoherent detection, and differential coherent integration. The direct GNSS and reflected GNSS signals that are collected during the Lake Michigan data campaigns are used for this study. First, the direct GNSS signals are used to compare each method's signal acquisition performance. The visible satellites are determined using the approximate sensor position and almanac information. Then, the same methods are compared for the reflected GNSS signals.

1.3.4 Analysis of surface-reflected GNSS signals.

The reflected signal properties are computed for two surface types (water or ice) using GNSS reflected signals. To estimate the surface type from which the signal reflects, a map of the lidar and camera data with estimated GPS signal reflection points is created. This map indicates the position of the GNSS reflection point on the surfaces, which is determined to be water or ice by visual inspection of the lidar and camera data. Next, a satellite whose reflection point is established to be on an ice surface is selected for computation of GNSS-R power characteristics: signal-to-noise ratio (SNR), surface reflectivity, and a Delay Doppler Map (DDM). For a data campaign during which the surface contained a mixture of water and ice, two satellites are selected whose reflection path scans over alternately ice and water over time. The SNR and SR are computed for these satellites. The SR over time is shown to be lower for water than ice at L-band, although the distinction is not as clear when the area from which the signal reflects contains a mixture of both water and ice. The sensor system can be applied for future cryospheric mapping.

CHAPTER 2

BACKGROUND

2.1 Overview

This chapter reviews some of the important concepts used in this work. To give a better understanding of GNSS reflectometry signal processing, the GPS signal structure is introduced. Then the basic signal processing to acquire the GNSS signal is reviewed. In addition to signal acquisition, quantities derivable from the GNSS reflected signals that are used in this work are discussed. Section 2.2 reviews the GNSS signal structure. Section 2.3 gives an overview of GNSS receivers. Section 2.4 describes the front-end processing step of a receiver. Section 2.5 discusses GPS signal acquisition processing and existing signal processing methods to detect a weak GPS signal. Finally, Section 2.6 explores important GNSS-R properties, such as the specular point (SP), Delay Doppler Map (DDM), signal-to-noise ratio (SNR), and Surface Reflectivity (SR) to be investigated for ice and for water.

2.2 GNSS signal

The GPS legacy signals are spread-spectrum broadcasts transmitted at two different frequencies L1 (civilian and military use) and L2 (military only). As new satellites replace older generations, new signals at L1C, L2C and L5 are being broadcast for civil use. In this work we focus on the GPS legacy civilian code at L1 frequency $f_{L1} = 1575.42$ MHz. The carrier sinusoid is modulated with a coarse-acquisition (C/A) code and with navigation data bits. Figure 2.1 illustrates the GPS L1 signal structure and modulation.

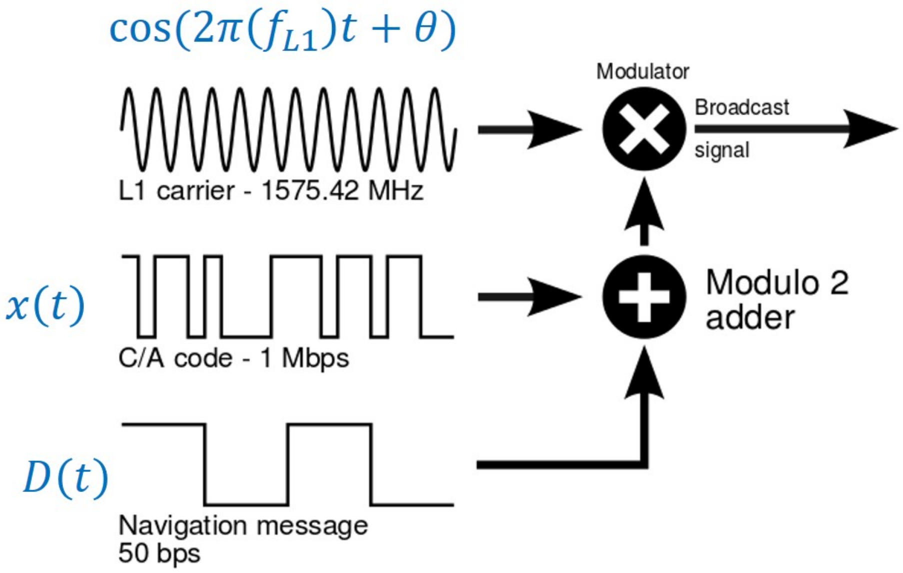

Figure 2.1. GPS L1 signal structure. Image modified from [5].

From the qth satellite, the signal arrives at the antenna as s^q_{L1}:

$$s^q_{L1}(t) = \sqrt{2P_C}D^q(t-\tau')x^q(t-\tau')\cos(2\pi(f_{L1}+f'_D)t+\theta_{L1}) + w^q_{L1}(t) \tag{2.1}$$

where P_C is the average signal power, D^q is the navigation data, x^q is the C/A code for the qth satellite, τ' is the GPS signal delay (arrival time), f'_D is the Doppler frequency shift due to the relative motion between the satellite and the receiver (and for reflected signals, the scatterer also), θ_{L1} is the phase offset, and w^q_{L1} is noise. The C/A code x^q for the qth satellite is a known pseudorandom noise (PRN) sequence. Each satellite is assigned its own PRN code, to differentiate it from the others [43]. Each PRN code is made of 1023 rectangular pulse "chips" of duration T_c, and the full sequence of chips repeats every $T_{C/A} = 1$ ms. The navigation data is also a sequence of rectangular pulses transmitted at 50 bits per second with 20 ms of bit duration. The navigation data contain the satellite health status, ephemerides for computing satellite position and velocity, clock bias and ionospheric correction parameters, and satellite almanac information [43] [58].

2.3 GNSS receiver

All GNSS receivers execute a sequence of steps to produce a position solution from the signals that arrive at the antenna in the form of Eq. (2.1). They may be performed with off-the-shelf receivers equipped with application-specific integrated circuits. In this work, the functions are performed with a combination of a universal software radio peripheral (USRP) and a software-defined receiver (SDR). Figure 2.2 describes the roles of the USRP and SDR in position estimation. Universal software radio peripherals (USRPs) serve as the receiver front-ends. GNSS signals are digitized and downconverted in the USRP. USRP outputs are discussed in chapter 3. Separate USRPs are used for each of a direct antenna and a reflection antenna. The SDR is an open source platform introduced in [8] that provides the user the ability to construct reconfigurable GNSS receivers. The explicit description of SDR functions used for the direct antenna in this dissertation can be found in chapter 3 of [8]. The SDR outputs a position solution as well as satellite elevation and azimuth. The following subsections review each of the functional steps of a general GNSS receiver.

2.4 GNSS front-end

When GPS signals arrive at the antenna: 1) the power of the GPS signals is low and needs to be amplified, 2) there is natural thermal noise on GPS signals that needs to be removed, 3) it is difficult for computers to cope with the high carrier frequency that GPS signals have, so the frequency must be down converted to practical levels, and 4) the incoming analog signal needs to be digitized for computation. The GNSS front-end performs these steps (circled in green in Figure 2.2). The front end of a receiver first downsamples the signal s^q_{L1} to an intermediate frequency $f_{IF} = f_s/2$, half the receiver's sampling rate f_s, and digitizes it. Dropping the superscript q for

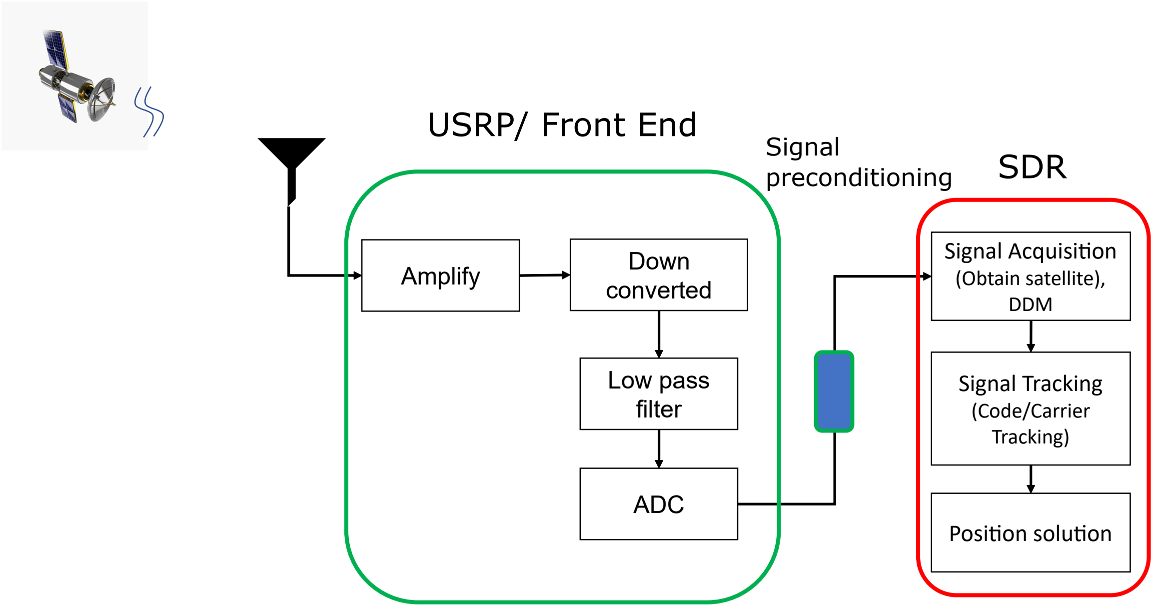

Figure 2.2. GNSS receiver block diagram as implemented in this work.

brevity gives [17]:

$$s_{IF}(nT_s) = P_s D(nT_s - m'T_s)x(nT_s - m'T_s)\cos\left(2\pi(f_{IF} + f'_D)nT_s + \theta_{L1}\right) + w_{IF}(nT_s) \tag{2.2}$$

where P_s is the digitized received power, $T_s = f_s^{-1}$ is the sampling period, n is the sample number, m' is the unknown integer to which code delay corresponds, and w_{IF} is multipath and thermal noise. Digitizing transforms $t \to nT_s$ and $\tau' \to m'T_s$. After discretized values are obtained, the arrival time τ' must be estimated to determine the range from the satellite to the user. To calculate the user's velocity, we need to estimate the Doppler frequency f_D containing the pseudorange rate. The process that estimates τ' and f_D is called signal acquisition. For high precision, the carrier phase, θ_{L1}, may be computed and tracked, a process known as signal tracking[43].

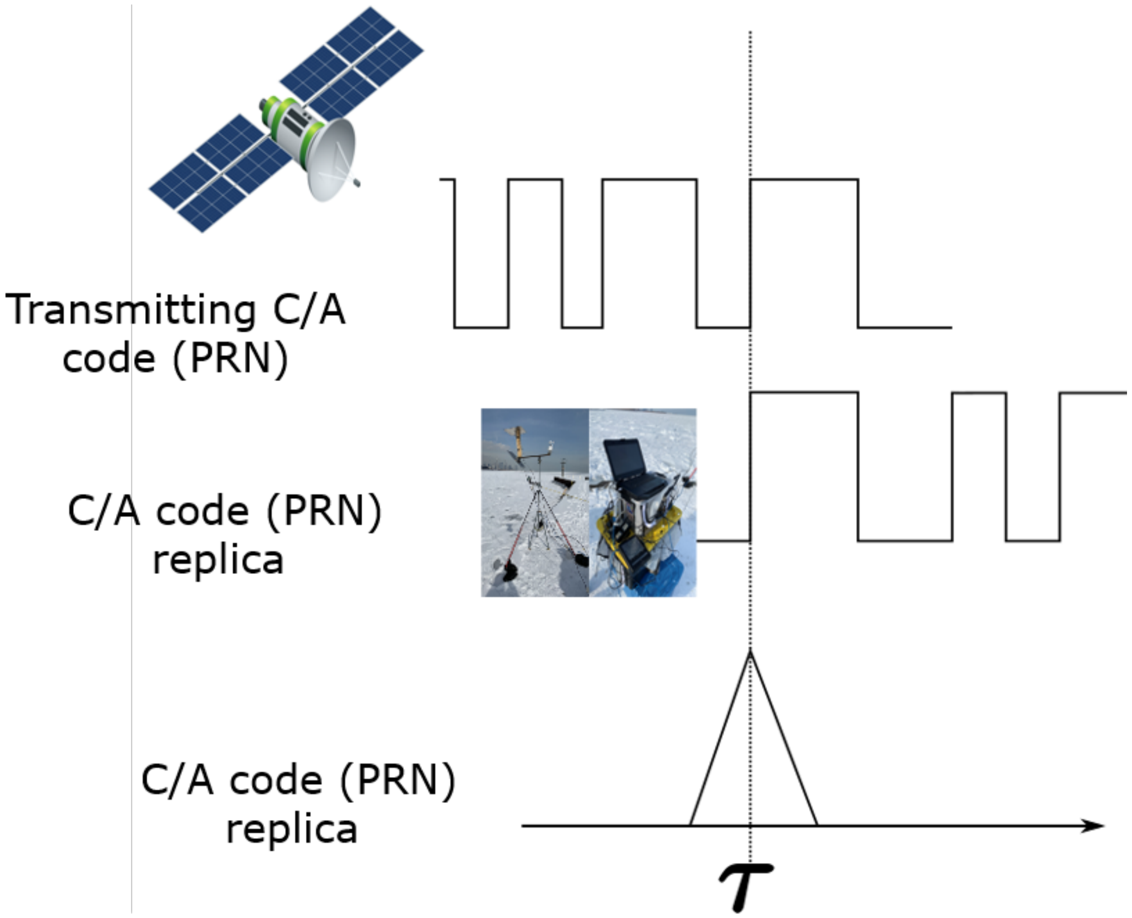

Figure 2.3. GPS signal acquisition process. To detect the GPS signal, the incoming C/A code is correlated with a receiver-generated replica of the C/A code. For a visible satellite the correlation output has a triangle shape.

2.5 GPS signal acquisition

The process by which a receiver determines whether a GPS signal exists in the incoming data from the antenna is called GPS signal acquisition. Figure 2.3 illustrates the GPS signal acquisition process. In short, the incoming signal is correlated with a replica of the known pseudo-random noise (PRN) sequence x. A high correlation peak identifies the satellite to which the transmitted signal belongs. Signal acquisition also yields estimates of the GPS signal delay τ and Doppler shift f_D. The signal search process yields a matrix $\hat{S}(\tau, f_D)$ of correlation power as a function of frequency and

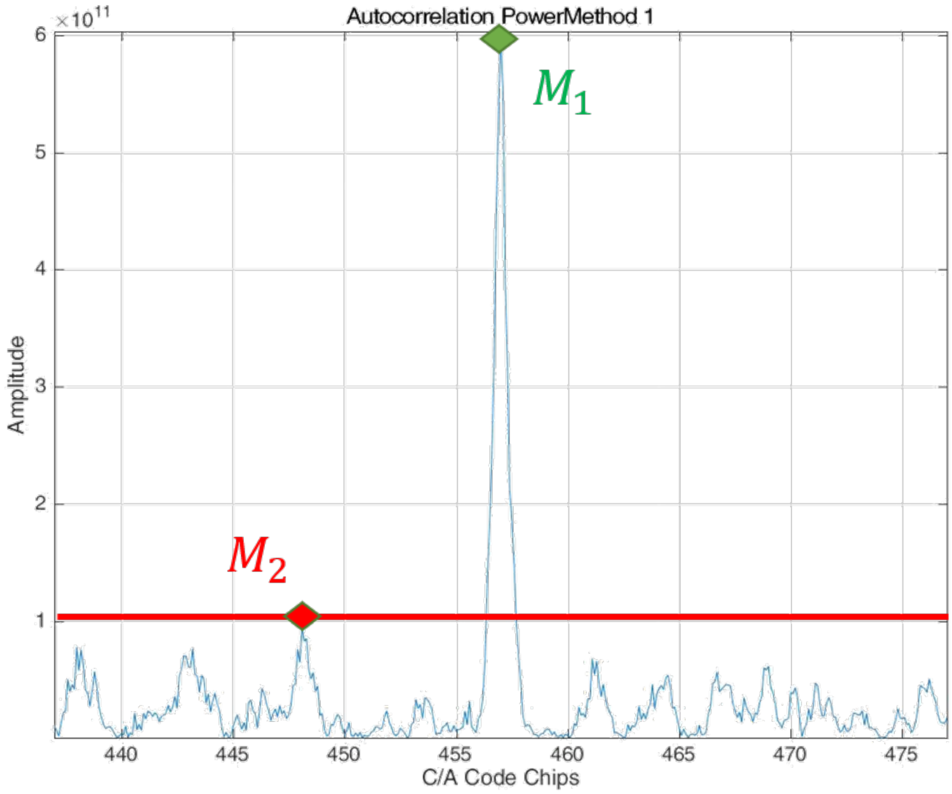

Figure 2.4. Correlation of a real GPS signal, M_1 is the primary peak and M_2 is secondary peak.

code delay space.

An acquisition metric $l^q_{f_D}$ for the qth satellite is defined as the ratio of the primary peak of the correlation power to the secondary peak (excluding points within one chip of the primary peak) at the same frequency [8].

$$l^q_{\hat{f}_D} = \frac{\max\limits_{\tau, f_D}\left(\hat{S}\left(\tau, f_D\right)\right)}{\max\limits_{|\tau-\hat{\tau}|\geq T_c}\left(\hat{S}\left(\tau, \hat{f}_D\right)\right)} \tag{2.3}$$

where $\hat{\tau}$, $\hat{f}_D$ are the delay and Doppler frequency at which the correlation peak occurs. Figure 2.4 is an example of the PRN correlation peak as a function of τ at

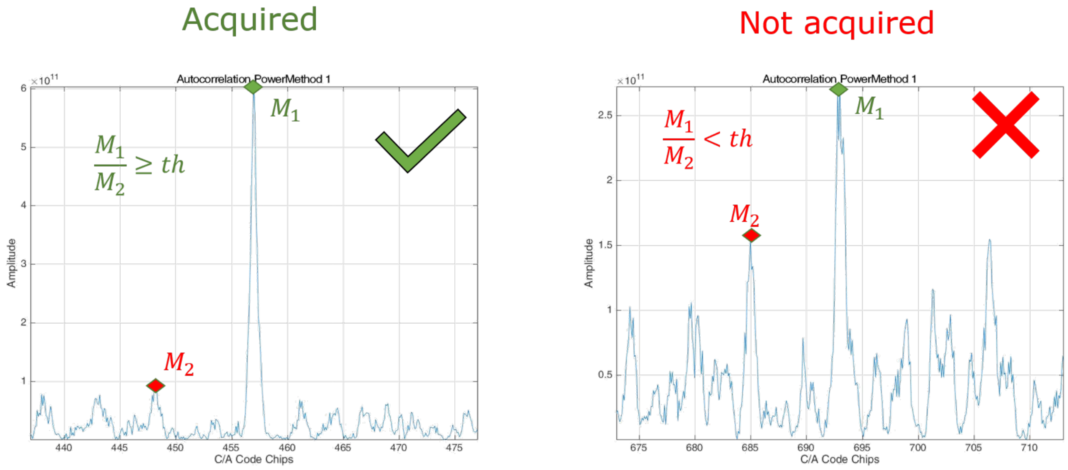

(a) visible satellite (b) invisible satellite

Figure 2.5. Example of the acquired GPS signal (visible satellite) (left) and not acquired (invisible satellite) (right).

Doppler $\hat{f}_D$ that shows the how acquisition metric is computed. In this Figure, M_1 indicates the primary peak, the numerator of Eq. (2.3) and M_2 is the secondary peak, i.e., the denominator of Eq. (2.3). The purpose of the acquisition metric is to determine whether a satellite is visible or not. If the ratio exceeds a given threshold, the satellite (PRN) is indicated as visible. Let H_0 be the null hypothesis that a given satellite is not in the sky, and H_1 be the alternative hypothesis, that the satellite is in the sky. Then the decision for the qth satellite is as follows:

$$\begin{cases} \text{If} \quad l^q_{\hat{f}_D} \geq th \Longrightarrow & H_1 \\ \text{If} \quad l^q_{\hat{f}_D} < th \Longrightarrow & H_0 \end{cases} \tag{2.4}$$

A typical threshold th in off-the-shelf receivers is 2.5. Figure 2.5 is an example of a received GPS signal for which (left) the auto-correlation metric exceeds the threshold and (right) a satellite whose acquisition metric is less than the threshold, so considered not acquired. If acquired, then $\hat{\tau}$, $\hat{f}_D$ are the estimates of the unknown

τ' and f'_D and the receiver proceeds to track the satellite. Different ways to compute the correlation power $\hat{S}$ on which to base the acquisition metric is the subject of Chapter 5.

2.5.1 Coherent integration. The most basic form of signal acquisition is via coherent integration. The phase θ_{L1} is an unknown assumed to be constant over the coherent integration time. The downconverted digitized signal s_{IF} from Eq.(2.2) is multiplied with a locally generated cosine to create in-phase samples s_I, and separately multiplied by a sinusoid for quadrature-phase samples s_Q, at a given Doppler f_D.

$$\begin{aligned} s_{I,n} &= s_{IF}(nT_s)\cos\left(2\pi\left(f_{IF}+f_D\right)nT_s\right) && (2.5)\\ s_{Q,n} &= s_{IF}(nT_s)\sin\left(2\pi\left(f_{IF}+f_D\right)nT_s\right) && (2.6)\end{aligned}$$

or, in complex form,

$$\tilde{s}_n = s_{I,n} + js_{Q,n} \tag{2.7}$$

The tilde represents a complex value throughout this work. Then each $s_{I,n}$ and $s_{Q,n}$ is correlated with a receiver-generated replica PRN code x for time T_{coh}, which is N_{coh} repetitions of the full PRN code.

$$T_{coh} \equiv N_{coh}T_{C/A} \tag{2.8}$$

In this work, correlation over T_{coh} is carried out by first computing the correlation for each segment $T_{C/A}$ consisting of N samples and then summing the correlations over N_{coh} segments. $S_{I,k}$ and $S_{Q,k}$ are correlator outputs for the kth segment of duration

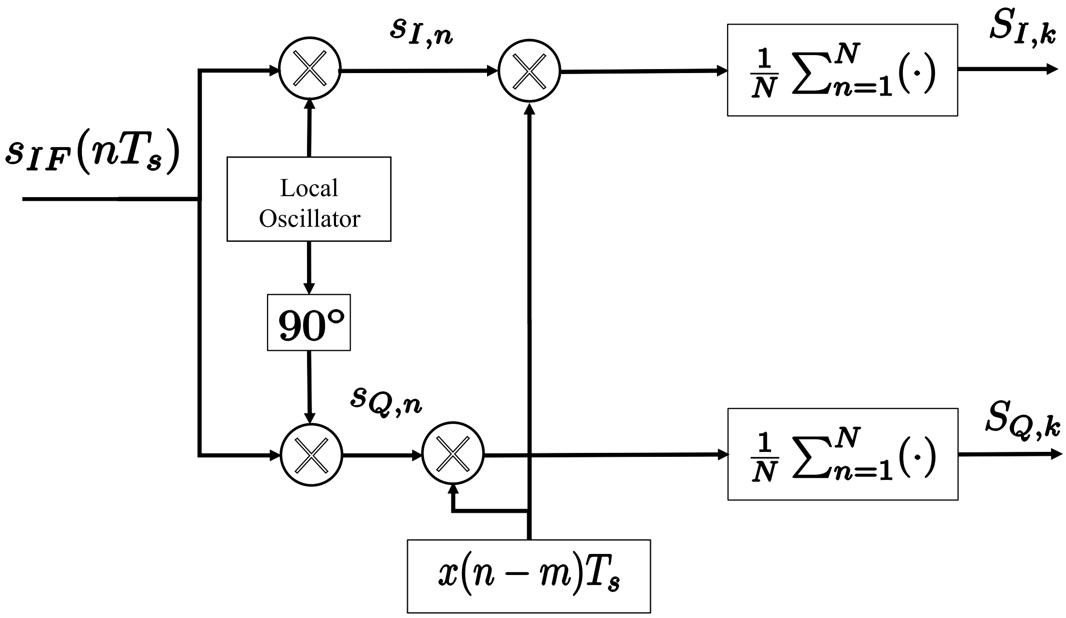

Figure 2.6. Correlation process of the GPS signal.

$T_{C/A}$:

$$\begin{aligned} T_{C/A} &= NT_s & (2.9)\\ S_{I,k}(m,f_D) &= \frac{1}{N}\sum_{n=1}^{N} s_{I,n}x((n-m)T_s) & (2.10)\\ S_{Q,k}(m,f_D) &= \frac{1}{N}\sum_{n=1}^{N} s_{Q,n}x((n-m)T_s) & (2.11)\\ \tilde{S}_k(m,f_D) &= S_{I,k}+jS_{Q,k} & (2.12)\end{aligned}$$

Figure 2.6 shows the basic correlation process. The correlator's outputs $S_{I,k}$, $S_{Q,k}$ are scalar over a two-dimensional space, m corresponding to code delay and f_D Doppler shift. The N_{coh} correlation outputs are then summed to compute power for time T_{coh}:

$$\bar{S}_I = \sum_{k=1}^{N_{coh}} S_{I,k}(m, f_D) \tag{2.13}$$

$$\bar{S}_Q = \sum_{k=1}^{N_{coh}} S_{Q,k}(m, f_D) \tag{2.14}$$

where the overbar indicates summation.

To estimate the Doppler frequency $\hat{f}_D$, the correlation process given by Eqs. (2.10)-(2.11) is iterated for frequencies within a band around the intermediate frequency f_{IF}.

With coherent integration, the correlator output summation $\bar{S}_I$ is used for computing the acquisition metric. There are different algorithms for performing the coherent signal acquisition search, in increasing order of speed and computational complexity: serial search, parallel frequency search, and parallel code phase search, (see [8] for more information). In this work, the parallel code phase search is used as one of our baseline methods. The method will be discussed in more detail in Section 5.3.1. Integration over longer time segments $N_{coh} > 1$ can increase the signal power, enabling acquisition of lower power signals, as long as the unknown data bit D (each of 20 ms duration) in s_{IF} does not change sign within time T_{coh}. However, due to the possibility of a navigation data bit transition (yielding a 180° phase shift), coherent integration is often restricted to a couple of milliseconds [43] [58] . With coherent integration of more than a few ms of data, comparison of the correlation functions of two consecutive data segments helps determine the data segment in which a data bit flip has not occurred. Given a data time series from time $t = [t_0, t_0{+}T_d]$ of duration T_d containing an even integer number of repetitions of the code, the data are divided into two equal duration segments of time $T_1 = [t_0, t_0 + T_d/2]$ and $T_2 = [t_0 + T_d/2, t_0 + T_d]$

with $T_d/2 = T_{coh}$, so that:

$$S_{coh} = \begin{cases} |\bar{S}_{I,T_1}|^2, & \max_m(|\bar{S}_{I,T_1}|^2) > \max_m(|\bar{S}_{I,T_2}|^2) \\ |\bar{S}_{I,T_2}|^2, & \text{otherwise} \end{cases} \tag{2.15}$$

where the maximum is taken over all time shifts m at each Doppler. When only coherent integration is used, $\hat{S} \equiv S_{coh}$.

2.5.2 Incoherent detection. One way to compensate for the unknown phase θ_{L1} is to use the power from the quadrature-phase accumulation $\bar{S}_Q$ as well as the in-phase $\bar{S}_I$. The unknown phase effect on the correlation power can be disregarded by the taking the magnitude of the complex correlation power: .

$$\tilde{\bar{S}}(m, f_D) = \bar{S}_I + j\bar{S}_Q \tag{2.16}$$

In this work, we use both in-phase and quadrature correlation sums $\bar{S}_I, \bar{S}_Q$. However, because those quantities are produced by coherent summation as shown in Eqs. (2.13)-(2.14) in which a data bit flip transition may have inverted one or more of the correlation peaks being summed, two segments for time T_1 and T_2 are again compared to determine which has the greater accumulated power, and therefore, no data bit flip [47]:

$$S_{inc} = \begin{cases} |\tilde{\bar{S}}_{T_1}|^2, & \max_m(|\tilde{\bar{S}}_{T_1}|^2) > \max_m(|\tilde{\bar{S}}_{T_2}|^2) \\ |\tilde{\bar{S}}_{T_2}|^2, & \text{otherwise} \end{cases} \tag{2.17}$$

in which $\tilde{\bar{S}}_{T1}$ is the complex correlation sum for the time segment T_1, and $\tilde{\bar{S}}_{T2}$ is the complex correlation sum for time T_2. Coherent averaging plus incoherent detection increases correlator power, but the sum of the squares of in-phase and quadrature contributions also increases the noise.

2.5.3 Differential integration. To acquire a weak GPS signal in a noisy (e.g., highly scattering) environment, various methods of differential integration have been developed. One post-correlation method is differential coherent (DC) integration. This method was first introduced by [18][65][66] for acquisition of a direct-sequence (DS) binary phase-shift key signal (BPSK), and was extended by [31][53] to GPS signals. The basic concept behind this method is that, when the signal exists in one code repetition k of data, not only will there be a high correlation peak somewhere in the cross-correlation function space (m, f_D), a high correlation peak will also have existed in the previous code repetition $k-1$. Conversely, in the case when the correlator contains noise only (i.e., the null hypothesis H_0), there is low correlation between them [19][20][44]. The complex coherent power $\tilde{S}_k$ from Eq. (2.12) is multiplied by the conjugate of the previous data segment's correlation, $\tilde{S}^*_{k-1}$:

$$\tilde{Y}_p = \tilde{S}_k \tilde{S}^*_{k-1},\ p = 1, 2, ..., N_{coh} - 1 \tag{2.18}$$

$$S_{\tilde{Y}} = \mathrm{Re}\left(\sum_{p=1}^{N_{coh}-1} \tilde{Y}_p \right) \tag{2.19}$$

where the superscript * indicates the complex conjugate, and index p counts sequential segments of duration $T_{C/A}$. As long as the satellite is not immediately rising into or setting from view the correlation functions $\tilde{S}_k, \tilde{S}_{k-1}$ are highly correlated, as captured by the product $\tilde{Y}_p$ of their complex conjugates. The complex-valued products are added and the real part is S_Y. A bit flip may still reduce the product of the correlation peaks, so comparison of the two time segments T_1 and T_2 is again used.

Since differential integration multiplies successive correlation functions, the acquisition metric values will generally be squared compared to the correlation output of coherent or incoherent detection [20][51].

2.6 Reflected GPS signal characteristics

The GNSS signal structure and acquisition procedure were discussed in the previous sections. These are applicable for PNT as well as GNSS-R applications. In this section, important reflected signal quantities for GNSS-R such as the specular point (SP), Delay Doppler Map (DDM), signal-to-noise ratio (SNR) and surface reflectivity (SR) are reviewed.

2.6.1 GNSS reflection. The scattered GNSS reflection signal contains information about the surface characteristics from which it is reflected. For surfaces that are smooth (i.e., the size of surface variations is small compared to the signal wavelength), specular reflection (rather than diffuse reflection) dominates. The specular point (SP) is the reflection point at which the incident and reflection angles are equal. Most energy is typically scattered from the first Fresnel zone surrounding the SP [6]. For high-altitude (low-Earth orbit) GNSS-R, the scattering area is often referred to as the glistening zone (GZ). The size of the glistening zone is a function of the surface roughness and expands as roughness of the surface increases [25] [67].

GPS reflection from water and ice surfaces is well-modeled by specular reflection. Figure 2.7 illustrates the SP and GZ geometry in our test configuration. The final signal received by an antenna is the result of the superposition of scattered GNSS reflections from various points of the GZ. Each of these reflected components travels at a different path toward the downward-facing GPS antenna. Therefore, each reflected ray will have different time delays. In addition, due to the satellite and surface motion, they will have different Doppler frequencies. The locus of points in the GZ with equal time delays has an ellipsoid shape and is called an iso-range (black ellipses in Figure 2.8). Similarly, the locus of points in the GZ with equal Doppler frequency has a hyperbola shape and is an iso-Doppler line (red lines in Figure 2.8) [68]. Appendix A describes the estimation of the specular point position as used in

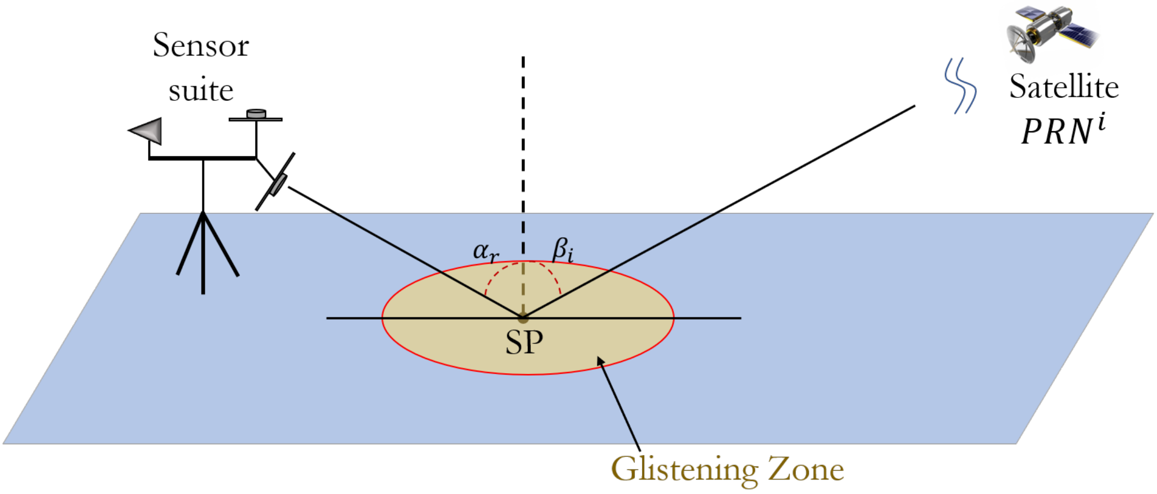

Figure 2.7. illustration defining the specular point at which α_r quals β_i and the glistening zone.

this work.

2.6.2 Delay Doppler Map (DDM). The signal received after reflection is a superposition of the signals that reflected from different points on the surface. Each will have a slightly different delay (τ) due to different path lengths. Each may also have different Doppler frequency due to the surface motion (f_D). As a result each of the points on the surface may be distinguished with its own delay and Doppler frequency. Figure 2.9 illustrates the relationship between the two-dimensional spatial domain and Delay Doppler domain. The locus of all points whose signal travels the same distance is an iso-range ellipse. The locus of points with equal Doppler frequency lie on an iso-Doppler hyperbola. Then, power scattered form these points can mapped to the Delay Doppler domain (2.9 right). Points in the spatial domain with a single delay and Doppler pair (red in Figure 2.9 left) map to a point in the Delay Doppler domain (red in Figure 2.9 right). A reflected signal with a specific time delay and Doppler frequency pair corresponds to a region on the surface.

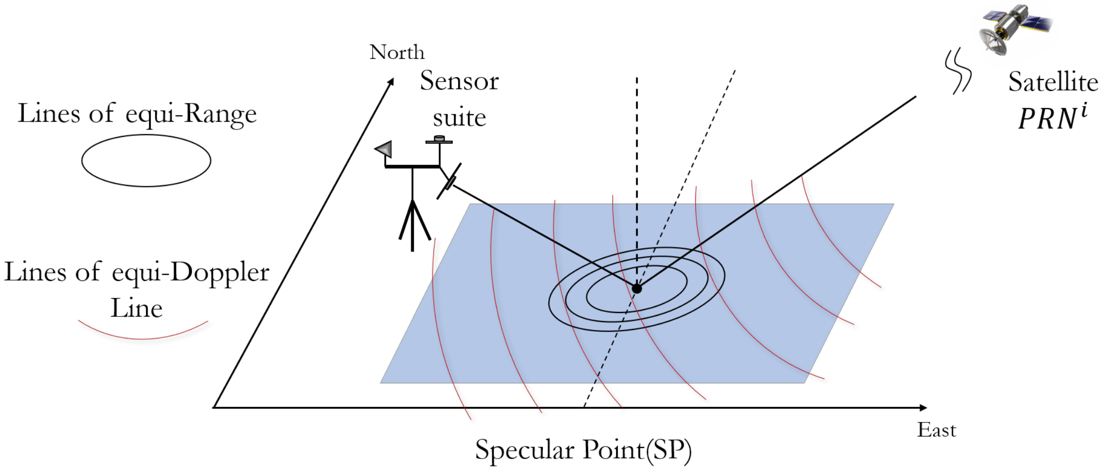

Figure 2.8. Iso-range ellipsoids (black) and iso-Doppler hyperbolas (red).

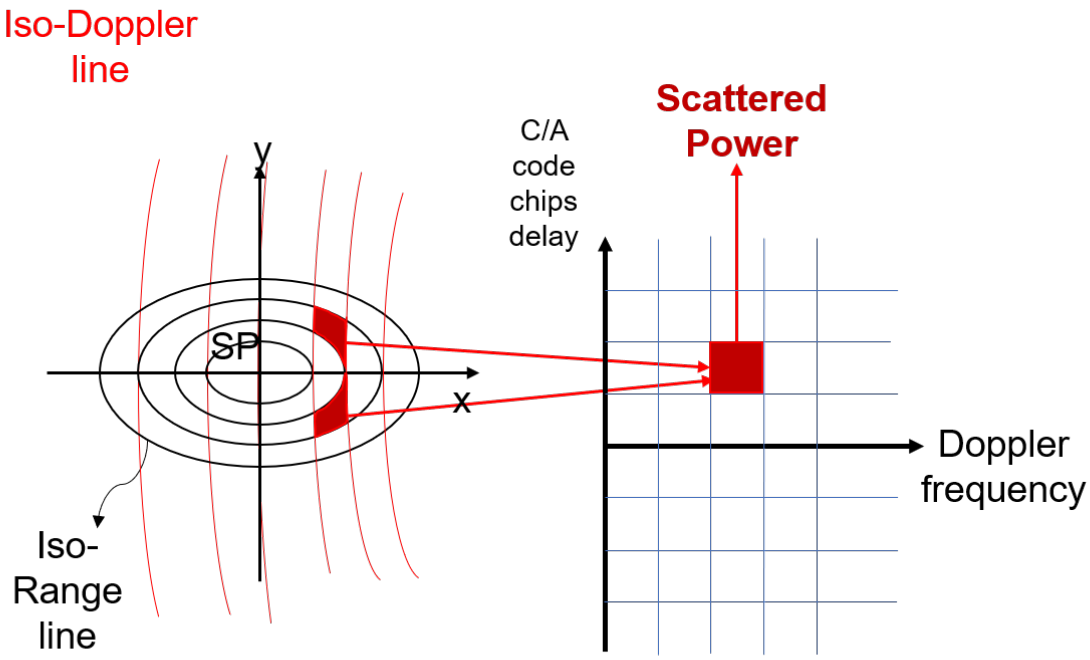

Figure 2.9. Relation between the spatial and Delay Doppler domain.

Scattered power can be computed for all pairs of time delay $\hat{\tau}$ and Doppler frequency $\hat{f}_D$ and is represented as a function of two variables. The correlation power is given by Gleason [26]:

$$Y_s(\tau, f) = P_s T_{C/A}^2 \wedge^2 (\tau - \tau') S^2(f - f') \tag{2.20}$$

where $P_s = A_s^2$, with A_s the signal amplitude at the receiver, and $T_{C/A}$ is the coherent correlation interval of 1 ms. The correlation triangle function $\wedge$ for the GPS code is given by:

$$\wedge\left((\tau - \tau'\right) \approx \frac{1}{T_{C/A}} \int_0^{T_{C/A}} < x(t - \tau')\hat{x}(t - \tau) > dt \tag{2.21}$$

$$\wedge\left((\tau - \tau'\right) = 1 - \frac{|\tau - \tau'|}{T_c} \tag{2.22}$$

where T_c is the pulse duration of the C/A code chip. In Eq.(2.20) S is the sinc function:

$$S(\hat{f} - f) = \frac{\sin(\pi(\hat{f} - f)T_I)}{\pi(\hat{f} - f)T_I} \tag{2.23}$$

In our work, we use the fast Fourier transform and cross correlation to obtain the DDM. The calculated scattered power is referred to as the Delay Doppler Map (DDM).

2.6.3 Signal-to-noise ratio. Another characteristic to study the reflected GNSS signals is the signal-to-noise ratio (SNR). SNR is the ratio of the signal to the floor noise level. To compute the SNR, the Eq.(2.24) is used from [42].

$$SNR = \frac{P_{max} - P_{noise}}{P_{noise}} \tag{2.24}$$

In this equation, P_{max} is the maximum of the correlation function, for example the value M_1 in Figure 2.4, and P_{noise} is the mean value of the noise, i.e., the mean value of correlation function excluding the values within $\pm T_{C/A}$ of the correlation peak.

2.6.4 Surface reflectivity.

Surface reflectivity of a scatterer is the fraction incident signal power that is reflected. Beginning from the radar equation for power arriving at a receiver,

$$P_{rl}^{r} = \frac{P_r^t G^t}{4\pi(R_{ts}+R_{sr})^2}\frac{G^r\lambda^2}{4\pi}\Gamma \tag{2.25}$$

where P_{rl}^{r} is the coherent component of scattered power, P_r^t is the transmitted RHCP power, G^t is the gain of the transmitting antenna, G^r is the receiving antenna gain, λ is the carrier wavelength, Γ is the surface reflectivity, and finally R_{ts} and R_{sr} are the distance from the transmitter (satellite) to the specular point and from the specular point to receiving antenna, respectively. Using the SNR as P_{rl}^{r} to which it is proportional, the surface reflectivity SR in dB may be computed by Eq. 2.26, taken from [12]:

$$\begin{aligned} SR \;&\propto\; SNR - 10\log(P_r^t) - 10\log(G_r^t) - 10\log(G^r) - 20\log(\lambda) \\ &\quad +20\log(R_{ts}+R_{sr}) + 20\log(4\pi) \end{aligned} \tag{2.26}$$

Once the SNR is computed, all quantities are known on the righthand side except the receiving antenna gain G^r. In general this will be a function of the direction of an incoming signal to the receiving antenna.

For the hemispheric antennas used in this work, gain patterns are provided by the manufacturer [15]. To calculate the antenna gain, the antenna zenith angle ϕ between the position vector $\vec{r}^{sp/R}$ of the specular point relative to the reflected antenna and the zenith direction $\hat{s}$ of the antenna is computed. When $\phi = 0$ the antenna has maximum gain. As ϕ increases the antenna gain decreases. Appendix B describes the calculation of ϕ and the antenna gain table based on the manufacturer's specifications.

CHAPTER 3

SENSOR SYSTEM DESIGN AND FABRICATION

3.1 Overview

To collect reflection data for ice and water conditions, and to compute reflected signal properties for ice and for water, a sensor suite is designed that includes a dedicated GNSS-R antenna pointing toward the surface being sensed. Also, to evaluate and correlate the results from the GNSS-R signals with physical surface conditions a lidar, camera, and weather station are collocated with the GNSS-R. Finally, a direct GNSS antenna is included in the system for PNT.

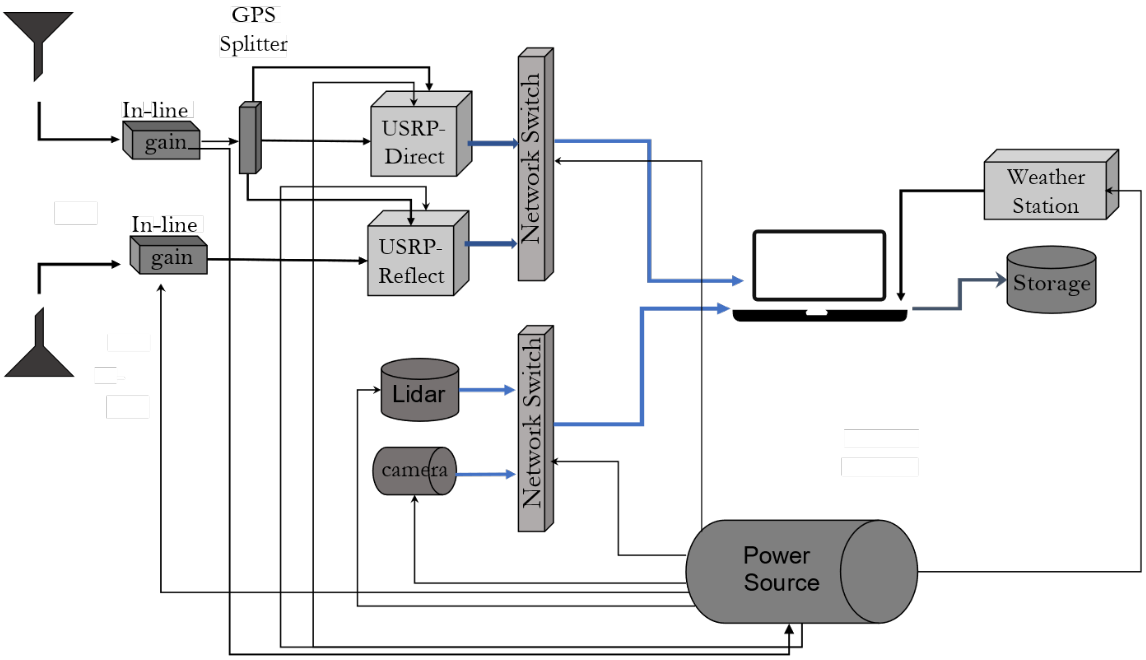

Figure 3.1. Schematic of the GNSS-R sensor system.

Figure 3.1 illustrates the sensor suite hardware, which includes: two antennas, two universal software radio peripherals (USRPs), a lidar, camera, weather station, and supporting electronics. GNSS antennas (Antcom models G8Ant-3A4TB1 and G8Ant-3A4TB1-LH) with right hand circular polarization (RHCP) for the direct signal and left hand circular polarization (LHCP) for the reflected signal are used, respectively. Since the transmitted GPS signal is RHCP and polarization changes upon reflection, the intent of using opposite polarization antennas is to suppress reflected signals in the RHCP direct antenna and direct signals in the LHCP reflected antenna. Meanwhile, USRPs (National Instruments Ettus N210) play the role of the traditional receiver front-end for GNSS signals. One USRP is used for direct signals and the other one for reflected GNSS signals. A Velodyne VLP-16 “puck” lidar, AcuRite 01528 weather station, and GW2237 IP camera are collocated to within a meter with the GNSS antennas as auxiliary instruments of the sensor suite. Supporting electronics include a rechargeable battery power source for the antennas, USRPs, lidar, and ethernet switches. The switches connect to a laptop for communicating with the sensors. GNSS, lidar, and camera data are collected via the laptop and stored on external storage devices. The weather station connects directly to the laptop via a USB port.

The chapter is organized as follows: Section 3.2 discusses a single USRP N210 initial setup, operation and signal preconditioning. A USRP N210 is designed for variety of applications. In the signal preconditioning section it is tuned for GNSS/GPS implementation, namely, to provide inputs to the software-defined receiver (SDR) and test GNSS-R calculations. In Section 3.3, two USRPs are set up to work simultaneously, one for the GNSS direct signal used for PNT, and the other one for reflected GNSS signals. Therefore, a dual-USRP system is designed and evaluated in this Section. In Section 3.4 two GPS-disciplined oscillators (GPSDOs) are installed into both USRPs, to improve internal USRP clock accuracy, and are tested in the lab.

The lidar is described in Section 3.5.1, and its integration for simultaneous data collection with the USRPs in Section 3.5.1. Finally, operation of the full USRPs, lidar, and camera system is described in Section 3.5.2.

3.2 Single USRP

In this section a USRP is initialized and tuned to serve as a GPS front-end. The USRP is tested with a GPS signal simulator, by checking whether a software-defined GPS receiver (SDR) can acquire simulated GPS satellites from the USRP data stream.

3.2.1 Initial setup. The universal software radio peripheral (USRP) is an instrument used for receiving and transmitting a radio signal, and has a wide variety of possible applications. In the GNSS-R project, two USRPs serve as GNSS receiver front-ends, providing signal pre-amplification, down-conversion, and digitization. The USRPs for this project are the Ettus N210 model, which produce high bandwidth, high-dynamic range processing capability. The N210 consists of a motherboard with a Xilinx Spartan field-programmable gate array (FPGA), and a choice of daughterboard [21] [17] [52]. The SBX-40 daughterboard is used for front-end processing (pre-amplification and bandpass filtering). The SBX daughterboard gain range is 0-31.1 dB. It provides up to 40 MHz bandwidth in the 400 MHz-4400 MHz range, which encompasses the GNSS bands. The USRP comes with a 2.5 ppm TCXO frequency reference. As an additional timing accuracy option, we have selected the GPS-disciplined oscillator (GPSDO) unit, which provides 0.01 ppm when connected to a GPS antenna, using GPS for timing.

After installing the GPSDO and SBX in each USRP (see Figure 3.2), the latest version of the USRP hardware driver (UHD) is downloaded and installed on a client computer and added to the system path. Both C/C++ compilers and python are required on this machine and added to the system path. The USRP is connected via crossover ethernet cable to the workstation, and LAN IP static addresses are assigned to the USRP and to the computer. After the device (i.e., USRP) is found, the FPGA image is loaded into the USRP and updated. The USRP configuration can be listed and verified with the appropriate UHD command. This process is repeated for each USRP.

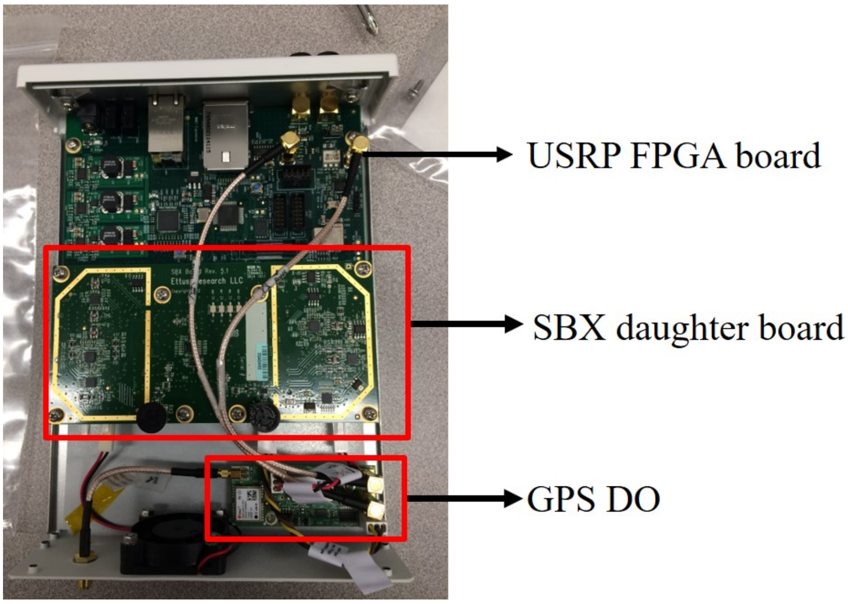

Figure 3.2. USRP N210 Hardware.

3.2.2 Single USRP operation and lab test. Initial testing of USRP operation is conducted in the lab. The purpose of this test is to check that a GPS data stream can be obtained from the USRP, and that it has the expected GPS signal properties. Figure 3.3 shows the testing configuration. We connect a Spectracom GSG-62L5 GNSS simulator, which generates a low noise GPS L1 signal with output signal power set to -95 dBm, to the daughterboard antenna port on the USRP (labeled TX/RX). We connect the GPSDO antenna port on the back of the USRP enclosure to a stationary GPS antenna mounted on the roof of the lab. Tests were also conducted without the timing reference antenna, and the results (not shown) were found to be essentially

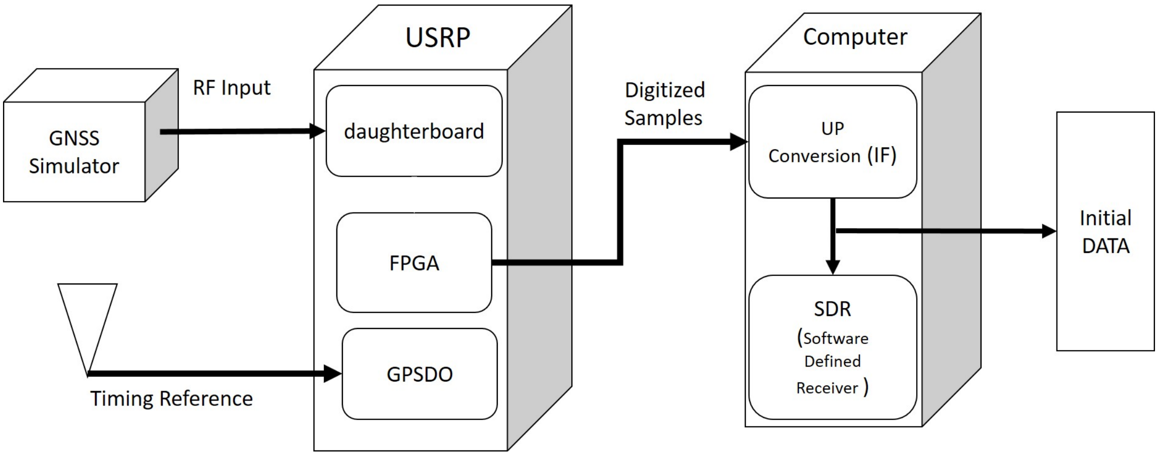

Figure 3.3. USRP in-lab testing configuration. A simulated noise-free GPS L1 signal is input as sample data. A static roof-mounted GPS antenna is used for the GPSDO timing reference.

identical to those with the reference.

A command line executable records sample data to a file, with options such as total number of samples to receive that can be specified. We collect samples with these specifications:

- Bandwidth = 40 MHz
- sample rate = 10 Msps
- gain = 30 dB
- collection duration = 15 s

The default setting for the USRP is to convert to baseband. However, our software defined receiver (SDR) is based on a Matlab software receiver prototype from [8], which takes intermediate frequency (IF) samples as input. For this reason, we convert the USRP sample data from complex in-phase and quadrature-phase (IQ) samples at baseband to IF data samples (described in further detail in Section 3.2.3) [58].

The IF samples are post-processed in the SDR to demonstrate that they are in fact those of a GPS L1 signal. For this aim the SDR "probeData" function [8] is used to plot a segment of the sample data in the time domain, the frequency domain, and as a histogram of the binary samples. The results of this test will be shown in Section 3.2.3.

3.2.3 Signal Preconditioning.

To tune a USRP for GPS applications, the USRP's output format and sampling parameters and effects of the automatic USRP automatic gain controller, are studied. To examine the effects of each parameter, the USRP is examined in the lab using a GNSS simulator. After lab testing, USRPs are evaluated outdoors with the GPS constellation. Also, the USRP is investigated with variety of external in-line- gains. All of these steps are described in detail in this section.

3.2.3.1 USRP N210 output data format and sampling parameters.

The USRP Ettus N210 output data format is 16-bit for in-phase and 16-bit for quadrature-phase of the complex signal. Since the SDR works with real values, URSP output data are converted from complex to real data (up-conversion) [58]. Figure 3.4 describes initial the data process from the USRP output to the SDR.

The USRP starts to collect sample data when the rx_to_samples_to_file function is executed. The output data format can be changed by modifying function arguments such as:

- –type arg
    - Sample type: double, float, or short (default =short)

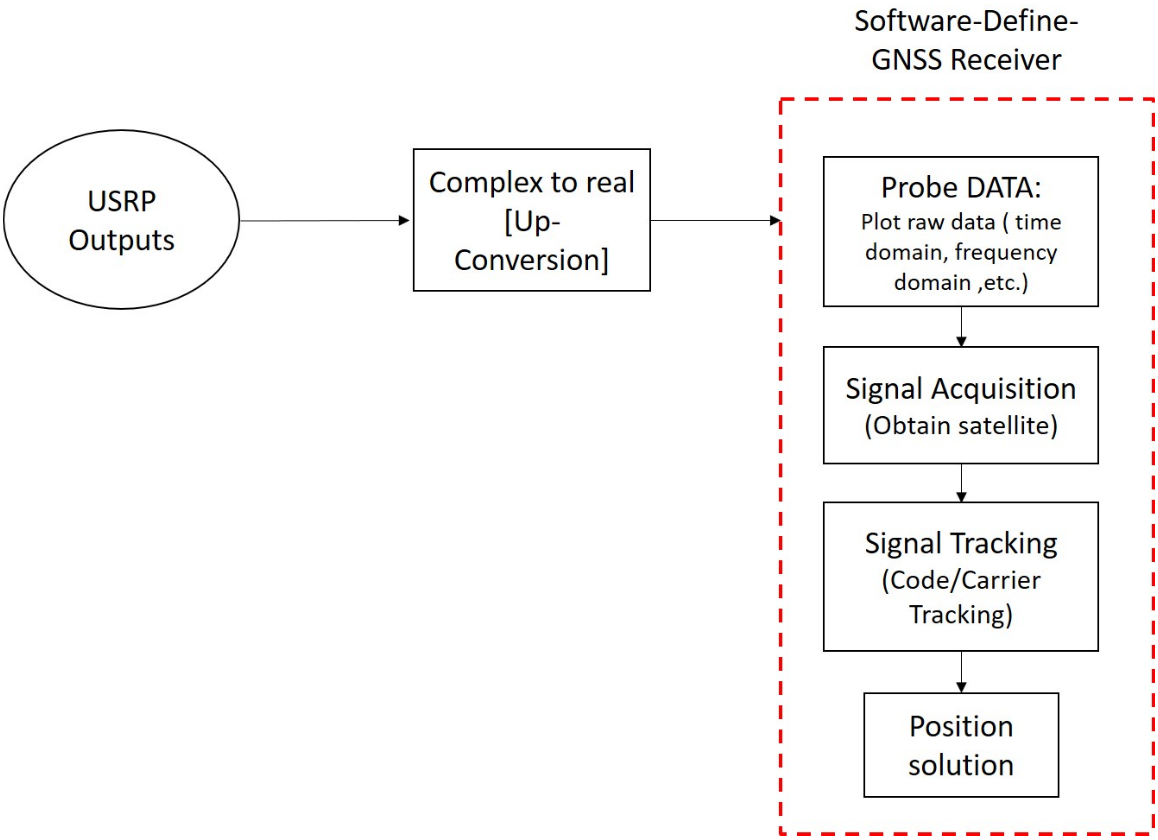

Figure 3.4. Initial data processing flow from the USRP output to the SDR. The SDR flowchart is inside the red box.

- –rate arg
  - Rate of incoming samples (Msps)
- –gain arg
  - Gain for RF chain (USRP internal Gain)
- – ref arg
  - Timing Reference source (internal, external, MIMO) default= internal
- –wire-format arg
  - Sc8bit or sc16 (default= sc16bit)

To examine each parameter, the USRP was connected to a GNSS simulator, then output data were converted from complex to real and evaluated using the SDR (Figure 3.4). For complete testing, each of the arguments was studied and adjusted holding all other arguments fixed. For instance, when the internal clock was chosen as reference, the sample data type was fixed to be short and sample data format was set to 16 bit. This process was applied for all combinations of parameters ([8]). The SDR was not able to acquire any GPS satellites. Changing the parameters did not significantly change the SDR results, so the default format of -SC16-short was selected.

3.2.3.2 Truncating the initial USRP output data. After the USRPs were examined with various argument settings for data type and wire-format, each configuration was evaluated in the lab with different USRP RF gains. Figure 3.5 represents the gain configurations tested.

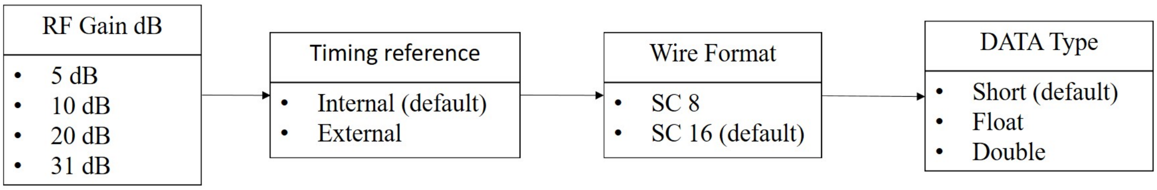

Figure 3.5. USRP test configuration with a simulator for various RF gains.

Identical processing was used as for the prior section tests (Figure 3.4), i.e., the SDR time series were used. Figure 3.6 exhibits an example of USRP output samples in the time domain for the first 0.02 ms, frequency domain and histogram of sample data as plotted using the SDR. The frequency domain plot shows a narrow peak at the intermediate frequency of 5 MHz, but not the GPS spread-spectrum power spectral density. The histogram is not a Gaussian, which pseudo-random noise is expected to be.

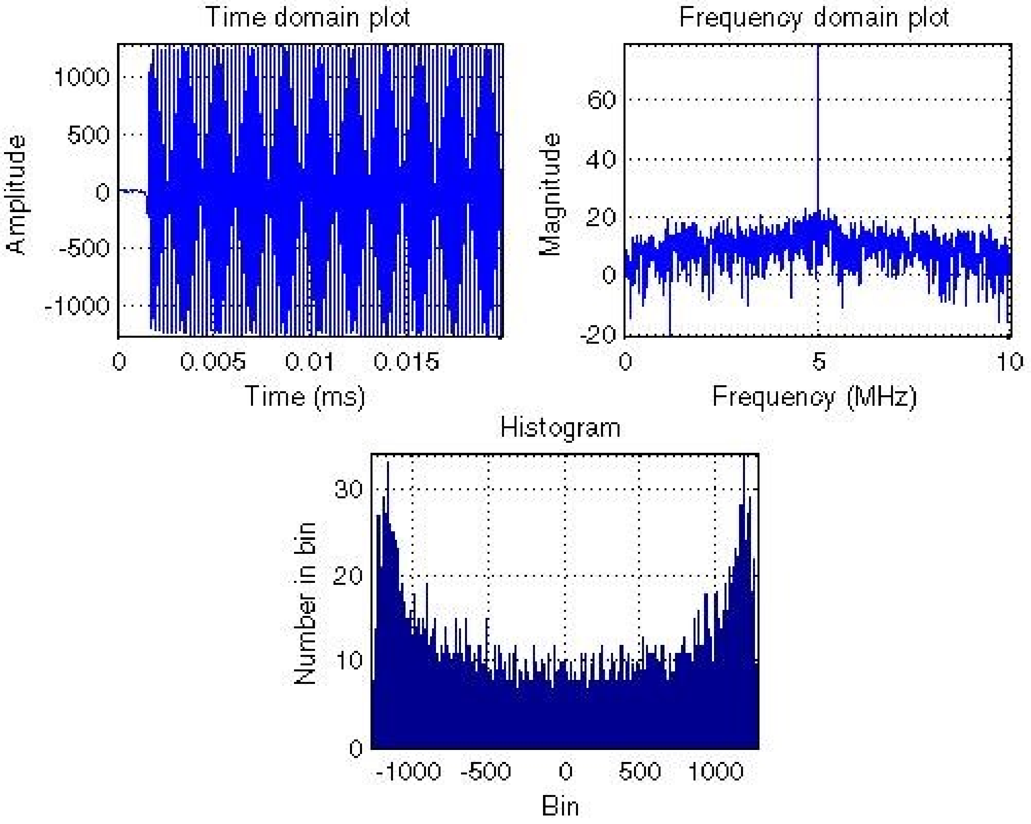

Figure 3.6. Sample data in time domain (top left); frequency domain (top right); histogram of the digitized samples (bottom). Parameters are: sample rate=10 MHz and gain=5 dB.

Modifying the USRP RF gain in the various combinations shown in Figure 3.5 did not improve the SDR results from those shown in Figure 3.6. To diagnose the problem, a longer time series of 0.06 s of USRP output samples from GNSS simulator signals is shown in Figure 3.7. This data was collected using a GNSS simulator with sampling rate = 10 MHz and gain = 5 dB, and shows the in-phase data prior to complex-to-real conversion. As shown in Figure 3.7, the amplitude of the raw data sharply rises to 1000 units oscillating with a gradually decreasing envelope until it falls to ±50. This may be an effect of the automatic gain control settling time in the USRP. Figure 3.8 illustrates 2 s of raw data, after the first 0.06 second truncated.

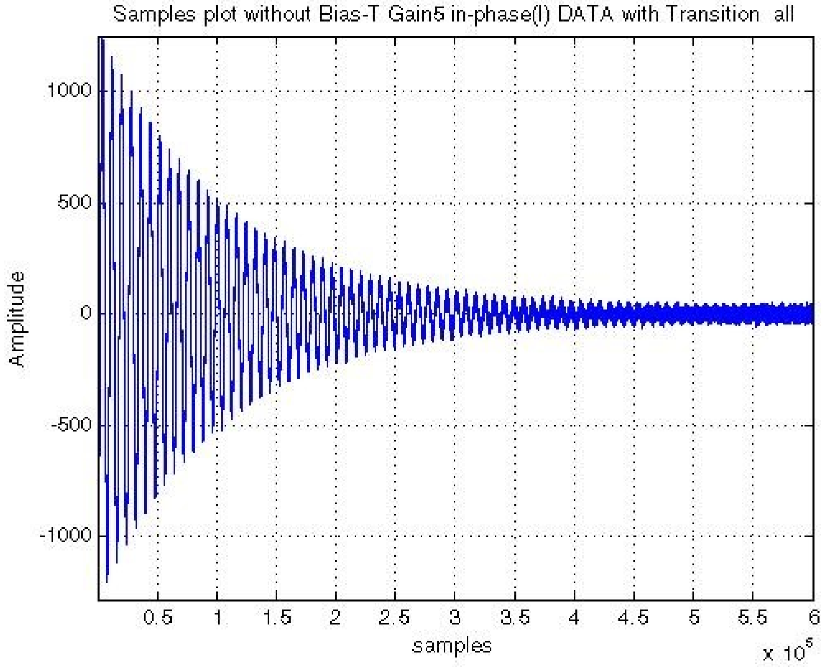

Figure 3.7. Time series of USRP sample data over the initial 0.06 seconds of the data-set.

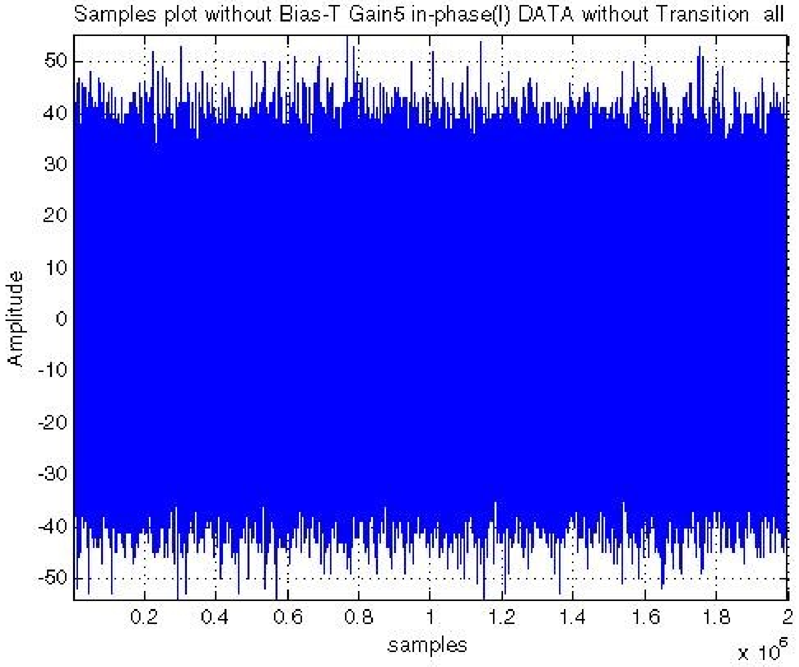

Figure 3.8. USRP data after truncating the first 0.06 seconds.

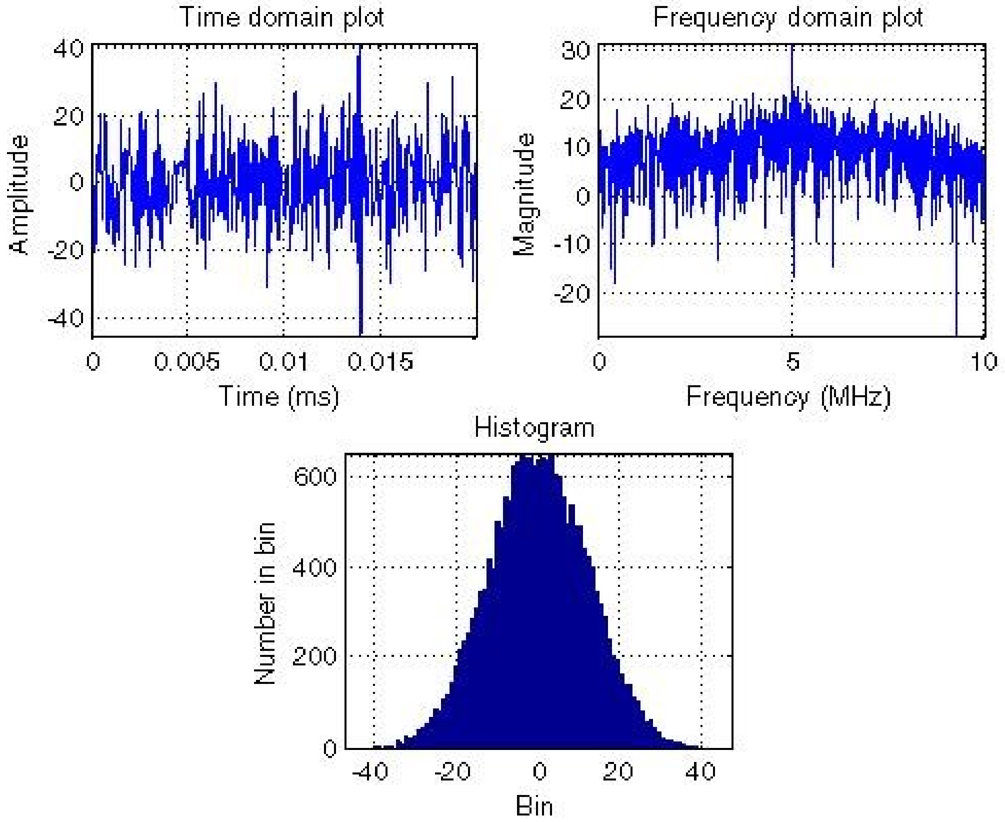

Figure 3.9. Data input to the SDR after truncating the first two seconds, in the time domain (top left); frequency domain (top right); histogram of the digitized samples (bottom). Parameters are: sample rate=10 MHz, gain=5 dB.

After the first 0.06 s, the rest of the time signal appears to be noise which is what we would expect prior to any GPS signal processing for de-spreading and acquisition (Figure 3.8). Therefore, 2 seconds at the beginning of any dataset from the USRPs is truncated. After truncating the initial 2 seconds, the USRP raw data output results are similar to reference results given in [17]. Figure 3.9 is the result of the same data after truncating 2 seconds. The time series is pseudo-random, the frequency peak at the intermediate frequency, and the histogram of samples is Gaussian, all as expected. As a result of these lab simulator tests, the process of preparing the USRP's output data for input to the SDR, which is termed here "signal preconditioning," includes truncating about the first 2 seconds and converting the data from complex to real, as illustrated in Figure 3.10.

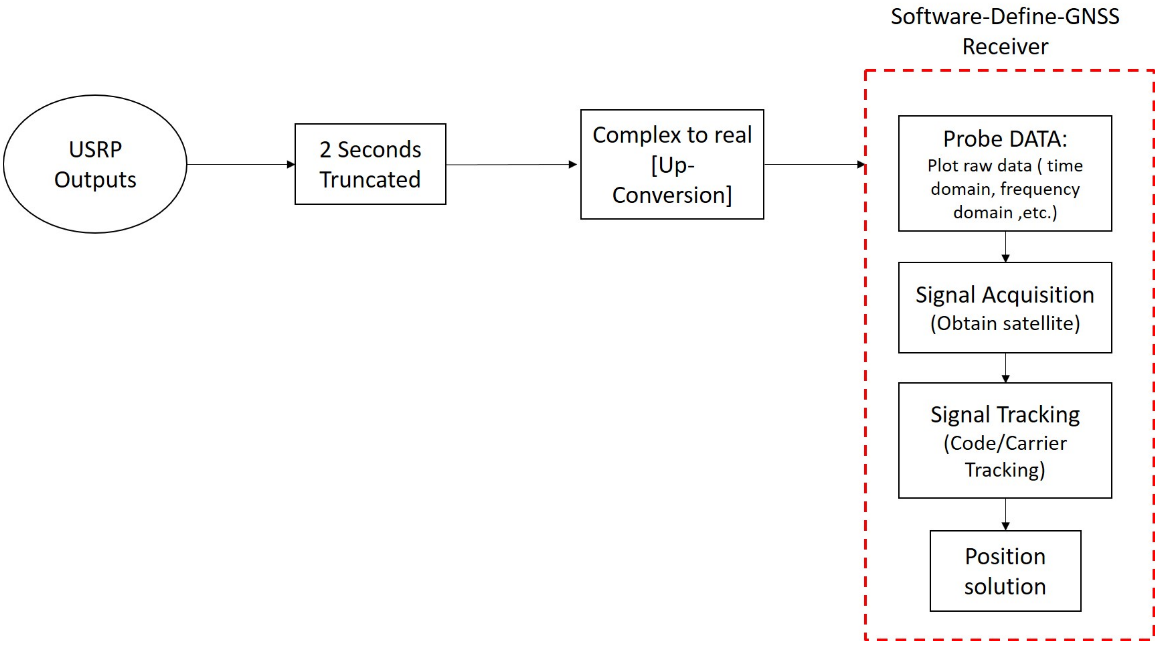

Figure 3.10. Updated data process before input to the SDR.

3.2.3.3 GPS signal power. GNSS signals have comparatively low power when received on the Earth ranging from -162.5 dBW to -154.5 dBW for a typical antenna depending on elevation [43]. For this reason, the USRPs were examined with various simulated GPS signal power levels using the GNSS simulator. For each input GNSS signal power from the simulator, the signal is split to each USRP, one using the minimum internal RF gain of 0 dB and the other using the maximum internal RF gain of 31 dB. Input signals were generated with a low noise-GNSS simulated signal. The purpose of this test was to determine whether and how much additional in-line gain may be required beyond those of the antenna and USRPs themselves. Figure

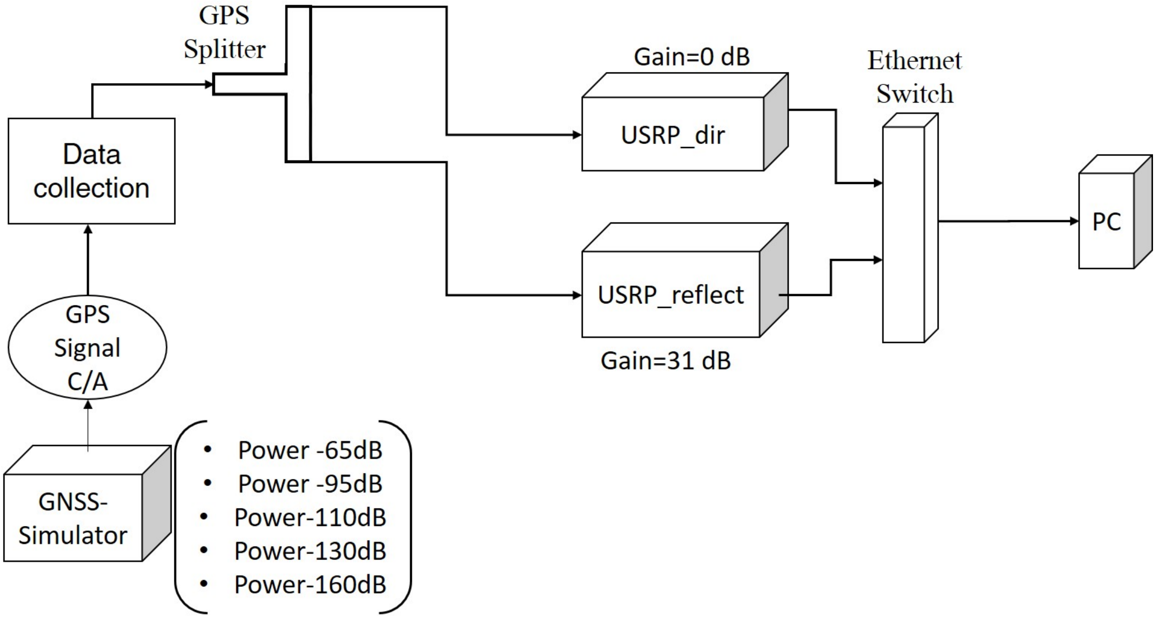

Figure 3.11. Test configuration to study USRPs with various GPS signal power to determine in-line gain requirements.

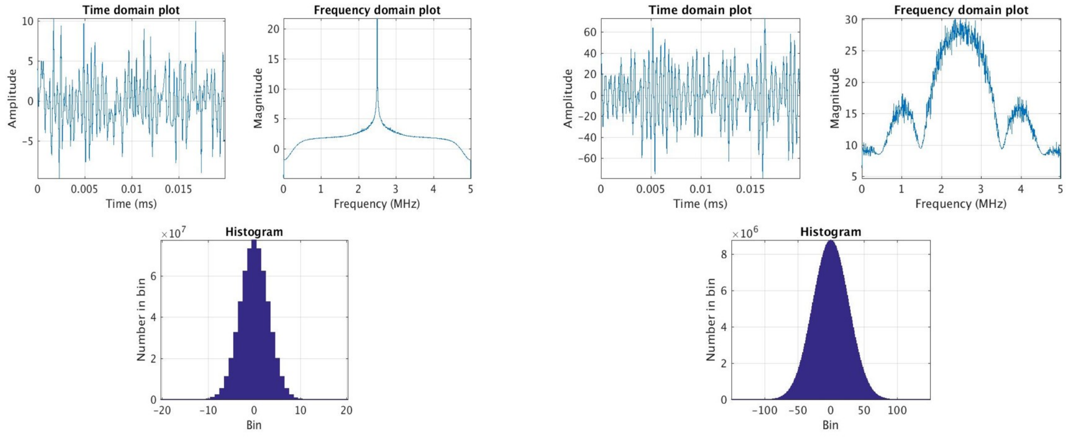

USRP-dir With 0 dB Gain

USRP-ref With 31dB Gain

Figure 3.12. Time domain, frequency domain, and histogram of the samples for RF gain test 4: (left subplots) USRP with 0 dB RF gain. (right subplots) USRP with 31 dB RF gain. The test is conducted with a simulated GPS noise-free signal with -95 dBW input power.

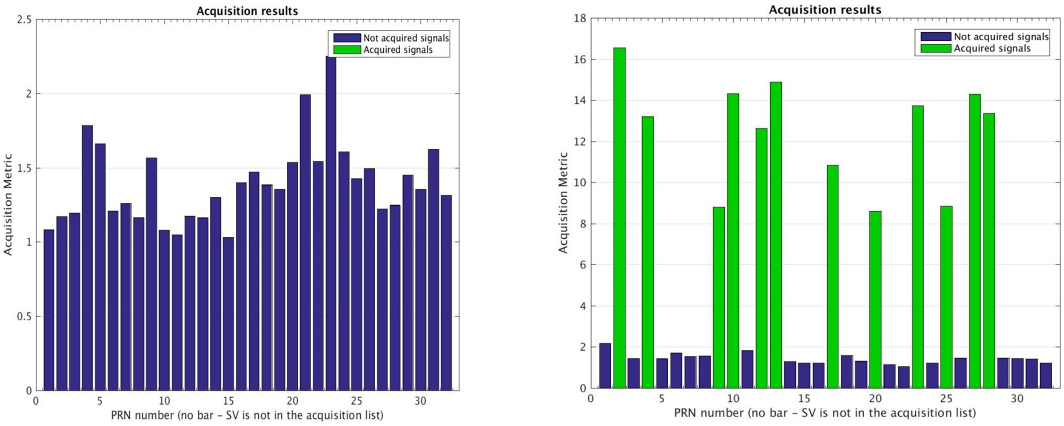

USRP-dir With 0 dB Gain

USRP-ref With 31dB Gain

Figure 3.13. Signal acquisition results for RF gain test 4: (left) USRP with 0 dB RF gain. (right) USRP with 31 dB RF gain ([52]).

3.11 describes the test configuration.

To perform this test, one of the USRPs is set to have a 0 dB RF gain and the other one to have 31 dB. Table 3.1 lists the USRP gain case studies tested with various input GNSS powers. USRP 2 with 31 dB RF gain is able to acquire GPS satellites with −110 dBW power. This is the minimum plausible input signal power for USRP with maximum RF gain. The time domain, frequency domain, and histogram of the samples input to the SDR with -95 dBW input power for USRPs with 0 dB and 31 dB RF gains (Test 4 in Table 3.1) are presented in Figure 3.12. Both USRPs' samples have a normal distribution (see Figure 3.12 bottom plots). However, only the USRP with 31 dB RF gain shows the spread-spectrum GPS signal in the frequency domain (Figure 3.12 right uppermost plot). The signal acquisition results from the SDR for these two configurations is shown separately in Figure 3.13. Each bar represents the acquisition metric for a single PRN [8]. Only the USRP with 31 dB RF gain for an incoming noise-free signal of -95 dBW has enough power that the GPS satellites can be acquired (Figure 3.13 right).

Table 3.1. RF gain requirement experimental tests of USRPs in the lab.

Test #	USRP N210	Power dBW	RF Gain dB	sample rate (MHz)	Duration	Signal Acquisition
1	USRP1	-160	0	5	60	NO
	USRP 2	-160	31	5	60	NO
2	USRP1	-130	0	5	60	NO
	USRP2	-130	31	5	60	NO
3	USRP1	-110	0	5	60	NO
	USRP2	-110	31	5	60	YES
4	USRP1	-95	0	5	60	NO
	USRP2	-95	31	5	60	YES
5	USRP1	-65	0	5	60	YES
	USRP2	-65	31	5	60	YES

3.2.4 Filter design. All previous USRP studies were conducted in the lab with a GNSS simulator. In reality GPS signals arrive at the antenna with noise, e.g., from thermal sources and multipath interference. To reduce noise from USRP output data, a low-pass filter was designed. Two low-pass filters with different stop-band and passband frequencies were adapted from the literature and applied to the USRP-SDR system [10] [57]. In addition, three other low pass filters with different pass band, stop band frequencies were compared (see Table 3.2).

For each filter, six different configurations A through F (Table 3.3) were tested to analyze MATLAB filter functions and notch filter effects on the signal. Outdoor GPS data (directed GPS signals) were collected in three experiments I, II, and III, for different GPS in-line and USRP RF gains, as shown in Table 3.4. Figure 3.14

Table 3.2. Low pass filters tested.

Filter number	1	2	3	4	5
Filter name	Chebyshev Type II	Butterworth	Equiripple FIR	Equiripple FIR	Kaiser window
Filter method	Cheby2	Butter	Equiripple	Equiripple	Kaiserwin
Pass band frequency	-	$0.45\times f_s/2$	$0.2\times f_s/2$	$0.2\times f_s/2$	0.2
Stop band frequecny	$0.45\times f_s/2$	$0.55\times f_s/2$	$0.25\times f_s/2$	$0.25\times f_s/2$	0.25
Passband ripple	-	-	-	-	0.5
Passband Weight	-	-	1	1	-
Stopband Weight	-	-	2	1	-

Table 3.3. Configurations in which low pass filters are studied. All filters are implemented with MATLAB built-in functions.

Configuration	Letter
MATLAB filter function	A
filter function + notch filter	B
notch filter + filter function	C
MATLAB filtfilt function	D
filtfilt function + notch filter	E
notch filter + filtfilt function	F

shows the test environment on the IIT baseball field (See [52] for more details).

For experiment II (defined in Table 3.4), we present results comparing the different filters in Table 3.5. In Table 3.5 it can be seen that the maximum number of satellites N and higher acquisition metric R are obtained by applying Filter 1, the Chebyshev Type II function (see Table 3.2) in Configuration D-F. The results in Table

Table 3.4. USRP gain configurations for each IIT baseball field experiment.

Experiment	I	II	III
GPS in-line gain	0 dB	0 dB	30 dB
USRP RF gain	0 dB	31 dB	31 dB

Figure 3.14. Left: Google Map satellite image of sensor location for the field test. The white cross indicates sensor location. Right: Photo of the experiment hardware setup, with distances notated.

3.5 also hold for experiment III for Configurations D-F (not shown). However, for experiment I, in which both USRP RF and GPS in-line gain were 0 dB, the USRP was not able to acquire any GPS signals with any filtering method in any configuration. Figure 3.15 illustrates the SDR input data in the time domain, frequency domain, and as a histogram for experiment II before and after filtering. Figure 3.16 shows PRNs acquired by the SDR before and after filtering.

Table 3.5. Signal acquisition results for five low-pass filters, with 6 different configurations each, that are applied to the experiment II data. N and $R = l^{q}_{\hat{f}_D}$ stand for number of acquired satellites and the acquisition meteoric (Eq. 2.3), respectively.

	Configuration A	Configuration B	Configuration C	Configuration D	Configuration E	Configuration F
Filter 1	N=4	N=4	N=4	N=5	N=5	N=5
	R=4	R=4	R=4	R=4.5	R=4.5	R=4.5
Filter 2	N=4	N=4	N=4	N=5	N=4	N=5
	R=4	R=4	R=4	R=4.6	R=4.6	R=4.5
Filter 3	N=4	N=4	N=4	N=4	N=4	N=4
	R=4.2	R=4.2	R=4.2	R=3.7	R=3.7	R=3.7
Filter 4	N=4	N=4	N=4	N=4	N=4	N=4
	R=4.2	R=4.2	R=4.2	R=4.2	R=3.8	R=3.8
Filter 5	N=4	N=4	N=4	N=4	N=4	N=4
	R=4.2	R=4.2	R=4.2	R=4.2	R=4.2	R=4.2

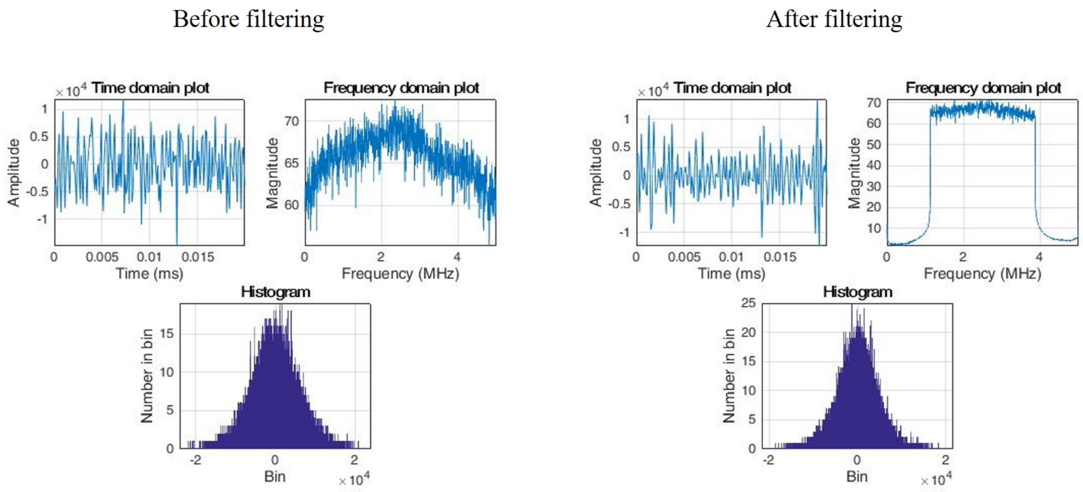

Figure 3.15. Time domain; frequency domain and histogram of the samples of experiment II (RF gain= 0 dB, GPS in-line gain = 30 dB) before (left) and after Chebyshev filtering (right).

It is clearly seen in this figure that before applying the filter the SDR was able to acquire five satellites, but after the USRP output data are filtered, two more

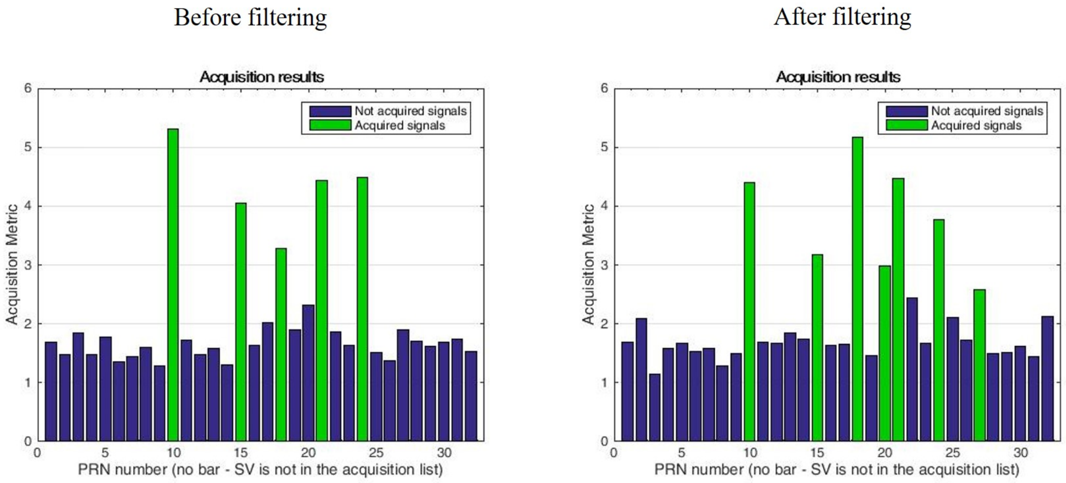

Figure 3.16. Signal acquisition results for experiment II (RF gain= 0 dB, GPS inline gain = 30 dB) before (left) and after filtering (right). After filtering, two more satellites are acquired.

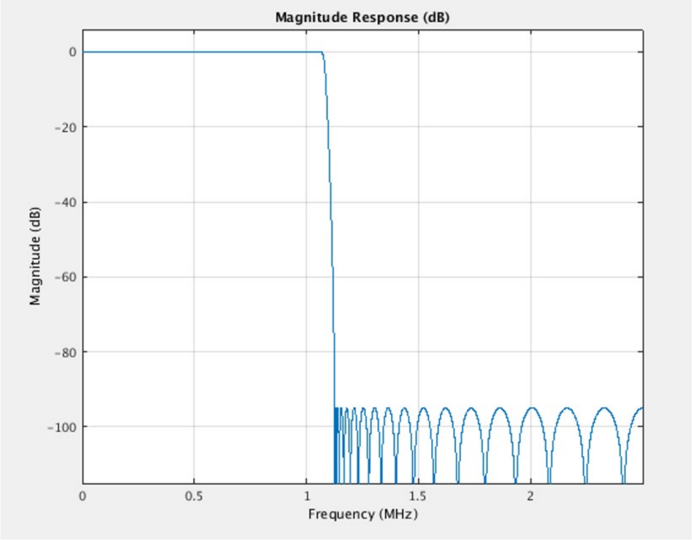

Figure 3.17. Frequency Response of the designed low pass filter

satellites are acquired. All satellites are visible satellites [52]. Figure 3.17 presents the impulse response of the selected low-pass filter, the Chebyshev Type II.

In conclusion, after lab tests with simulated signals and field data from the actual GPS constellation, the USRP is able to acquire actual GPS signals using the

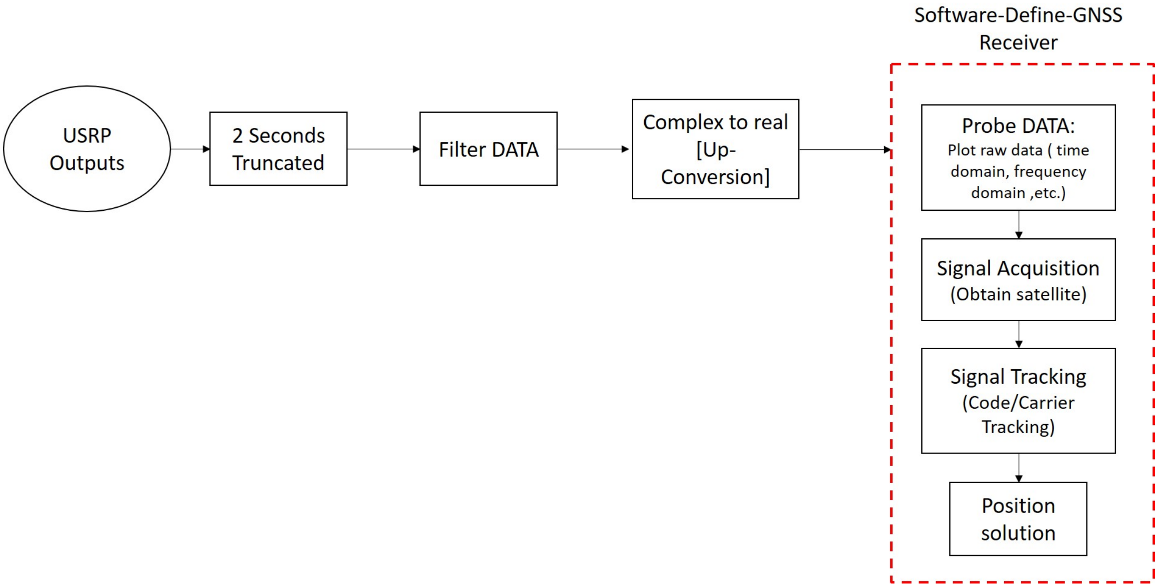

Figure 3.18. Final Signal preconditioning process before feeding to the SDR

USRP-SDR system. The final USRP output data processing includes: 1) truncating the first two seconds of data; 2) filtering out noise by applying a low pass filter; and 3) converting samples from complex to real, as summarized in Figure 3.18.

3.3 Dual-USRP configuration

To collect both direct and reflected GPS signals from two different antennas, two USRPs are needed: one to process the GNSS direct antenna signal, and the other to process the reflection antenna signal. The two USRPs must operate simultaneously, so two possible dual-USRP configurations were tested. There are two ways to connect the dual-USRPs to a PC: either by using a MIMO cable connecting the USRPs to each other (Figure 3.19) or by a gigabit ethernet switch (Figure 3.20).

In the MIMO cable setup, both USRPs can be chosen to use the same clock so that one of them operates as primary and the other one as secondary. In this configuration, the secondary USRP would use the primary USRP's clock. With the

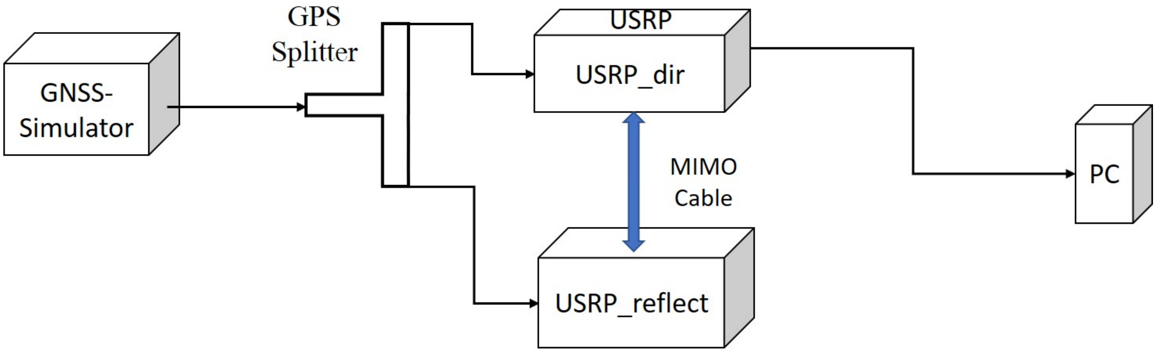

Figure 3.19. Dual-USRP system using a MIMO cable with a primary and secondary USRP.

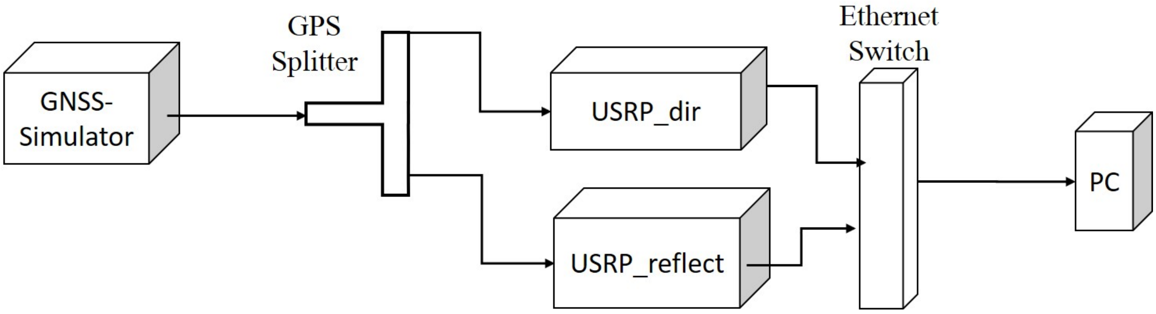

Figure 3.20. Dual-USRP System using a gigabit ethernet switch.

ethernet switch, each USRP operates independently without synchronization (however, see Section 3.4). The purpose of the lab tests of these dual-USRP architectures is to determine a configuration that can effectively collect both data streams simultaneously. An added benefit of the MIMO configuration is the timing synchronization, but that is less critical a requirement for the system than the ability to send the data to the storage device. Each USRP is first assigned a unique name and IP address. One of the USRPs is designated to receive the direct GNSS signal. Its name and

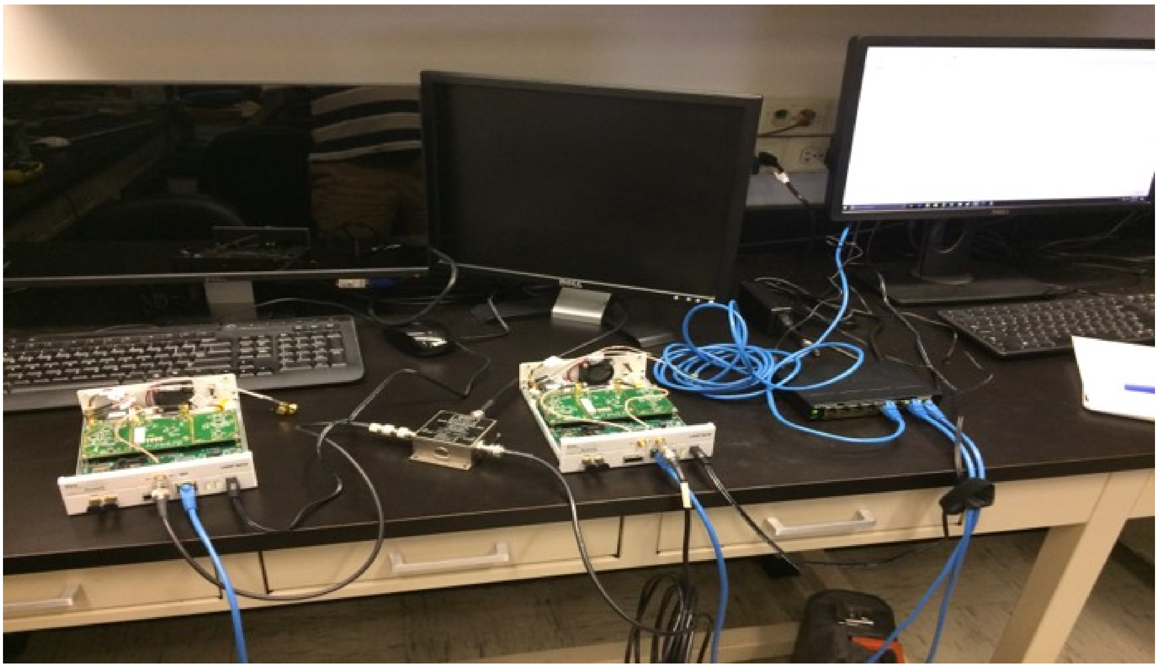

Figure 3.21. Dual USRP System set up for testing with simulator. Facilities provided by the NavLab at IIT.

IP address are changed to USRP_dir and 192.168.10.2, respectively. Similarly, the name and IP address of the USRP used for reflected GNSS signals are modified to USRP_reflect and 192.168.10.3. A python script commands both USRPs to operate simultaneously with their corresponding data and respective configurations stored at the PC. To test our MIMO system in the lab, both USRPs are connected to the same simulator through the GPS splitter, such that both USRPs have identical inputs.

While the MIMO cable offers the advantage of synchronization, the gigabit ethernet switch method is preferable due to buffer overflow errors we encountered in testing, as described in detail in Section 3.2.3 with the MIMO cable (Figure 3.19). Buffer overflow is the error message and a user will get this error message when the speed at which data is written into the hard-drive is less than the speed of the incoming data (sampling rate and data transfer rate). In this situation USRPs will start to lose some of the samples (Figure 3.22). Figure 3.20 represents our selected final dual-USRP system.

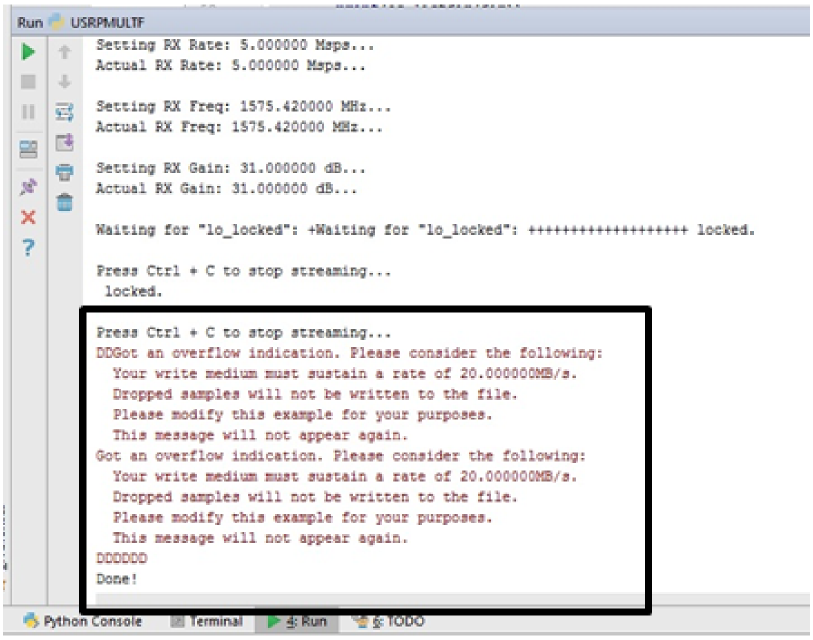

```
Setting RX Rate: 5.000000 Msps...
Actual RX Rate: 5.000000 Msps...

Setting RX Freq: 1575.420000 MHz...
Actual RX Freq: 1575.420000 MHz...

Setting RX Gain: 31.000000 dB...
Actual RX Gain: 31.000000 dB...

Waiting for "lo_locked": +Waiting for "lo_locked": +++++++++++++++++++ locked.

Press Ctrl + C to stop streaming...
 locked.

Press Ctrl + C to stop streaming...
DDGot an overflow indication. Please consider the following:
  Your write medium must sustain a rate of 20.000000MB/s.
  Dropped samples will not be written to the file.
  Please modify this example for your purposes.
  This message will not appear again.
Got an overflow indication. Please consider the following:
  Your write medium must sustain a rate of 20.000000MB/s.
  Dropped samples will not be written to the file.
  Please modify this example for your purposes.
  This message will not appear again.
DDDDDD
Done!
```

Figure 3.22. Screen capture of buffer overflow indication error, which occurs when the write-to-medium rate drops below 20 MB/s.

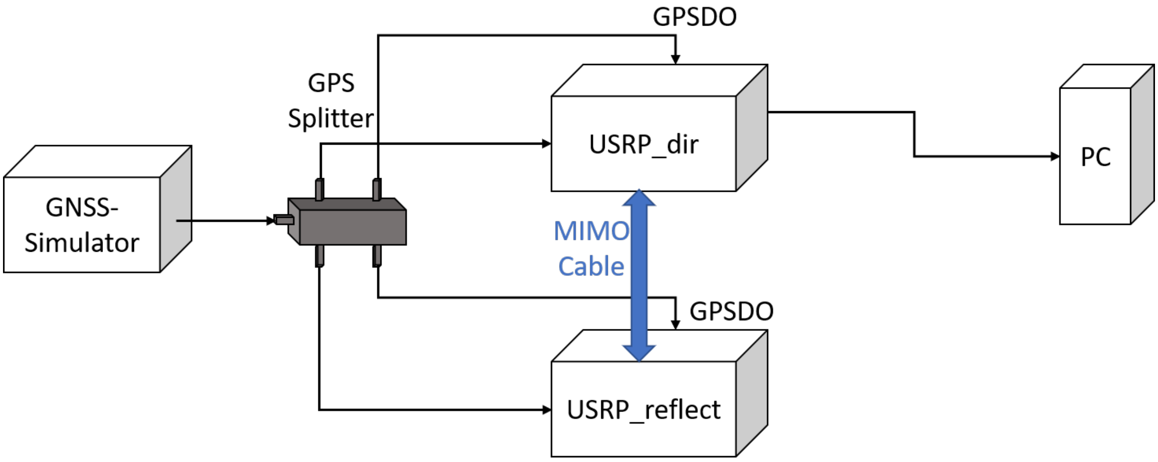

Figure 3.23. Dual-USRP system using a MIMO cable with GPSDO internal clocks.

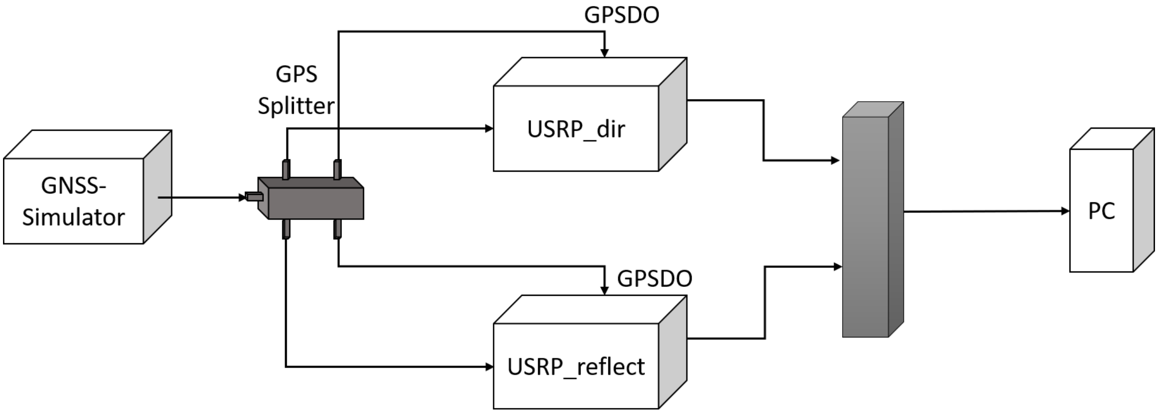

Figure 3.24. Dual-USRP system using a gigabit ethernet switch with GPSDO internal clocks.

3.4 USRP GPS-disciplined oscillator (GPSDO)

In the previous section, the MIMO cable allowed for synchronization between USRPs. To have more accurate clocks, each USRP's oscillator can be driven by a GPS-disciplined oscillator (GPSDO). The GPSDO is installed in the back of each USRP, as shown in Figure 3.2. The GPSDO is directly connected to the USRP's daughterboard (see [21] for more details about the USRP-GPSDO installation). Once the USRP N210 detects the GPSDO, the USRP internal clock is automatically set as the GPSDO. The GPSDO requires a separate GPS antenna input for driving the clock. Because the primary application of these USRPs is itself processing signals from GPS antennas, the direct antenna line is fed as input to each GPSDO using a splitter. Our sensor system is tested with and without the GPSDO to assure the stability of the system using direct GNSS signals for satellite acquisition 3.24. Figure 3.23 shows the dual-USRPs configuration with the MIMO cable when the GPSDO is setup for the USRPs. However, due to the buffering limits discussed in the previous section, this configuration is not used in practice. The final dual-USRP design configuration, with the ethernet switch using the GPSDO in each USRP, is illustrated in Figure

3.24 when connected to a GNSS simulator. The use of the GPSDO means that the clocks are more accurate, and since driven by timing synchronized to GPS time, the USRP clocks are synchronized.

3.5 Auxiliary sensors

The purpose of the auxiliary sensors is to provide a “truth” reference for the surface conditions in the vicinity of the sensors. The complementary sensors include one lidar, up to three optical cameras, and a weather station.

3.5.1 Lidar. One of the primary environmental sensors to which the GNSS-R techniques will be referenced is lidar. The surface at the specular point upon collection of reflected GPS signals is to be characterized by a 3-dimensional surface generated by the point cloud of lidar range and intensity measurements. The lidar unit to be used in the spatial analysis of the lake surface is the Velodyne VLP-16 “puck.” The lidar transmits a beam of light at 903 nm (infrared) in a 360° azimuth field and 15° above and below the unit’s horizontal, with maximum range of 100 m [2]. The applications of this technology are most commonly surveying, and vehicle and robotic navigation, but for this project we use the lidar for 3-dimensional mapping of the local surface. In contrast to bathymetric lidar, which is dual-frequency with a water-penetrating wavelength for mapping submerged surfaces, the VLP-16 is single frequency. Given that the VLP-16 laser frequency is absorbed by water [62] [30] [9], range and intensity data may be expected from solid ice surfaces, but when the surface is liquid, little to no return data will be produced.

After the dual-USRP system was tested successfully (see Section 3.3), the lidar was coupled to it. The python script was modified to operate the lidar for simultaneous data collection with the USRPs. Initially, the lidar was also connected to the PC via the same gigabit ethernet switch used for the USRPs. However, to reduce the likelihood of buffer overflows encountered in this case, we use a separate ethernet switch to connect the PC to the lidar (see Figure 3.1) [52].

3.5.2 Camera and weather station. For recording visual surface conditions, a camera is mounted as part of the system with a field-of-view that overlaps the lidar scan area of the surface. The surface type of any GPS specular point lying in this overlapping area can then be visually confirmed. The GW2237 IP camera, and for some tests two GW Security CCTV- GW-5050-IP cameras, are collocated to within a meter of the GNSS antennas and lidar as auxiliary instruments of the sensor suite [33]. To join the camera to the sensor system, the python script is extended to cover the cameras too. The cameras connect to the same ethernet switch as the lidar and require a power-over-ethernet switch. A separate external hard drive is used to save lidar and camera data. Figure 3.1 is the schematic of the sensor suite showing how the sensors are connected and communicate with each other. To have the camera images in the appropriate coordinate system (in this work, the reflected antenna coordinate system), lidar point clouds are transformed into the camera coordinate system, whose origin is the center of the camera. When lidar point clouds and camera pixels are mapped to a lidar-camera map, then pixels are mapped to positions in the $\hat{x}, \hat{b}, \hat{u}$ coordinate system (for more information about the lidar-camera map see [33]). From there, the data are transformed to a local east-north-up coordinate system whose origin is at the reflected antenna [33] (see Appendix C).

CHAPTER 4

FIELD TESTS

4.1 Overview

From 2018-2020, eleven data campaigns, or “tests,” were conducted at the shore of Lake Michigan, Chicago, Illinois, for different surface conditions. In this chapter, the configuration details for each campaign are given: the approximate sensor system position, orientation, antennas’ angles, and sampling rate. The data campaigns whose results are shown and discussed in subsequent chapters are: Data Campaign 8 (Location B) and Data Campaign 11.

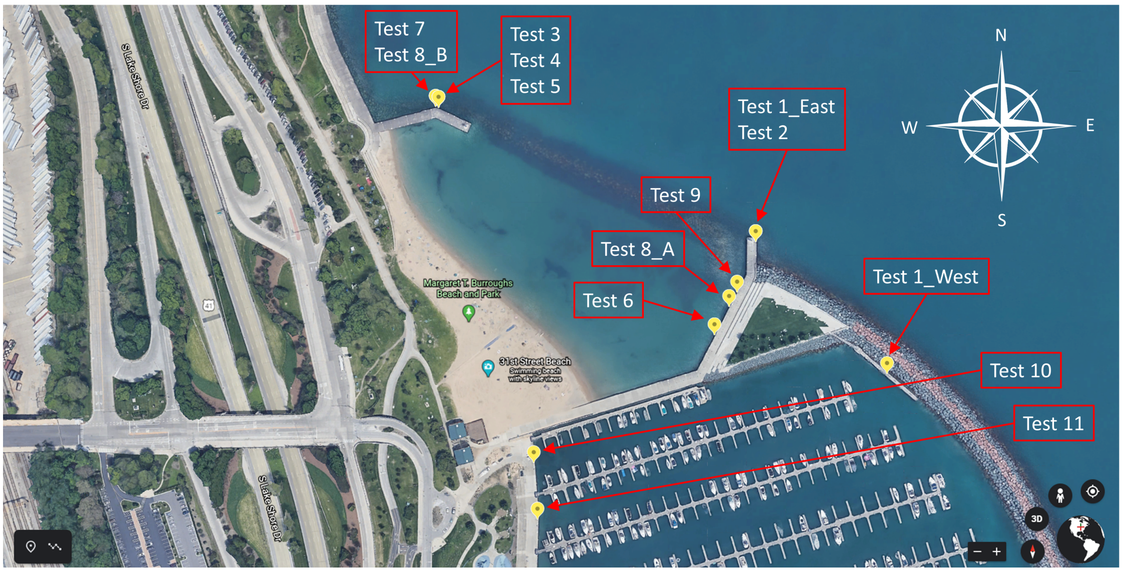

Figure 4.1. Google Map of all data campaign locations at Lake Michigan. [33]

Figure 4.1 shows a Google Map with the campaign sites identified with pins. Approximate sensor position is estimated using photo documentation of the campaign

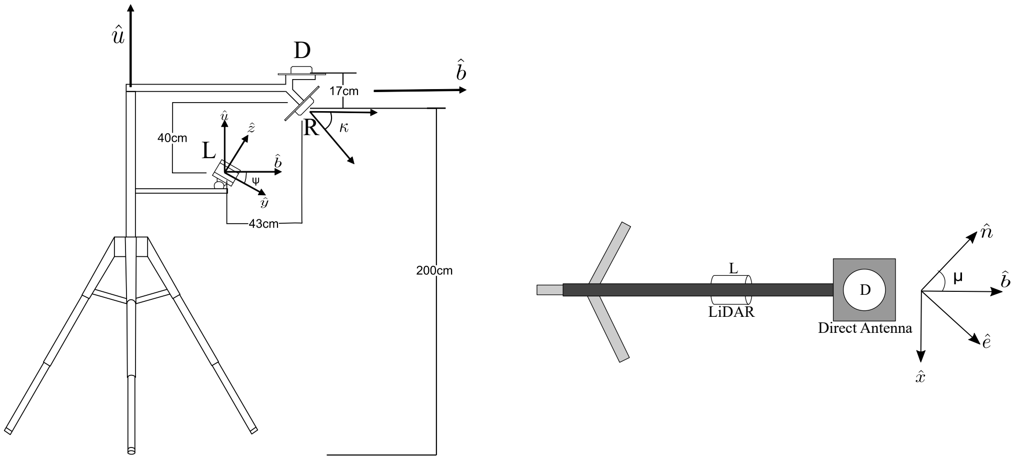

Figure 4.2. Schematic of sensor mounting system and relevant coordinate systems. Left: view from the side. Right: View from above.

site referenced to a Google Earth map. Orientation angles with respect to local north are measured on-site after installation with a magnetic compass. Antenna, lidar, and camera angles are also measured on-site with digital angle measurement tool. For lidar and camera angles, please see [33]. Sampling rate and gain are set with the python script and recorded to a text file at the start of each data collection. In practice, data collection on each test date is divided into 20-minute intervals. Longer duration data collection sometimes led to a buffer overflow recording the USRP data, causing loss of samples. Each campaign is divided into one or more 20-minute parts. Each section below summarizes the key objectives of each data campaign. Tables describing the configuration of each campaign are all listed at the end of the chapter.

4.2 Data Campaign 1

Figure 4.2 illustrates the CAD design of the tripod for data campaigns 1-East and 1-West. A tripod is placed on the ground supporting a 2 m mast oriented vertically upward along $\hat{u}$. The GNSS direct antenna D and reflected antenna R are mounted at the end of a boom that defines a unit vector direction $\hat{b}$. The lidar L

is installed on a lower boom attached to the same tripod and aligned along $\hat{b}$. The heading angle of the system with respect to local north is μ, and the elevation angles of the reflected GNSS antenna and lidar are κ and ψ, respectively.

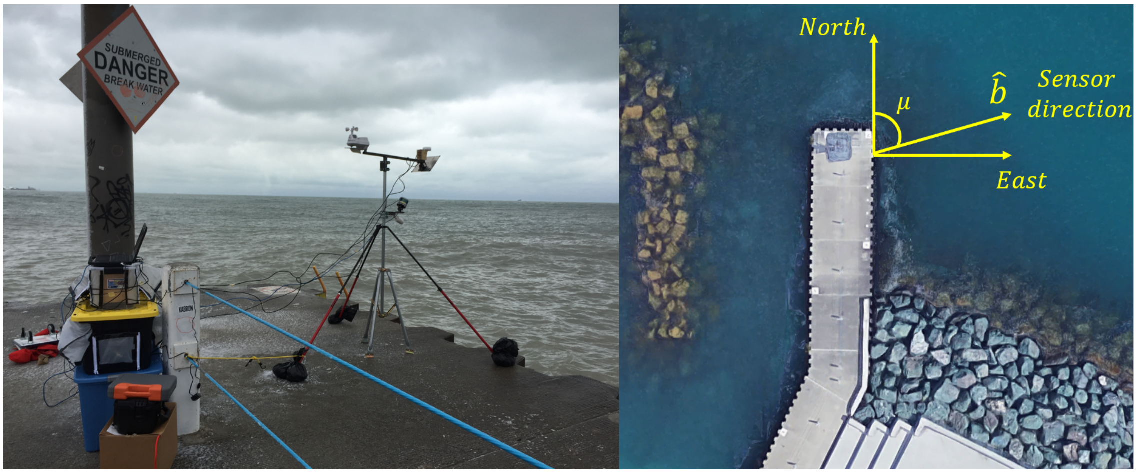

Figure 4.3. Left: Photo of the experiment hardware setup for Test 1-East. Right: Google Map satellite image of sensor location for Test 1-East. The yellow arrow describes the boom direction $\hat{b}$.

Figure 4.4. Left: Photo of the experiment hardware setup for Test 1-West. Right: Google Map satellite image of sensor location for Test 1-West. The yellow arrow describes the boom direction $\hat{b}$.

The purpose of Test 1-East and Test 1-West was to operate the two USRPs and the lidar in the field for ice surface conditions and for water surface conditions. In this test, the sensor suite was set at two different locations. Figure 4.3(left) is a photo of the system field for Test 1-East. For Test 1-East the sensor boom was oriented to the east at a heading of $\mu = 64$ degrees; the surface condition was water (Figure 4.3(right)). For the Test 1-West site, the surface was ice covered, and the sensor boom was pointed to the southwest at $\mu = 208$ degrees (Figure 4.4(right)). Figure 4.4(left) is a photo of the setup for Test 1-West. In this test at both sites, the USRPs used their respective internal clocks (meaning that the GPSDOs were disconnected). The approximate system position as determined by Google Map, reflected antenna angle κ, lidar elevation ψ, sampling rate, GPS inline gains, boom heading μ, surface condition and data collection duration are summarized in Table 4.1. To avoid a USRP data overflow to the computer, each campaign is divided into 20 minutes. Test 1-East has two parts, each with 20 minute length, which means that the total test duration at site 1-East is 40 minutes. Test 1-West has three parts, i.e., the total duration of data collected at Test 1-West is 1 hour.

4.3 Data Campaign 2

From Table 4.1 and subsequent analysis of the Test 1 data, we determined that the gains were connected incorrectly for Test 1-West. The purpose of Test 2 was to set up exercise the process of collecting data with the inline gains connected as intended: using 0 dB from the direct antenna and 30 dB from the reflected antenna. In Test 2, the sensor boom was oriented east, and the surface condition was water. As with Test 1, the USRPs used their internal clocks. The sensor design is same as Test 1 (Figure 4.2). The sensor location is same as Test 1-East (Figure 4.3). Table 4.2 shows the Test 2 configuration details. Test 2 data were collected in three segments of 20 minutes duration each.

4.4 Data Campaign 3

The purpose of this test was to test the effects of antenna gains and ground planes. The antenna gains were increased, to 40 dB inline gain for the reflection antenna and 30 dB for the direct antenna. In this test, the USRPs and lidar were operated again, to collect data from both USRPs and the lidar. Also, following Test 2, it was determined that the lidar data file was empty.

Test 3 data has 4 parts with 20 minute length each, totaling 80 minutes. The lake surface condition for this test was water. Test 3 information is summed up in the Table 4.3. In this test USRP internal clocks are used. The sensor mounting system is as shown in Figure 4.2 for the case with ground plane. For the parts of the test without a ground plane, the ground plane of the directed antenna is removed.

4.5 Data Campaign 4

On Friday March 9, 2018, the fourth test was conducted at Lake Michigan, 31st Street Beach, Chicago 4.1. In this test, in addition to using a ground plane on the reflected antenna, a ground plane was used for the direct antenna also. This is identical to the configuration used in Test 3 for the first 20-minute segment. The lake surface condition was water. Test 4 has 5 parts with 20 minutes duration each. Figure 4.2 shows the sensor CAD design for first 2 parts (part 1-2). Test 4 configuration information is presented in Table 4.4.

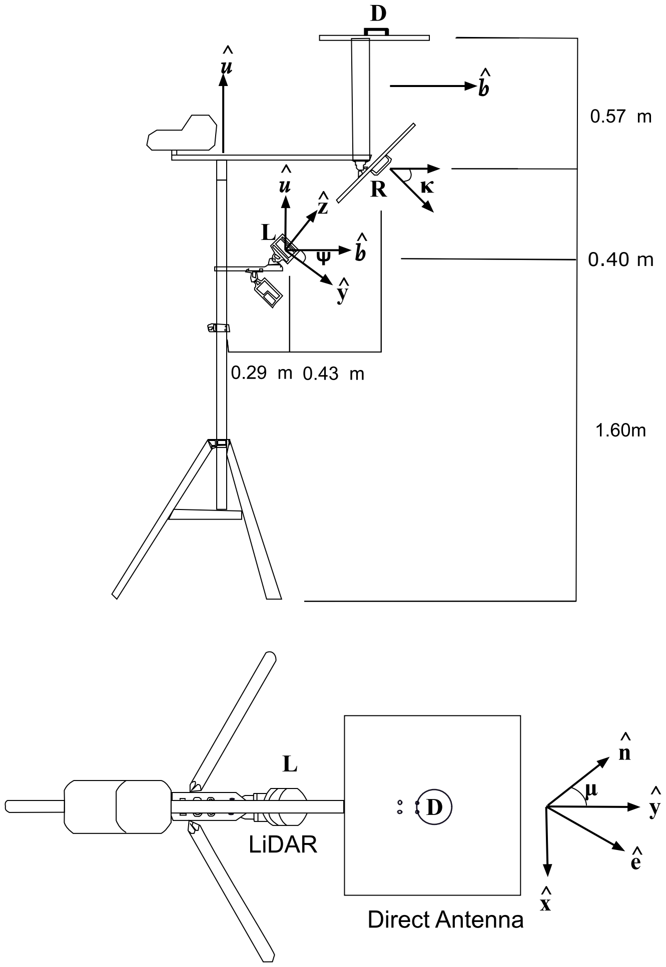

Figure 4.5. Schematic of sensor mounting system and relevant coordinate systems. (Above) Side view. (Below) Top view.

4.6 Data Campaign 5

Test 5 was performed on Thursday July 5, 2018. In this test, the ground planes' size at both antennas is increased in an attempt to further block signals reflected from the back of each antenna. Because of the larger ground planes, the direct antenna must be displaced further vertically from the reflected antenna. The CAD design of this mounting system is illustrated at the Figure 4.5. The test is conducted at a same site of Tests 3-4 at the 31st St. Beach. Figure 4.1 indicates the sensor location on a Google Map. Figure 4.6(left) is a photo of the system on-site, and Figure 4.6(right) shows the sensor orientation on a Google Map satellite image. This is the first test

Figure 4.6. Left: Photo of the experiment hardware setup for Test 5. Right: Google Map satellite image of sensor location for Test 5. The yellow arrow describes the boom direction $\hat{b}$.

for which the camera is activated with the other sensors. To initiate the camera data collection, the software VLC is manually called. The lake surface condition in this test is fresh water. The USRPs' internal clocks are used. Test 5 information is summarized in Table 4.5.

4.7 Data Campaign 6

On January 27, 2019, Test 6 is conducted at 31st Street Beach, Chicago, Illinois, at the same site as Test 5. The configuration is identical to that of Test 5, with big ground planes used for both antennas (Figure 4.5). Even though the temperature was below freezing (13° F), the lake surface condition at the area viewed was water. Small blocks of the ice were floating on the fresh water. The total duration of test 6 data is 40 minutes, in two parts of 20 minutes each. The boom heading was eastward. Test 6 configuration information is given in Table 4.6. In this test, GPSDOs were installed in both USRPs. Each GPSDO was connected to the direct GPS antenna using a GPS splitter. This means that even the GPSDO of the reflected USRP was connected to the direct antenna, only for timing. Effectively, the

USRPs were synchronized using GPS to drive the clock (Figure 3.1). Figure 4.7(left) is a photo of the system on-site, and Figure 4.7(right) shows the sensor orientation on a Google Map satellite image.

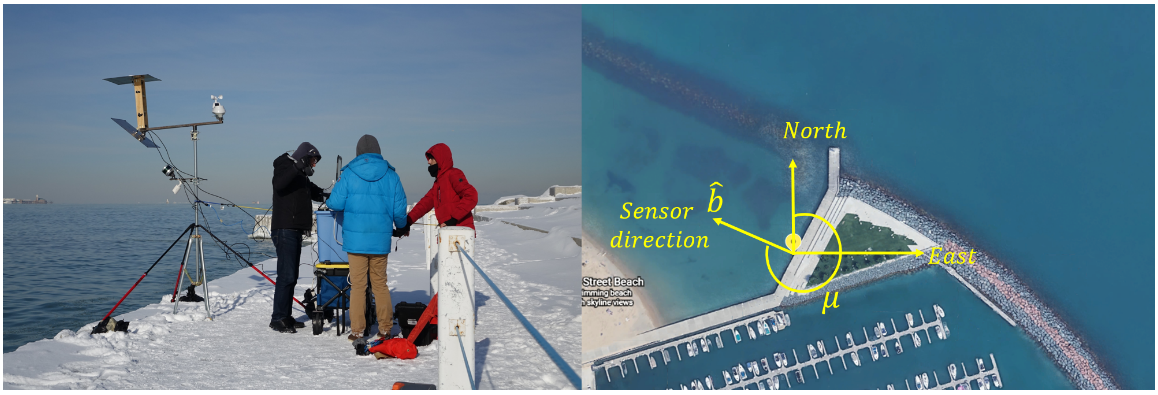

Figure 4.7. Left: Photo of the experiment hardware setup for Test 6. Right: Google Map satellite image of sensor location for Test 6. The yellow arrow describes the boom direction $\hat{b}$.

4.8 Data Campaign 7

Lake Michigan Test 7 is carried out February 1, 2019. Test 7 includes 6 parts, each of 20 minutes duration. The lake surface was ice. In this test, the USRPs' timing was driven by their GPSDOs connected to the direct antenna. Test 7 information is listed in Table 4.7. Test 7 has a different test site than Test 6 at 31st Street Beach, Chicago, Illinois. The sensor system design are the same as for Test 6 (Figure 4.5). Also, 2 hours is the maximum duration of the test due to shortened cycle of the rechargeable power source in cold weather. Figure 4.8(left) is a photo of the system on-site, and Figure 4.8(right) shows the sensor orientation on a Google Map satellite image.

Figure 4.8. Left: Photo of the experiment hardware setup for Test 7. Right: Google Map satellite image of sensor location for Test 7. The yellow arrow describes the boom direction $\hat{b}$.

4.9 Data Campaign 8

Test 8 took place on February 19, 2019, at two locations A and B, as indicated in Figure 4.1. At both locations, the lake surface was covered with ice. Figure 4.9 shows the sensor location, orientation (left) and actual sensor set up at the field (right) at location A. Figure 4.10 (left) is the Google Map of the sensor location/orientation and right is the actual sensor set up at location B. The sensor schematic for this test is in Figure 4.5, identical to Tests 5-7. The USRPs are each driven by their GPSDO connected to the direct antenna, identical to Tests 6-7 (see Figure 3.1). The total duration of Test 8-A data collection is 1 hour, and the total duration of Test 8-B is 80 minutes. Test 8 data campaign information is presented in Table 4.8 for both locations.

4.10 Data Campaign 9

In this data campaign, for the first time 3 cameras are coupled with the sensor suite. Figure 4.12 shows the updated sensor schematics with 3 cameras. In this new setup two new cameras are connected to same power-over-ethernet network switch as

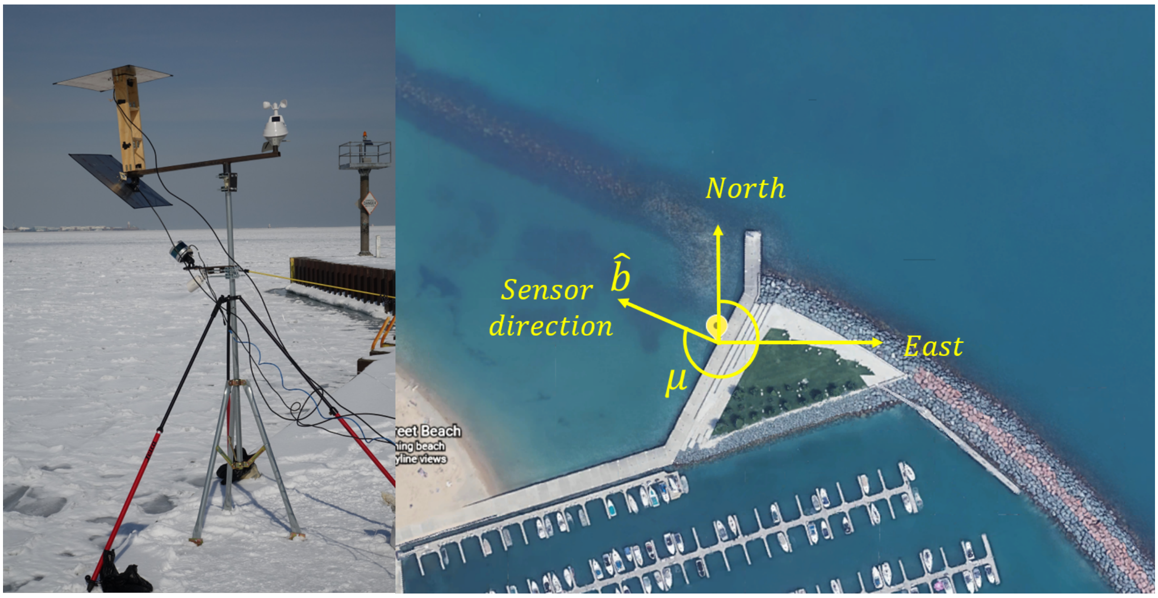

Figure 4.9. Left: Photo of the experiment hardware setup for Test 8 Location A. Right: Google Map satellite image of sensor location for Test 8 Location A. The yellow arrow describes the boom direction $\hat{b}$.

Figure 4.10. Left: Photo of the experiment hardware setup for Test 8 Location B. Right: Google Map satellite image of sensor location for Test 8 Location B. The yellow arrow describes the boom direction $\hat{b}$.

the first camera. The reason to add two more cameras is to have a wider field imaged of the surface, since our first camera only covered a small portion of the surface. The purpose of this data campaign is to check the three-camera system. Data Campaign information is summarized in Table 4.9. Figure 4.11 (left) is a photo of the sensor suite in the field for this data campaign. Figure 4.11 (right) is the Google Map of the sensor location and direction.

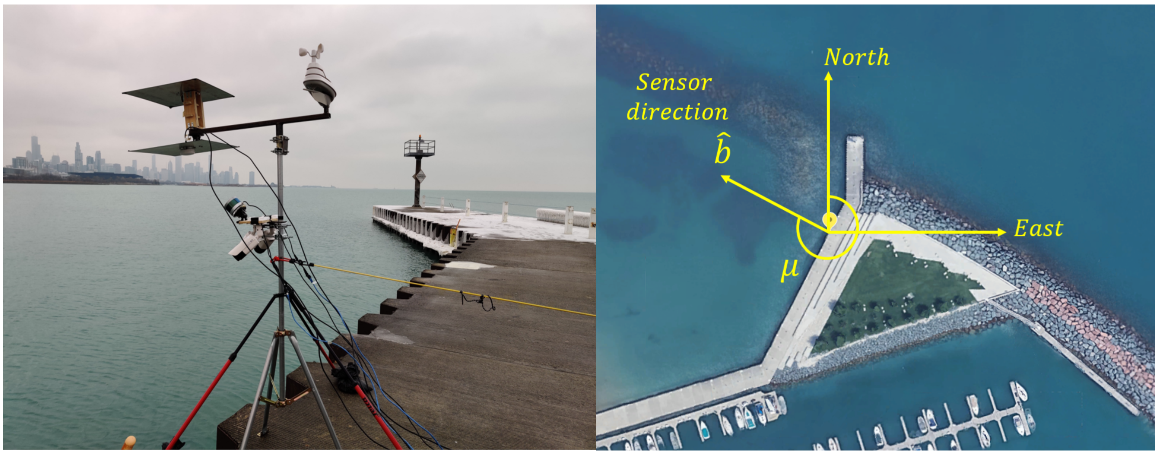

Figure 4.11. Left: Photo of the experiment hardware setup for Test 9. Right: Google Map satellite image of sensor location for Test 9. The yellow arrow describes the boom direction $\hat{b}$.

4.11 Data Campaign 10

Data Campaign 10 is held on February 14, 2020, when the lake surface condition was mixed ice and water. Figure 4.13 shows a photo of the sensor system onsite and a Google Map of the sensor position and orientation. Data Campaign 10 information is summarized in Table 4.10.

4.12 Data Campaign 11

The last data campaign described in this work was conducted February 21, 2020. The surface condition was mixed ice and water. A photo of the sensor system onsite and a map of the sensor position and direction are shown in Figure 4.13. Data Campaign 11 information is listed in Table 4.11.

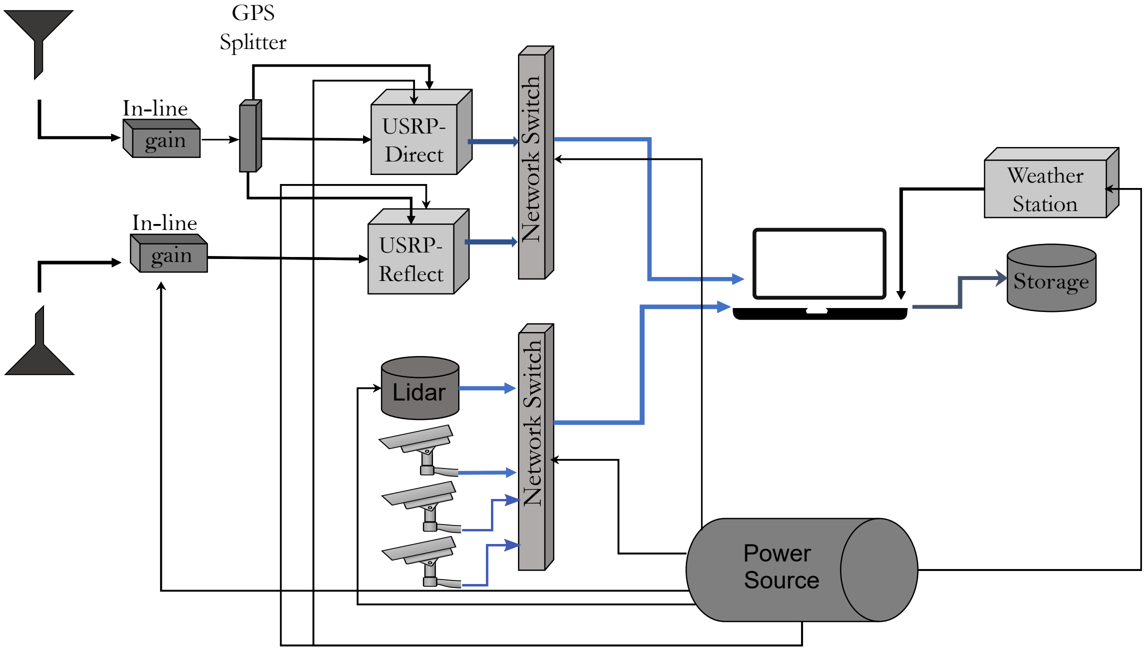

Figure 4.12. Sensor system schematic with three cameras.

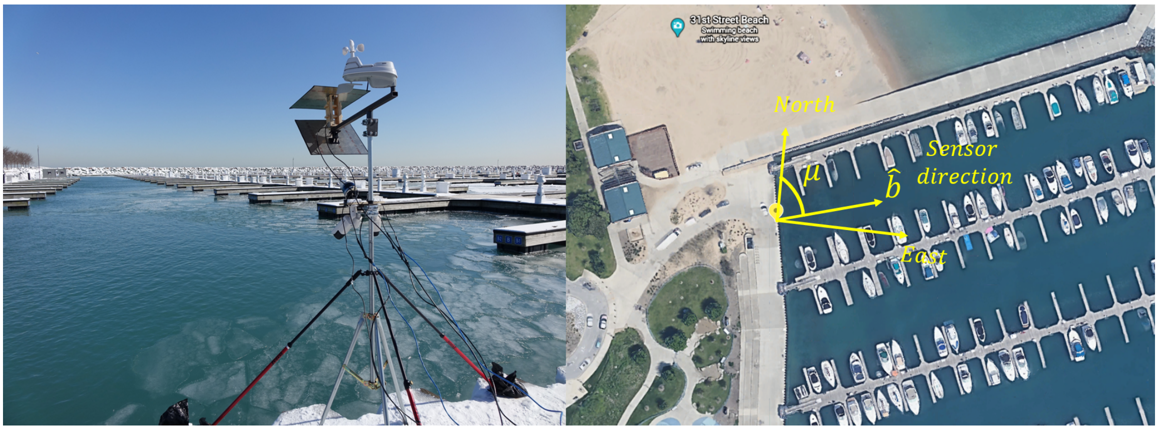

Figure 4.13. Left: Photo of the experiment hardware setup for Test 10. Right: Google Map satellite image of sensor location for Test 10. The yellow arrow describes the boom direction $\hat{b}$.

Figure 4.14. Left: Photo of the experiment hardware setup for Test 11. Right: Google Map satellite image of sensor location for Test 11. The yellow arrow describes the boom direction $\hat{b}$.

Table 4.1. Lake Michigan data collection campaign information Test 1.

Data campaign	Test 1-East	Test 1-West
Time (CST)	Tue Jan 23, 2018 12:41:48	Tue Jan 23, 2018 14:35:48
Sensor Location	latitude : $41.83979°$ longitude :$-87.60421°$	latitude : $41.83893°$ longitude :$-87.60306°$
Sample rate	5 MHz	5 MHz
USRP_dir inline gain	0 dB	30 dB
USRP_ref inline gain	30 dB	0 dB
USRP_dir RF gain	31 dB	31 dB
USRP_ref RF gain	31 dB	31 dB
Ground plane dimension direct	None	None
Ground plane dimension reflected	10.125" x 10.125" x 0.06"	10.125" x 10.125" x 0.06"
Clock used	internal TCXO	internal TCXO
Heading μ	$64°$	$208°$
Elevation angle of the reflected antenna	$-45°$	$-45°$
Elevation angle of the lidar ψ	$-30°$	$-30°$
Number of 20-minute parts	2	3
Surface condition	water	ice/snow

Table 4.2. Lake Michigan data collection campaign information Test 2

Data Campaign	Test 2
Date	Thu Feb 22 2018
Sensor Location	latitude : $41.83979°$ longitude :$-87.60421°$
Sample rate	5 MHz
USRP_dir inline gain	0 dB
USRP_ref inline gain	30 dB
USRP_dir RF gain	31 dB
USRP_ref RF gain	31 dB
Ground plane dimension direct	Not Used
Ground plane dimension reflected	10.125” x 10.125” x 0.06”
Clock used	internal TCXO
Heading μ	67° NE
Elevation angle of the reflected antenna	$-45°$
Elevation angle of the lidar ψ	$-45°$
Number of 20-minute parts	3
Surface condition	water

Table 4.3. Lake Michigan data collection campaign information Test 3.

Data campaign info	Test 3
Date	Fri March 2 2018
Sensor Location	latitude : 41.84066° longitude :$-87.60698°$
Sample rate	5 MHz
USRP_dir inline gain	0 dB
USRP_ref inline gain	30 dB
USRP_dir RF gain	31 dB
USRP_ref RF gain	31 dB
Ground plane dimension direct	10.125" x 10.125" x 0.06"
Ground plane dimension reflected	10.125" x 10.125" x 0.06"
Clock used	internal TCXO
Heading μ	60°NE
Elevation angle of the reflected antenna	$-45°$
Elevation angle of the lidar ψ	$-30°$
Number of 20-minute parts	4
Surface condition	water

Table 4.4. Lake Michigan data collection campaign information Test 4.

Data campaign info	Test 4
Date	Fri March 9 2018
Sensor Location	latitude : 41.84066° longitude :$-87.60698°$
Sample rate	5 MHz
USRP_dir inline gain	30 dB
USRP_ref inline gain	40 dB
USRP_dir RF gain	31 dB
USRP_ref RF gain	31 dB
Ground plane dimension direct	10.125” x 10.125” x 0.06”
Ground plane dimension reflected	10.125” x 10.125” x 0.06”
Clock used	internal TCXO
Heading μ	60° NE
Elevation angle of the reflected antenna	$-45°$
Elevation angle of the lidar ψ	$-30°$
Number of 20-minute parts	5
Surface condition	water

Table 4.5. Lake Michigan data collection campaign information Test 5.

Data Campaign	Test 5
Date	Thu Jul 5 2018
Sensor Location	latitude : 41.84066° longitude :-87.60698°
Sample rate	5 MHz
USRP_dir inline gain	30 dB
USRP_ref inline gain	40 dB
USRP_dir RF gain	31 dB
USRP_ref RF gain	31 dB
Ground plane dimension direct	19.6875” x 19.6875” x 0.04”
Ground plane dimension reflected	19.6875” x 19.6875” x 0.04”
Clock used	internal TCXO
Heading μ	60° NE
Elevation angle of the reflected antenna	-45°
Elevation angle of the lidar ψ	-45°
Number of 20-minute parts	4
Surface condition	water

Table 4.6. Lake Michigan data collection campaign information Test 6.

Data Campaign	Test 6
Date	Fri March 2 2018
Sensor Location	latitude : 41.83918° longitude :$-87.60457°$
Sample rate	5 MHz
USRP_dir inline gain	30 dB
USRP_ref inline gain	40 dB
USRP_dir RF gain	31 dB
USRP_ref RF gain	31 dB
Ground plane dimension direct	19.6875” x 19.6875” x 0.04”
Ground plane dimension reflected	19.6875” x 19.6875” x 0.04”
Clock used	GPSDO
Heading μ	350° NW
Elevation angle of the reflected antenna	$-45°$
Elevation angle of the lidar ψ	$-45°$
Number of 20-minute parts	2
Surface condition	water

Table 4.7. Lake Michigan data collection campaign information Test 7

Data Campaign	Test 7
Date	Fri Feb 1 2019
Sensor Location	latitude : 41.84066° longitude :$-87.60701°$
Sample rate	5 MHz
USRP_dir inline gain	30 dB
USRP_ref inline gain	40 dB
USRP_dir RF gain	31 dB
USRP_ref RF gain	31 dB
Ground plane dimension direct	19.6875" x 19.6875" x 0.04"
Ground plane dimension reflected	19.6875" x 19.6875" x 0.04"
Clock used	GPSDO
Heading μ	330° NW
Elevation angle of the reflected antenna	$-45°$
Elevation angle of the lidar ψ	$-45°$
Number of 20-minute parts	6
Surface condition	water

Table 4.8. Lake Michigan data collection campaign information for Data campaign 8 for both locations (A and B).

Data Campaign	Test 8 (Location A)	Test 8 (Location B)
Date	Tue Feb 19 12:41:48 2019	Tue Feb 19 15:28:48 2019
Sensor Location	latitude : 41.83936° longitude :$-87.60444°$	latitude : 41.84066° longitude :$-87.60701°$
Sample rate	5 MHz	5 MHz
USRP_dir inline gain	30 dB	30 dB
USRP_ref inline gain	40 dB	40 dB
USRP_dir RF gain	31 dB	31 dB
USRP_ref RF gain	31 dB	31 dB
Ground plane dimension direct	19.6875" x 19.6875" x 0.04"	19.6875" x 19.6875" x 0.04"
Ground plane dimension reflected	19.6875" x 19.6875" x 0.04"	19.6875" x 19.6875" x 0.04"
Clock used	GPSDO	GPSDO
Heading μ	218° NW	350° NW
Elevation angle of the reflected antenna	$-45°$	$-45°$
Elevation angle of the lidar ψ	$-45°$	$-45°$
Number of 20-minute parts	3	4
Surface condition	ice/snow covered	ice/snow covered

Table 4.9. Lake Michigan data collection campaign information Test 9

Data Campaign	Test 9
Date	Fri Jan 31 2020
Sensor Location	latitude : 41.83946° longitude :−87.60437°
Sample rate	5 MHz
USRP_dir inline gain	30 dB
USRP_ref inline gain	40 dB
USRP_dir RF gain	31 dB
USRP_ref RF gain	31 dB
Ground plane dimension direct	19.6875” x 19.6875” x 0.04”
Ground plane dimension reflected	19.6875” x 19.6875” x 0.04”
Clock used	GPSDO
Heading μ	70°
Elevation angle of the reflected antenna	−45°
Elevation angle of the lidar ψ	−45°
Number of 20-minute parts	2
Surface condition	water

Table 4.10. Lake Michigan data collection campaign information Test 10

Data Campaign	Test 10
Date	Fri Feb 14 2020
Sensor Location	latitude : 41.83835° longitude :$-87.60615°$
Sample rate	5 MHz
USRP_dir inline gain	30 dB
USRP_ref inline gain	40 dB
Ground plane dimension direct	19.6875” x 19.6875” x 0.04”
Ground plane dimension reflected	19.6875” x 19.6875” x 0.04”
Clock used	GPSDO
Heading μ	70°
Elevation angle of the reflected antenna	$-45°$
Elevation angle of the lidar ψ	$-45°$
Number of 20-minute parts	9
Surface condition	Mixed water/ice

Table 4.11. Lake Michigan data collection campaign information Test 11

Data Campaign	Test 11
Date	Fri Feb 21 2020
Sensor Location	latitude : 41.83798° longitude :$-87.60612°$
Sample rate	5 MHz
USRP_dir inline gain	30 dB
USRP_ref inline gain	40 dB
USRP_dir RF gain	31 dB
USRP_ref RF gain	31 dB
Ground plane dimension direct	19.6875” x 19.6875” x 0.04”
Ground plane dimension reflected	19.6875” x 19.6875” x 0.04”
Clock used	GPSDO
Heading μ	70°
Elevation angle of the reflected antenna	$-45°$
Elevation angle of the lidar ψ	$-45°$
Number of 20-minute parts	8
Surface condition	Mixed ice and water

CHAPTER 5

NEW SIGNAL PROCESSING METHOD FOR ACQUISITION

5.1 Overview

This chapter develops a new signal processing method to detect and acquire Global Navigation Satellite System (GNSS) signals reflected from the nearby environment. The method of modified differential coherent integration multiplies time-shifted auto-correlation samples. The new method is compared to two conventional Global Positioning System (GPS) signal acquisition methods—coherent integration and coherent integration plus incoherent detection —as well as an existing differential coherent integration method. To test and compare these methods, GPS front-end signals were collected from both a directly receiving antenna facing upward and from a reflection-receiving antenna facing downward during data campaign Test 8 (location B) on Lake Michigan, Chicago, as described in Chapter 4. The front-end samples are saved and brought to the lab for post-processing and analysis. Visible satellite locations are computed based on satellite almanacs [60]. The proposed method and three baseline methods are evaluated for 2 ms and 10 ms coherent integration of the data from the directly-receiving antenna. Coherent integration and the proposed method are compared for 1 ms integration time as well. The performance criteria compared are acquisition metric, the number of correctly detected satellites, false alarms, and missed detections. We also compare the performance of the methods when applied to data from the reflection-receiving antenna. The new method of modified differential coherent integration increases the acquisition metric. Unlike conventional differential coherent integration, it can be performed on as little as 1 ms of front-end data. The new method is the only one of the four compared that acquires satellites in the reflected GPS signals, with three acquired using 10 ms of integration.

This chapter is organized as follows: Section 5.2 describes the new GPS signal acquisition method. Section 5.3 describes how the new method is evaluated and compared with the three existing methods. Section 5.4 describes the experimental setup and shows the satellites visible during data collection. Section 5.5 shows the results of this study and, finally, section 5.6 concludes.

5.2 Proposed acquisition method

In this chapter, I introduce a new version of the differential correlation operation that was reviewed in Section 2.5.3. I will refer to the new method as "modified differential" (MDI) integration. The *element* of the correlation output $\tilde{\tilde{S}}$ from Eq. (2.16) at time shift m is correlated with the previous time shift element $\tilde{\tilde{S}}$ at time shift $m-1$. Then the neighboring elements in delay space are highly correlated with each other in the vicinity of the correlation peak, and are not correlated elsewhere or when random noise is present [45] [48]. To perform this operation let $\tilde{\tilde{S}}_m$ be the complex correlation output element picked out from Eq. (2.16) for the m^{th} time shift for a single Doppler f_D. Substituting in Eqs. (2.9) (2.13) :

$$\tilde{\tilde{S}}_m \equiv \tilde{\tilde{S}}(m, f_D) = \frac{1}{N} \sum_{k=1}^{N_{coh}} \sum_{n=1}^{N} (s_{I,k,n} + j s_{Q,k,n})\, x((n-m)T_s) \tag{5.1}$$

In this expression N is the number of samples in one repetition of the C/A code, N_{coh} is the number of code repetitions to be summed, $s_{I,n}, s_{Q,n}$ are the n^{th} in-phase and quadrature-phase samples given by Eqs.(2.5) (2.6), x is the PRN code, and T_s is the sampling period. Then "modified differential" correlation is:

$$\tilde{U}_m \;=\; \tilde{\tilde{S}}_m \tilde{\tilde{S}}^*_{m-1} \tag{5.2}$$

This makes $\tilde{U}_m$ a single value corresponding to time shift m for Doppler f_D. The full array of $\tilde{U}_m$ is the modified differential integration output (Figure 5.1):

$$\tilde{S}_{\tilde{U}}(f_D) \quad = \quad \left[\tilde{U}_1, \tilde{U}_2, ..., , \tilde{U}_{N-1}, \tilde{U}_N\right] \tag{5.3}$$

whose magnitude can be then used for acquisition.

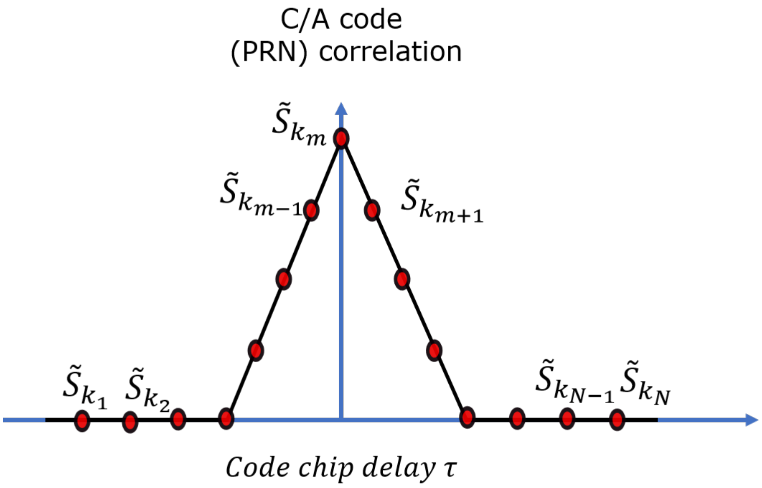

(a) Auto-correlation function.

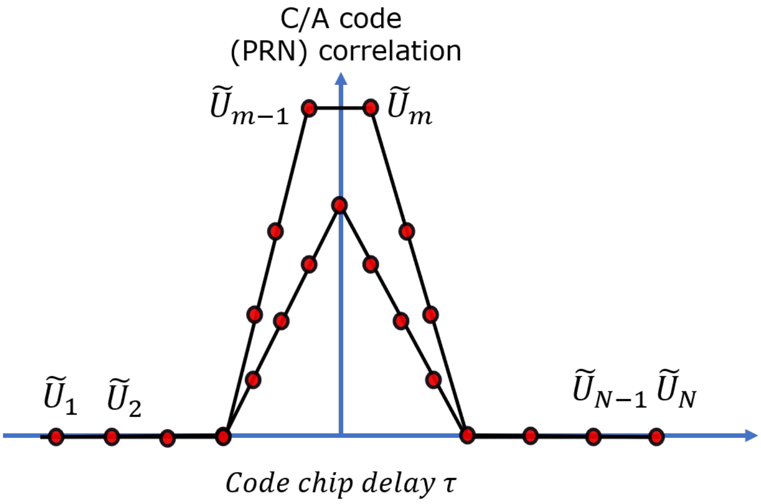

(b) Auto-Correlation function after MDI.

Figure 5.1. Illustration of the auto-correlation function before (a) and after (b) the proposed method (MDI).

Figure 5.2(c) shows the modified differential coherent integration method in

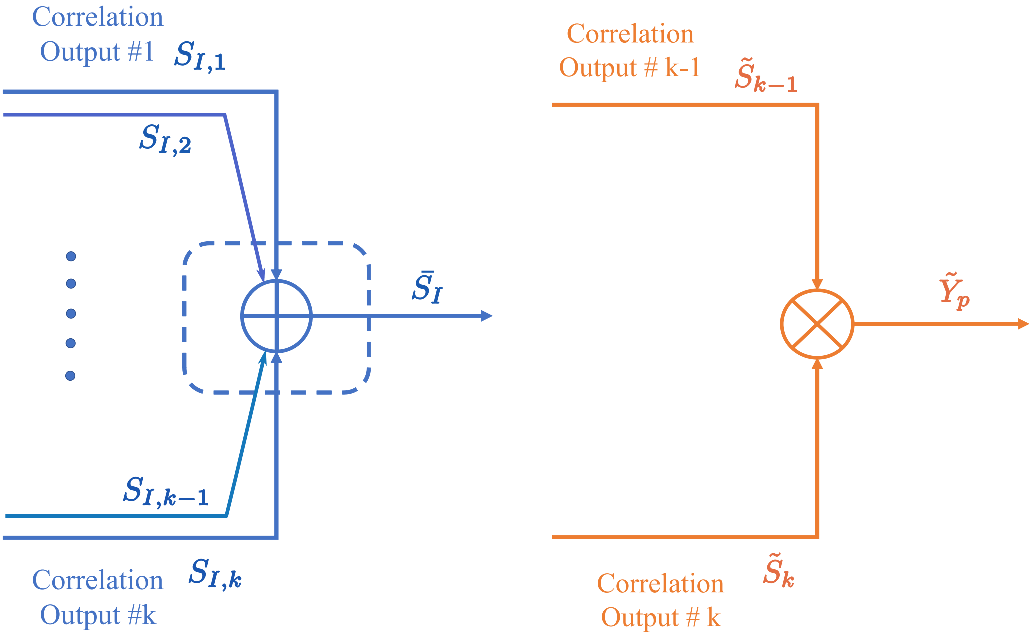

(a) Coherent integration. (b) Differential integration.

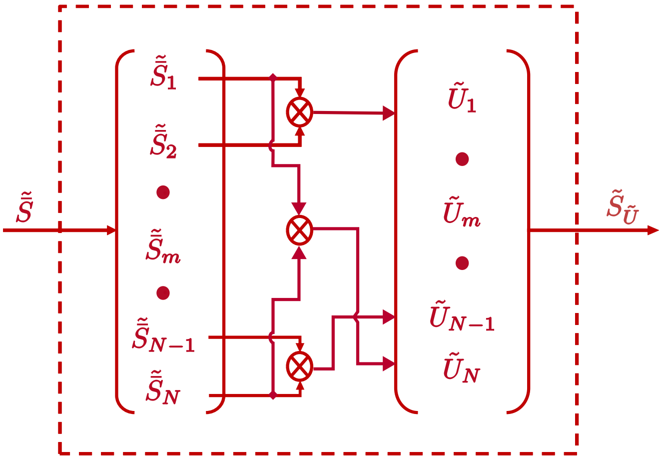

(c) Modified differential integration.

Figure 5.2. Comparison between (a) coherent integration, (b) conventional differential integration, and (c) modified differential integration.

contrast to (5.2(a)) coherent integration and (5.2(b)) conventional differential integration.

5.3 Signal acquisition methods evaluated

In this section three conventional GPS signal acquisition methods and the proposed modified differential method are evaluated. Table 5.1 summarizes these four methods and the five comparison tests used. These methods are analyzed using both signals collected from an upward-facing right-hand circularly polarized antenna (the “direct” signal) and from a downward-facing lefthand circularly polarized antenna (the “reflected” GPS signal). The downward-facing antenna is intended to collect signals reflected from the nearby ice surface. Comparisons 1-3 use the direct signal and comparisons 4-5 use the reflected signal. To make the comparison among methods most nearly equivalent to each other, only the in-phase component is used to the extent possible, and all are tested for identical durations of signal data in a given test. Details on each method to be compared will be given in the subsections that follow.

For Comparison 1 we compare the acquisition metric obtained by methods 1-4 using $T_d = 4$ ms of the direct signal. Comparison 2 compares methods 1-4 using $T_d = 20$ ms of the direct signal. We quantify missed detection rates on a standard desktop machine for these two time intervals. In Comparison 3, we compare methods that use the in-phase component of the signal only for $T_d = 1$ ms. Since Method 2 is incoherent and Method 3 requires two successive correlator outputs (i.e., a minimum of $T_d = 2$ ms of data), only Methods 1 and 4 are compared for $T_d = 1$ ms. Having established the performance of the new method against baseline methods for directly-received data, we finally apply all four methods in Comparison 4 to $T_d = 4$ ms and in Comparison 5 to $T_d = 20$ ms of the reflected GPS data.

Table 5.1. Signal acquisition methods compared.

Comparison	Signal	T_d (ms)	T_1, T_2 (ms)	N_{coh}	Method	$\hat{S}$	Eq.
1	direct	4	2	2	1	S_{coh}	(5.4)
					2	S_{inc}	(5.6)
					3	S_{DC}	(5.10)
					4	S_{MDI}	(5.15)
2	direct	20	10	10	1	S_{coh}	(5.4)
					2	S_{inc}	(5.6)
					3	S_{DC}	(5.10)
					4	S_{MDI}	(5.15)
3	direct	1	1	1	1	S_{coh}	(5.4)
					4	S_{MDI}	(5.15)
4	reflected	4	2	2	1	S_{coh}	(5.4)
					2	S_{inc}	(5.6)
					3	S_{DC}	(5.10)
					4	S_{MDI}	(5.15)
5	reflected	20	10	10	1	S_{coh}	(5.4)
					2	S_{inc}	(5.6)
					3	S_{DC}	(5.10)
					4	S_{MDI}	(5.15)

5.3.1 Method 1: Coherent integration. The conventional signal acquisition method is coherent integration, described previously in Section 2.5.1. Instead of

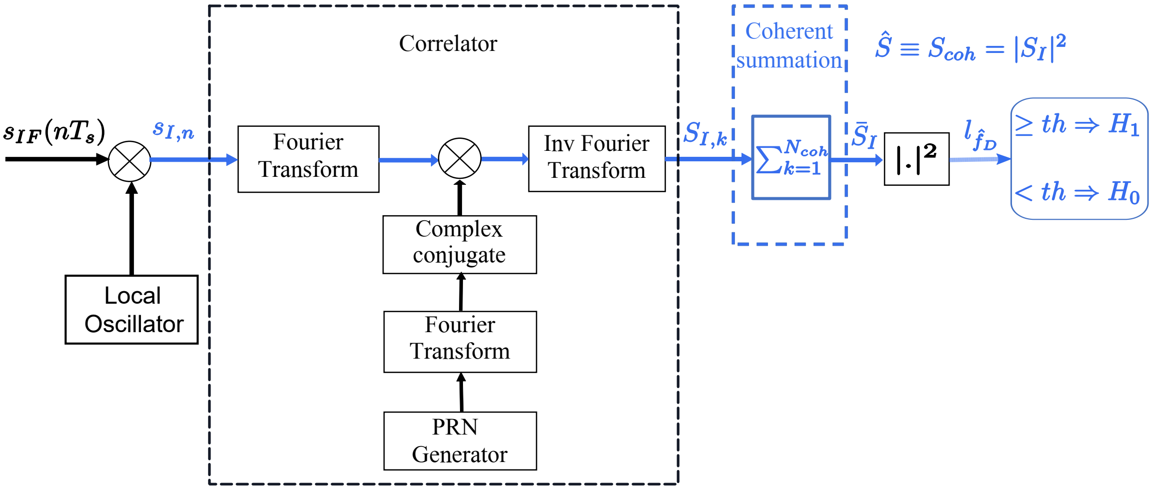

Figure 5.3. Coherent integration via Fast Fourier Transform (Method 1)

computing the correlation of in-phase samples $S_{I,k}$ of Eq. (2.10) in the time domain, the Fast Fourier Transform (FFT) is used to parallelize the correlation operation. The parallel code phase search leverages the fact that correlation of time series is multiplication in the Fourier domain. I use a software-defined received (SDR) that performs the correlation as a parallel code search via the FFT. The FFT signal acquisition method decreases the computation time but increases the computational complexity. Figure 5.3 shows the signal acquisition process for Method 1, with blue arrows and operations emphasizing elements specific to coherent processing. As seen in Figure 5.3, the in-phase samples $s_{I,n}$ of the signal of duration T_{coh} are Fourier transformed and then multiplied by the complex conjugate of the Fourier transform of the replica PRN code x. The product is inverse transformed to produce $S_{I,k}$ equivalent to that shown in Eq. (2.10). Then N_{coh} segments are summed and the real part squared $|\bar{S}_I|^2$, is used as $\hat{S}$ for computing the acquisition metric $l^q_{\hat{f}_D}$ defined in Eq. (2.3).

$$S_{coh} = \begin{cases} |\bar{S}_{I,T_1}|^2, & \max_m(|\bar{S}_{I,T_1}|^2) > \max_m(|\bar{S}_{I,T_2}|^2) \\ |\bar{S}_{I,T_2}|^2, & \text{otherwise} \end{cases} \tag{5.4}$$

$$\hat{S} \equiv S_{coh} \tag{5.5}$$

We evaluate Method 1 for $T_d = 4$ ms in Comparisons 1 and 4; for 20 ms in Comparisons 2 and 5; and for 1 ms in Comparison 3. To avoid the possibility of a navigation data bit transition, when integrating for duration $T_d > 1$ ms, the logic in Eq. (5.4) is used. The frequency search space for coherent integration is ± 10 kHz of the intermediate frequency. For Comparisons 1, 2, 4, and 5 the frequency bin width $\Delta f_D = 100$ Hz. For Comparison 3 which has $T_{coh} = 1$ ms, the Doppler search resolution is $\Delta f_D = 500$ Hz. For this method, the acquisition metric ratio $th = 2.5$, following the convention in [8].

5.3.2 Method 2: Incoherent detection. In this method the magnitude of the complex signal is used for signal acquisition. Figure 5.4 describes method 2, with green arrows and operations describing the incoherent elements of the processing, which now incorporate $s_{Q,n}$. As with Method 1, correlation is completed via parallel code phase search using the FFT, represented in Figure 5.4 by the “correlator” boxes. After coherent summation yields $\bar{S}_I, \bar{S}_Q$ (Eq.(2.13) and (2.14)), the squared magnitude of the complex-valued $\tilde{\bar{S}}$ (Eq (5.1)) is used for the correlation power output.

$$S_{inc} = \begin{cases} |\tilde{\bar{S}}_{T_1}|^2, & \max_m(|\tilde{\bar{S}}_{T_1}|^2) > \max_m(|\tilde{\bar{S}}_{T_2}|^2) \\ |\tilde{\bar{S}}_{T_2}|^2, & \text{otherwise} \end{cases} \tag{5.6}$$

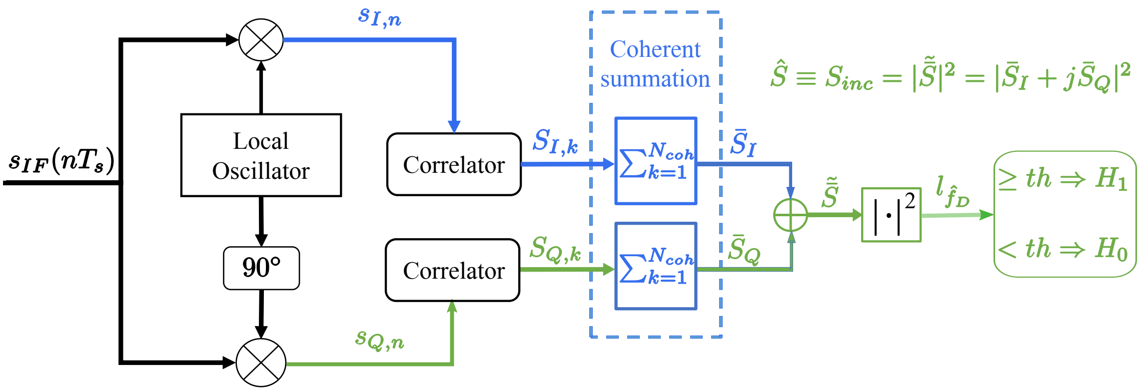

Figure 5.4. Standard incoherent detection (Method 2)

For this method the correlation power is:

$$\hat{S} \equiv S_{inc} \tag{5.7}$$

as given in Eq.(5.6). Method 2 is evaluated for $T_d = 4$ ms in Comparisons 1 and 4, and for $T_d = 20$ ms in Comparisons 2 and 5. For handling the possible data bit transitions, two consecutive data segments of duration $T_1 = T_2 = T_d/2$ are correlated, and the data segment with higher power is selected as $\hat{S}$. The frequency search space for coherent integration is ±10 kHz of the intermediate frequency, with $\Delta f_D = 100$ Hz. For this method, the acquisition metric ratio $th = 2.5$, following the convention in [8].

5.3.3 Method 3: Conventional differential coherent integration. To make this method as closely comparable to the other algorithms as possible, and for simplicity only the in-phase correlator output is used in this method, rather than the more general form introduced in Section 2.5.3. The coherent correlation of the in-phase signal for the k^{th} millisecond $S_{I,k}$ is multiplied by the correlation of the previous segment of length $T_{C/A}$, $S_{I,k-1}$.

$$\begin{aligned} Y_p &= S_{I,k}S_{I,k-1},\ p = 1, 2, ..., N_{coh} - 1 && (5.8)\\ S_Y &= \sum_{p=1}^{N_{coh}-1} Y_p && (5.9)\\ S_{DC} &= \begin{cases} |S_{Y,T_1}|^2, & \max_m(|S_{Y,T_1}|^2) > \max_m(|S_{Y,T_2}|^2) \\ |S_{Y,T_2}|^2, & \text{otherwise} \end{cases} && (5.10) \end{aligned}$$

Figure 5.5 illustrates the conventional differential integration used in this comparison, with the orange box in Figure 5.5 emphasizing the differential operation. Then the real part of the product of the differential coherent operation output is computed for obtaining S_Y. Its squared magnitude is the value used for determining the acquisition metric, as given in Eq. (5.10) to account for data bit transitions. For this method,

$$\hat{S} \equiv S_{DC} \tag{5.11}$$

This method is analyzed for $T_d = 4$ ms and 20 ms. The frequency search space is ±10 kHz of the intermediate frequency, with Δf_D= 100 Hz. For this method, the acquisition metric ratio $th = 4.5$, based on the idea that the complex conjugate multiplication will tend to approximately square correlation output values.

5.3.4 Method 4: Modified differential coherent integration. The implementation of modified differential integration used in this work is shown in the dark red

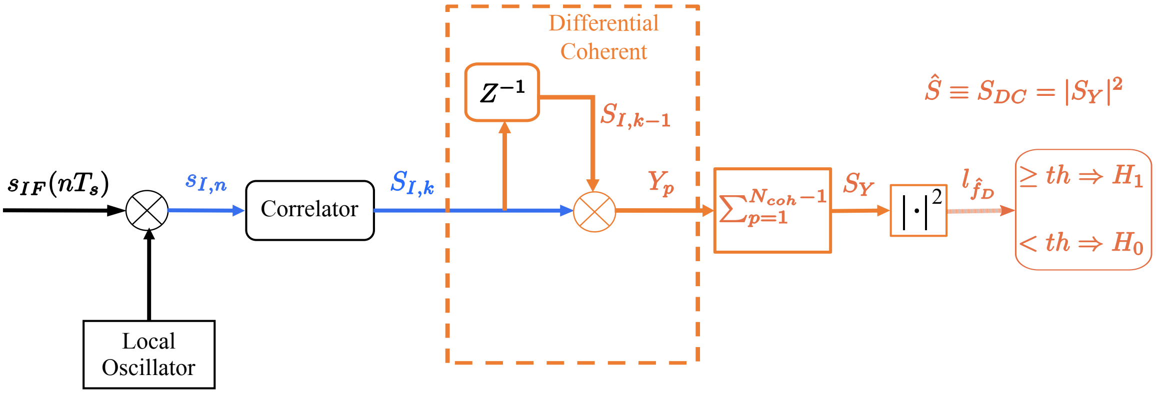

Figure 5.5. Conventional differential coherent integration (Method 3)

box in Figure 5.6. To most closely compare against methods 1-3, again only the in-phase component is used rather than the more general complex form introduced in Section 5.2. The correlation power $\bar{S}_{I_m}$ for the m^{th} time shift is multiplied by the previous correlation sample, $\bar{S}_{I_{m-1}}$ as in Eq. (5.13).

$$\bar{S}_{I_m} \equiv \bar{S}_I(m, f_D) \tag{5.12}$$

$$U_m = \bar{S}_{I_m}\bar{S}_{I_{m-1}} \tag{5.13}$$

Each element of a single array of coherent integration is correlated with the prior element, cyclically, to give an array S_U whose squared magnitude is used for acquisition:

$$S_U(f_D) = [U_1, U_2, ..., , U_{N-1}, U_N] \tag{5.14}$$

For tests with $T_d > 1$ ms, the data bit is accounted for by using Eq. (5.15).

$$S_{MDI} = \begin{cases} |S_{U,T_1}|^2, & \max_m(|S_{U,T_1}|^2) > \max_m(|S_{U,T_2}|^2) \\ |S_{U,T_2}|^2, & \text{otherwise} \end{cases} \tag{5.15}$$

$$\hat{S} \equiv S_{MDI} \tag{5.16}$$

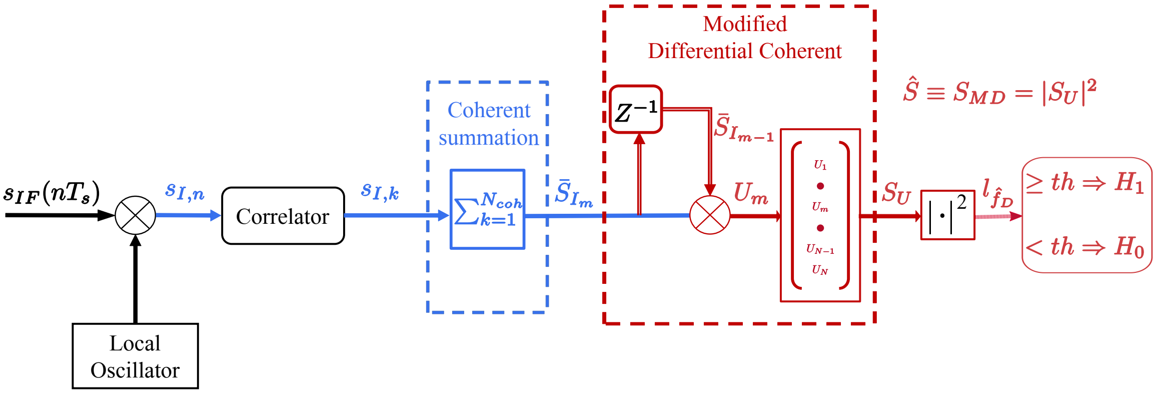

Figure 5.6. “Modified Differential” correlator tested in this work.

This method is evaluated for $T_d = 4$ ms, 20 ms, and 1 ms. The frequency search space for coherent integration is ±10 kHz of the intermediate frequency. For the comparisons whose $T_d > 1$ ms, the resolution $\Delta f_D = 100$ Hz. For $T_d = 1$ ms, the Doppler search resolution is $\Delta f_D = 500$ Hz. These are identical to the resolutions used for the other three methods. The acquisition metric ratio for method 4 is $th = 4.5$ to align with the threshold used for method 3.

5.4 Experimental evaluation

To evaluate the performance of various signal acquisition methods, GPS data collected during Data Campaign 8 (Location B) are analyzed. Details about this sensor system and the data campaign are provided in Section 4.9. A GPS direct antenna and front-end, and GPS reflected antenna and front-end are powered and connected to a laptop for data acquisition. The reflection surface is lake ice. The data are brought into the lab for post-processing. Receiver signal acquisition is implemented in the lab using software to implement the methods described in Section 5.3.

A sky plot of the satellites in view during data collection, computed based on GPS almanac information and the antenna location from Table 4.8 is shown in

#visible satellite for Almanac Week 1017 2-19-2019 at 15:28-15:29 Central Time

Satellite
PRN 05
PRN 07
PRN 08
PRN 09
PRN 11
PRN 16
PRN 18
PRN 23
PRN 26
PRN 27
PRN 28
PRN 30

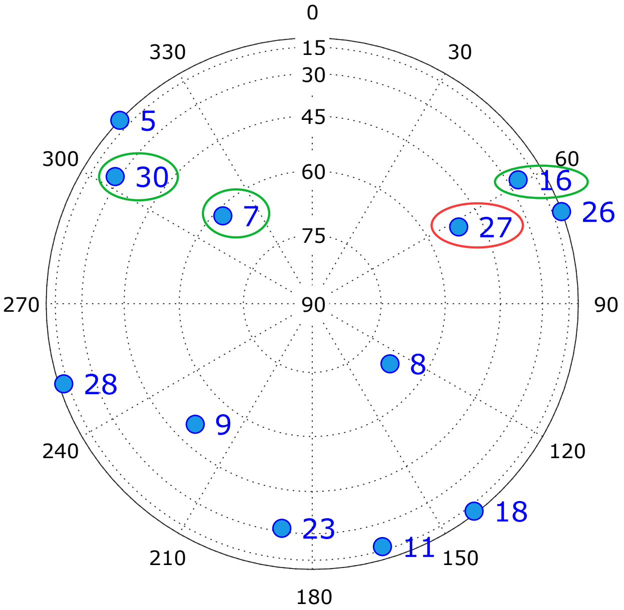

Figure 5.7. Visible satellite list and sky plot at the time of the data analyzed.

Figure 5.7. The skyplot shows satellites that should be visible based on the satellites' elevation and azimuth angles. Zenith is at the center of the plot and the horizon around the perimeter, with azimuth angle of 0° indicating local north and 90° east. Blue points are the satellites (PRNs) present in the sky.

PRN 4 was in the sky but not plotted in Figure 5.7 because it was designated as an unhealthy satellite. All PRNs listed in the table on the left part of Figure 5.7 are, in principle, acquirable in the directly received data (from the upward-facing antenna). In Figure 5.7, four PRNs are circled (PRN 07, 16, 27, and 30) because these PRNs' specular points (reflection point from the surface, see [47] [52]) are on the ice surface due to the sensor suite orientation. These will be the subject of analysis in the reflected data Comparisons 4 and 5.

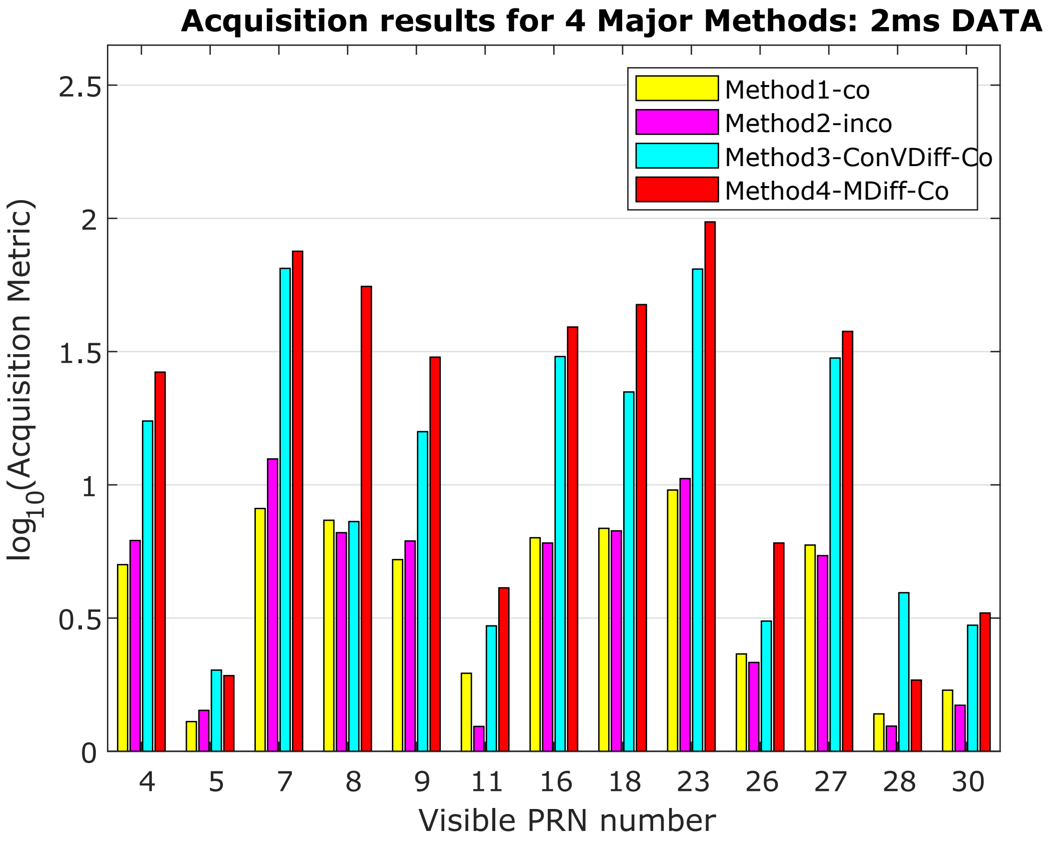

Figure 5.8. Comparison 1 result: acquisition metric for methods 1-4 using $T_1 = T_2 =$ 2 ms of direct signal data.

5.5 Results

5.5.1 Comparison 1. Figure 5.8 shows a bar chart of the acquisition metric $l_{\hat{f}_D}$ for the visible satellites for test 1, comparing Methods 1-4 for $T_1 = T_2 = 2$ ms. The horizontal axis lists the PRNs in the sky and the vertical axis is the base 10 logarithm of the acquisition metric $l_{\hat{f}_D}$. Yellow bars show $l_{\hat{f}_D}$ for method 1, magenta for method 2, cyan for method 3, and red the proposed “modified differential” method (4). The acquisition thresholds (not shown) are $th = 2.5$ for methods 1-2 and $th = 4.5$ for methods 3-4. When the acquisition metric $l_{\hat{f}_D}$ exceeds the threshold, then the satellite is considered acquired (the H_1 hypothesis in Section 2.5). PRN 4 is acquired in all methods, but the satellite is flagged unhealthy in the almanac information. It will be counted as a correct detection in the subsequent analyses. As seen from Figure 5.8, both methods 3 and 4 significantly increase the acquisition metric, with method 4 generally producing a higher ratio than method 3. This trend occurs for all PRNs except PRNs 05 and 28. These satellites are so low on the horizon (see Figure 5.7) that they are not actually acquired by any of the methods. Based on this test we find that, for a satellite acquired by all four methods, the proposed modified differential integration (method 4) will have the highest acquisition metric.

5.5.2 Comparison 2. Figure 5.9 illustrates the logarithmic acquisition metric results (bar plots) of Methods 1-4 for Comparison 2, having $T_1 = T_2 = 10$ ms. Yellow bars show $l_{\hat{f}_D}$ for method 1, magenta for method 2, cyan for method 3, and red for method 4. Method 4 has significantly higher $l_{\hat{f}_D}$ than the other methods, except for PRNs 05, 11, and 28, in which method 4 has lower acquisition metric than method 3. However, for these three PRNs $l_{\hat{f}_D}$ is so low for each method that none of the methods acquire them. For the PRNs that are acquired, method 4 increases the acquisition metric in nearly all cases, a result consistent with the 2 ms results shown in Figure 5.8. As with Comparison 1, Comparison 2 indicates that, given a satellite detected by all four methods, modified differential integration will yield the highest acquisition metric.

5.5.3 Comparison 3. In Comparison 3, Methods 1 and 4 are examined for $T_{coh} = 1$ ms. Figure 5.10 compares the resulting acquisition metrics for method 1 (green) and method 4 (blue). The horizontal axis lists the visible PRNs and the vertical axis is $\log_{10}(l_{\hat{f}_D})$. The blue bars are higher, which means that for the minimum time interval of data (one code repetition), method 4 increases the acquisition metric, suppressing the noise level and increasing the signal power. This is expected, as the method output is almost the square of the power.

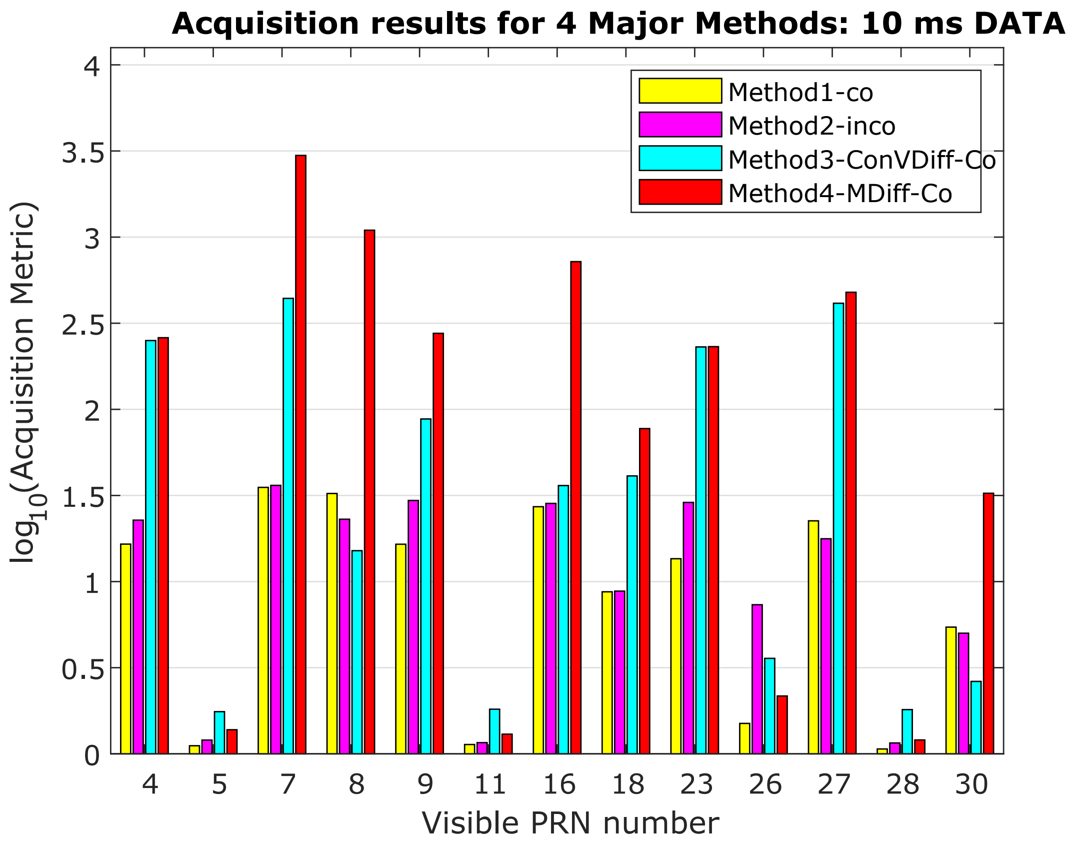

Figure 5.9. Comparison 2 result: acquisition metric for methods 1-4 using $T_1 = T_2 =$ 10 ms of direct signal data.

Table 5.2 summarizes the performance of the methods in Comparisons 1-3 in terms of the number of correctly acquired satellites out of the 12 in the sky, false alarms, and missed detections. For Comparison 1, in which $T_1 = T_2 = 2$ ms, method 4 acquires 9 satellites while the other methods detect only 8 satellites. The additional satellite acquired by method 4 is PRN 26, which is at low elevation at an azimuth of about 70 degrees. There are no false alarms resulting for any of the methods. For Comparison 2, in which $T_1 = T_2 = 10$ ms, Method 2 acquires the greatest number of satellites (10), in contrast to the 9 acquired by methods 1 and 4. This indicates that for longer data segments, conventional methods suffice for acquisition with direct GPS signals, which is why the conventional coherent and incoherent detection are so

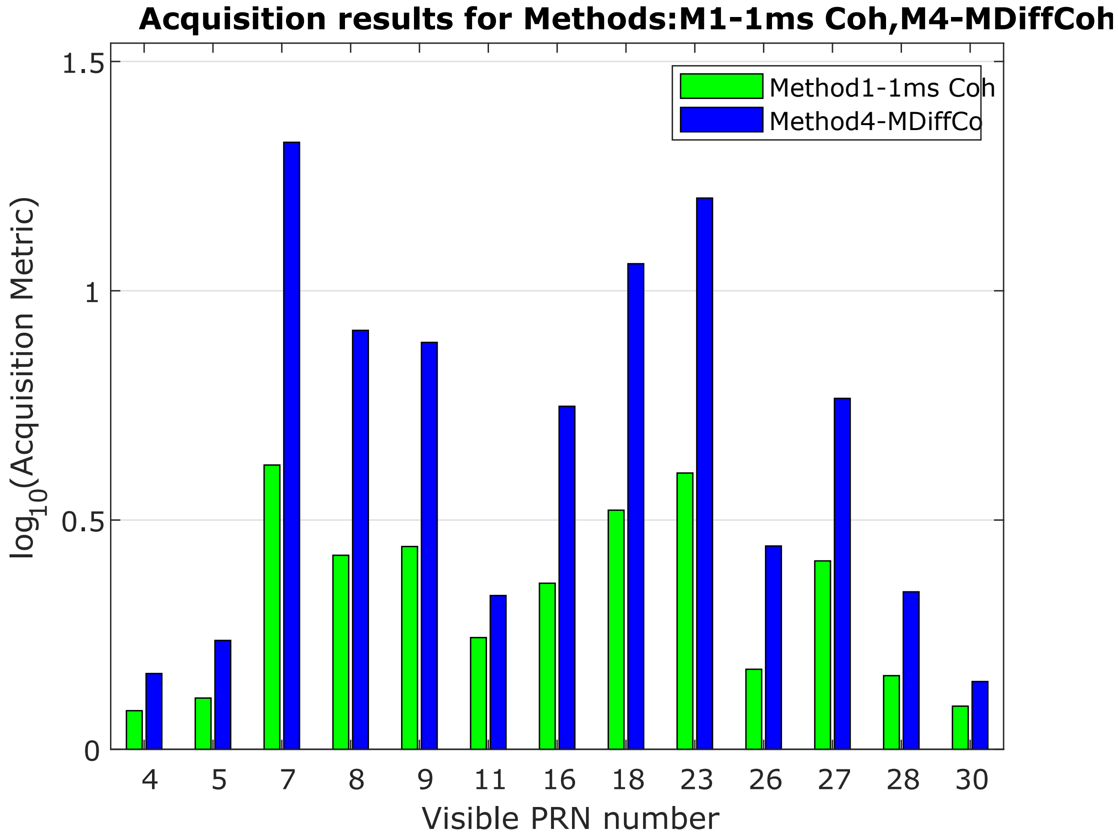

Figure 5.10. Test 3 result: acquisition metric for methods 1 and 4 using $T_d = T_1 =$ 1 ms of direct signal data.

commonly used for navigation. Finally, the Comparison 3 results for methods 1 and 4, using $T_{coh} = 1$ ms, show that method 1 acquires 6 satellites while method 4 detects 7 satellites. In summary, using direct GPS signals, modified differential coherent integration is able to acquire one more satellite (in Comparisons 1 and 3) than the other methods by returning a higher acquisition metric. For longer integration times (i.e., Comparison 2), it may not acquire the most satellites (which method 2 did in this case).

5.5.4 Comparisons 4 and 5. The modified differential integration may not appear useful from Comparisons 1-3, since other methods are sufficient for acquiring enough satellites for navigation. However, since the signal power level yielded by Method 4 is generally higher than that of the other methods, as I show next, it is beneficial for use with reflected GPS signals. All 4 methods' results for Comparisons 4 and 5, which use the reflected GPS signals, are summarized in Table 5.3.

Comparison 4 shows that no method acquires any satellites with a data segment of only $T_i = 2$ ms. Comparison 5 shows that **only method 4** with $T_i = 10$ ms coherent integration is able to detect any satellites from the GPS reflected signal. As identified from comparisons 1-3 with the direct GPS signals, method 4 considerably increases the signal power level. In the case of the reflected GPS signals, method 4 enables acquisition. Figure 5.11 shows the acquisition metric for method 4 using $T_d = 20$ ms of the reflected GPS signal. Green bars indicate the acquired satellites for which $l_{\hat{f}_D} > th$, and blue bars are for the satellites whose acquisition metric $l_{\hat{f}_D} < th$ results in the null hypothesis H_0. Method 4 acquires 3 satellites from the signal reflected from the surface lake ice: PRNs 07, 16 and 30.

From the skyplot (Fig. 5.7) we know that PRNs 07, 16, and 30 (circled in green) are in the northern part of sky during the data campaign, which is in the direction of surface ice coverage (see photo in Figure 4.10). Interestingly, PRN 27, circled in red in the skyplot, is at a similar azimuth angle to PRN 16 and at a high elevation of about 50 degrees, but is not detected. To investigate this further, the auto-correlation functions for PRNs 16, 27, and 07 are plotted for comparison. Figure 5.12 is the auto-correlation power obtained via method 4 (i.e., $\hat{S} = S_{MDI}$) for PRN 16 at the estimated Doppler frequency $\hat{f}_D$. The vertical axis is the modified correlation power (unitless) and the horizontal axis is the C/A code chip delay. A triangle shape with a sharp peak, which is characteristic of the GPS signal auto-correlation (C/A code correlation), appears in this Figure. The ratio of the primary to secondary peaks is greater than a factor of 4.5, which is why PRN 16 is determined to be in the sky.

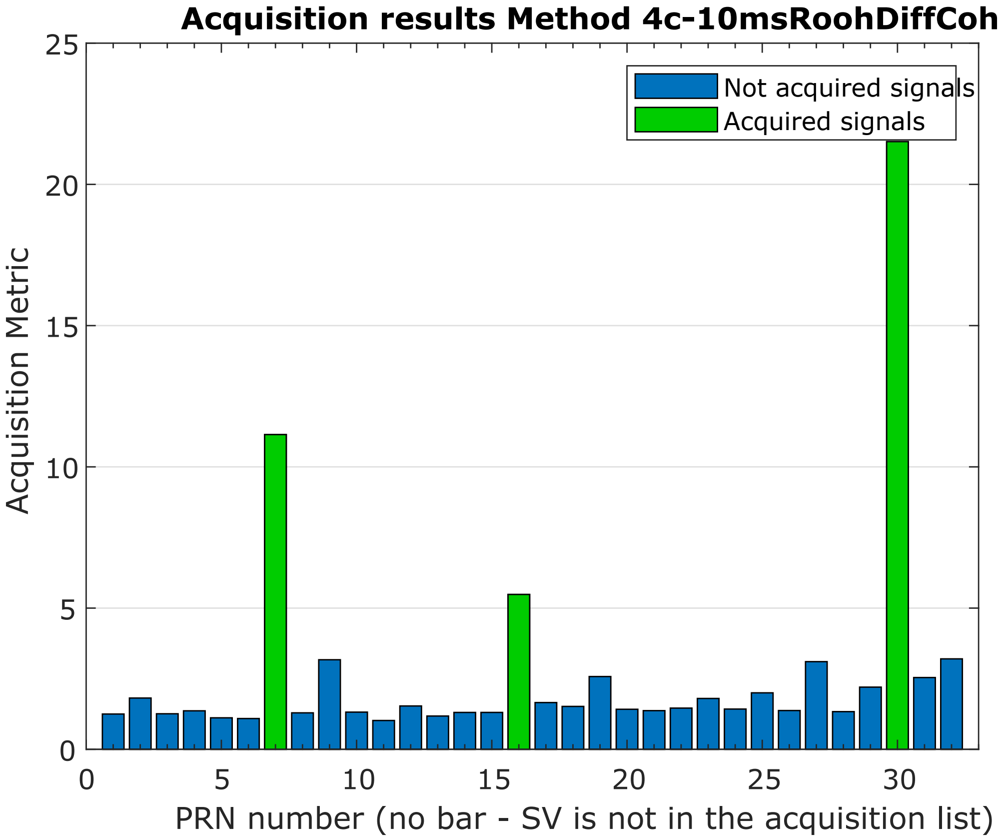

Figure 5.11. Test 5 result: acquisition metric for methods 4 using $T_1 = T_2 = 10$ ms of reflected signal data.

Figure 5.13 shows the auto-correlation for PRN 27 for the reflected GPS signal. For PRN 27, a secondary peak is identified with a red arrow about 120 C/A code chip samples away from the primary peak (since each chip contains 10 samples, this is equal to 12 C/A code chips). For this reason PRN 27 is determined to be invisible, since its acquisition metric $l_{\hat{f}_D} < th$ is less than the method 4 threshold of $th = 4.5$. The secondary peak might be due to multiple scatter due to the surface shape, as discussed in the companion paper [46].

The auto-correlation function for PRN 7, which is also acquired, is shown in Figure 5.14. While PRN 7 has a comparable elevation angle to PRN 27, due to their

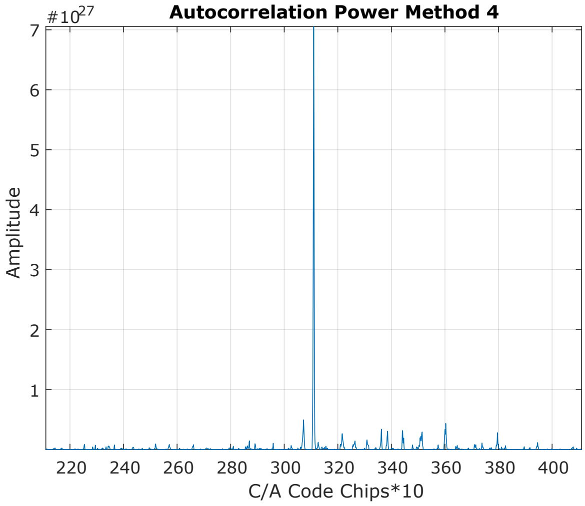

Figure 5.12. Auto-correlation of PRN 16 for the reflected signal.

differing azimuth angles, the signals from the scattering surface arrive at different "antenna zenith" angles, of about 30° degrees and 50°, respectively. Because it is in a similar direction to PRN 27, PRN 16 also has an antenna zenith angle of about 50°.

Given that modified differential integration approximately squares the power, the dB difference between PRNs 07 and 16 is close to 3 dB, but is about 5 dB between PRNs 07 and 27:

$$10\log_{10}\left(\frac{P_7}{P_{16}}\right) = 10\log_{10}\left(\frac{\sqrt{2\cdot 10^{28}}}{\sqrt{7\cdot 10^{27}}}\right) = 2.3\text{dB} \tag{5.17}$$

$$10\log_{10}\left(\frac{P_7}{P_{27}}\right) = 10\log_{10}\left(\frac{\sqrt{2\cdot 10^{28}}}{\sqrt{2\cdot 10^{27}}}\right) = 5\text{dB} \tag{5.18}$$

It is possible that, given the elevation angle of the reflection antenna $\kappa = -45°$, some of the direct signal energy is entering the antenna. If that is the case, then the power accumulated for PRN 16 represents a sum of both the straight-line and multipath signals, which might partly explain why the ratio is only 2.3 dB. PRN 27 is likelier to contain only reflected signal power since it is above 45 degrees elevation. However, given the secondary peak and the possibility of multiple scattering due

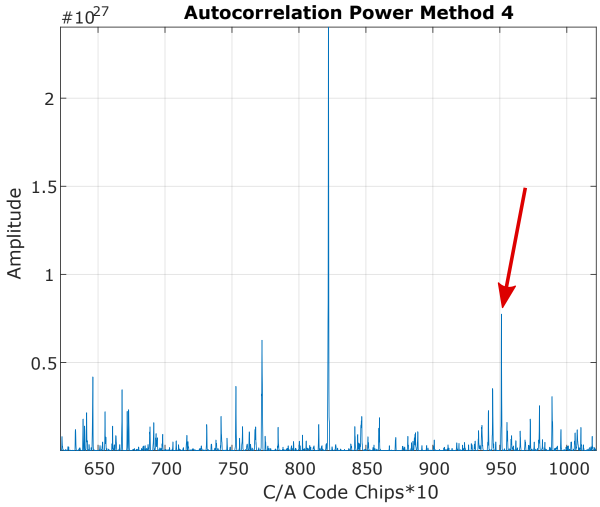

Figure 5.13. Auto-correlation of PRN 27 for the reflected signal.

to the surface geometry, in this case it is likely that not all the power has forward scattered toward the antenna. PRN 07 is at a comparable elevation angle to PRN 27 and so comparably likely to contain only reflected signal power. In this case PRN 07 is one of the satellites acquired. From this result, we conclude that method 4 is capable of acquiring signals scattered from the lake ice surface.

5.6 Conclusion

A new signal acquisition method (modified differential integration) was introduced in this chapter. A form of this method that uses the in-phase signal only (method 4) was compared to 3 other methods: coherent integration (method 1), incoherent detection (method 2), and differential coherent integration (method 3). GPS direct signals and reflected signal collected during a data campaign at Lake Michigan shore with reflections from surface lake ice were used to test these methods. All 4 methods were compared based on the signal acquisition metric ($l^q_{\hat{f}_D}$) and number of detected satellites. In this study $T_i = 2$ ms and $T_i = 10$ ms were used for all methods on the direct signal. Also methods 1 and 4 are examined with $T_i = 1$ ms coherent integration of the direct signal.

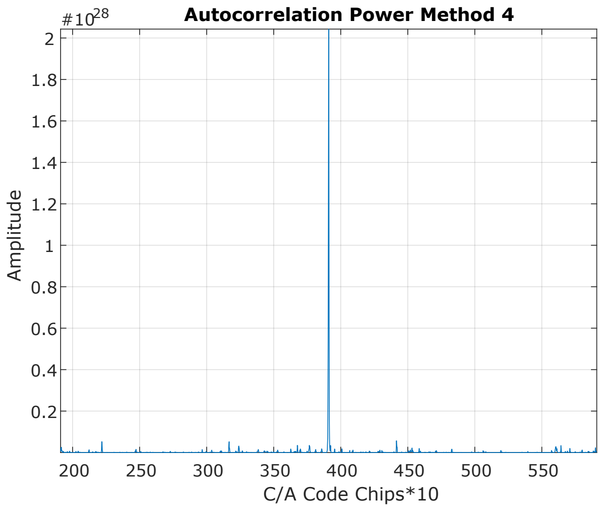

Figure 5.14. Auto-correlation of PRN 07 for the reflected signal.

For $T_i = 1$ ms, method 4 detects 1 more satellite than method 1. Using 2 ms, method 4 acquires 9 satellites rather than the 8 acquired by the other methods. Only with the $T_i = 10$ ms, is method 2 able to acquire one more satellite than method 4. However, the acquisition metric is higher for method 4 than the other methods among satellites acquired. In addition, these methods are examined with the reflected GPS signals from the lake surface. Only method 4, with $T_1 = T_2 = 10$ ms coherently integrated, is able to acquire satellites from the reflected GPS signals. Three PRNs (07, 16, and 30) are detected in the reflected signals. PRN 27 at a similar azimuth to the detected PRN 16, but at higher elevation angle, is not detected. This is due to a secondary peak that causes the acquisition metric to be lower than the method 4 threshold. One possible explanation for the acquisition of PRN 16 but missed detection of PRN 27 is due to the antenna reception of additional power from the line-of-sight satellite-to-receiver signal. Since at least PRN 07 is acquired, we conclude that our proposed modified differential coherent integration method yields enough power to enable acquisition of satellites whose signal is reflected from the lake ice surface. Variations of the modified differential integration will be studied in the future, particularly those leveraging the quadrature-phase samples. The complex form of this acquisition method in Eq. (5.2) may be used for GNSS reflectometry investigations. More generally, for applications aiming to acquire satellites from GPS reflection signals, we suggest that the modified differential incoherent integration is a promising way forward.

Table 5.2. Results of Comparisons 1-3 using the direct GPS signal.

Comparison	1			
$T_i, i = 1, 2$	2 ms			
Method	1	2	3	4
Acquisition threshold th	2.5	2.5	4.5	4.5
Correct detection rate	8/12	8/12	8/12	9/12
False alarm	0	0	0	0
Missed detection rate	4/12	4/12	4/12	3/12
Detected PRNs	4,7,8,9,16 18,23,27	4,7,8,9,16, 18,23,27	4,7,8,9,16, 18,23,27	4,7,8,9,16, 18,23,26,27
Comparison	2			
$T_i, i = 1, 2$	10 ms			
Method	1	2	3	4
Acquisition threshold th	2.5	2.5	4.5	4.5
Correct detection rate	9/12	10/12	8/12	9/12
False alarm	0	0	0	0
Missed detection rate	3/12	2/12	4/12	3/12
Detected PRNs	4,7,8,9,16 18,23,27,30	4,7,8,9,16, 18,23,26,27,30	4,7,8,9,16, 18,23,27	4,7,8,9,16, 18,23,26,27,30
Comparison	3			
$T_i, i = 1, 2$	1 ms			
Method	1		4	
Acquisition threshold th	2.5		4.5	
Correct detection rate	6/12		7/12	
False alarm	0		0	
Missed detection rate	6/12		5/12	
Detected PRNs	7,8,9,18,23,27		7,8,9,16,18,23,27	

Table 5.3. Results of Comparisons 4-5 using the reflected GPS signal.

Comparison	4			
$T_i, i = 1, 2$	2 ms			
Method	1	2	3	4
Acquisition threshold th	2.5	2.5	4.5	4.5
Correct detection rate	0	0	0	0
False alarm	0	0	0	0
Missed detection rate	12/12	12/12	12/12	12/12
Detected PRNs	-	-	-	-
Test	5			
$T_i, i = 1, 2$	10 ms			
Method	1	2	3	4
Acquisition threshold th	2.5	2.5	4.5	4.5
Correct detection rate	0	0	0	3/12
False alarm	0	0	0	0
Missed detection rate	12/12	12/12	12/12	9/12
Detected PRNs	-	-	-	7,16,30

CHAPTER 6

EVALUATION OF GNSS-R USING AUXILIARY SENSORS

6.1 Overview

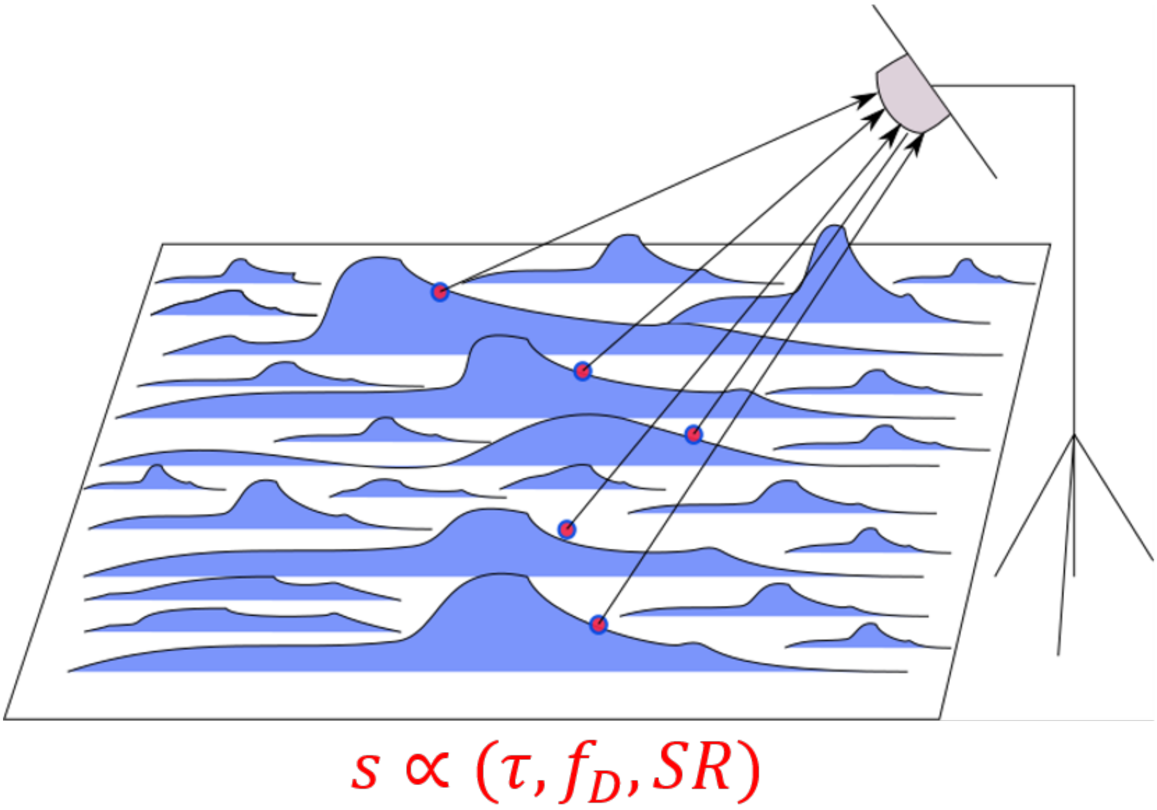

Figure 6.1. Cartoon of a surface with SPs (red) from satellites 1 to n scattering power toward the reflected antenna.

The GNSS signal is dominated by specular reflection, and the strongest reflection comes from the specular point (SP), as shown in the cartoon in Figure 6.1. GNSS signals from a given satellite reflected from a surface will travel along different paths toward the downward-looking antenna and so have different delays (τ). If there is surface motion the signals may have different Doppler shifts (f_D). The fraction of incident power that is reflected by a surface is called surface reflectivity SR. SR depends on the surface condition and affects the signal-to-noise ratio SNR. Therefore, the signal power received at the reflected antenna for a given satellite is a function of delay, Doppler frequency, and SR which is proportional to SNR (Figure 6.1).

$$S_{scattered} \approx f(\tau, f_D, SR) + w \tag{6.1}$$

In this chapter, we compute the delay Doppler map (DDM), SNR and SR for PRNs in the reflected signal, and we relate them to the surface condition from which the GNSS signals are reflected. Auxiliary sensor data are used to map the surface condition. Estimating the SPs of the visible satellites on the map lets us visually verify the surface condition at the point from which most of the energy has scattered. Data from Data Campaign 8 (Location B) and Data Campaign 11 are used in this chapter. The surface condition for Data Campaign 8 was snow-covered ice, and for Data Campaign 11 the surface condition was a heterogeneous mix of ice and water. The sensor system schematics are shown in Figure 4.10 for Data Campaign 8 (Location B), and Figure 4.14 for Data Campaign 11. The system configurations are summarized in Table 4.8 and 4.11, respectively. This chapter has three sections. Section 6.2 describes the method for identification of surface type, selection of PRN, and GNSS-R quantities to be computed. Section 6.3 uses Data Campaign 8 (Location B) data to demonstrate how the surface type is determined and compute the DDM and SNR for a satellite scattering off that surface (ice). Section 6.4 shows results of Data Campaign 11 to compute the SNR and SR for two PRNs whose SPs scan across water and ice over time.

6.2 Method for comparison of GNSS-R power to surface type

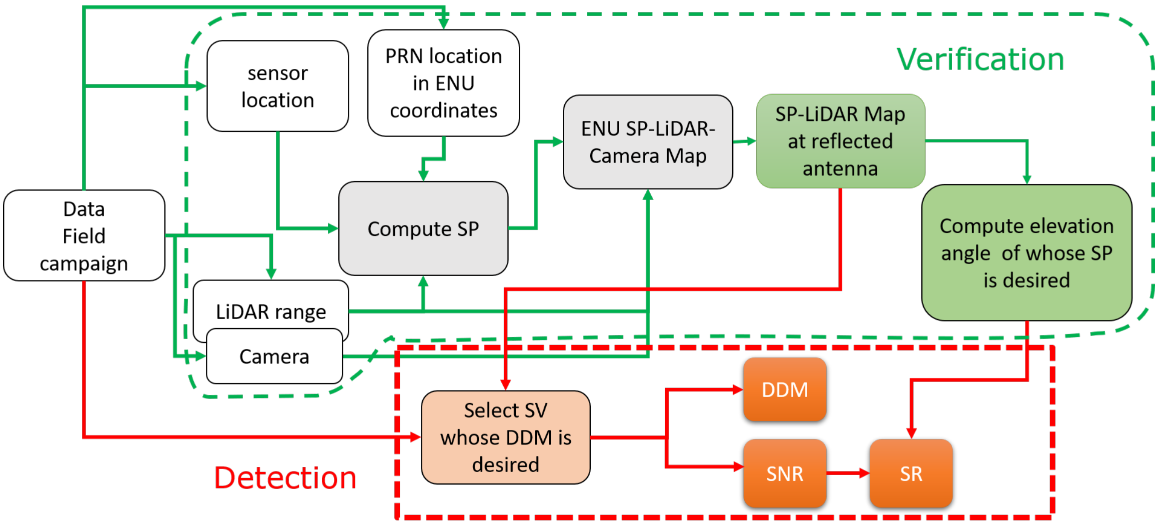

Figure 6.2. Flowchart describing the process by which the surface type for a reflecting satellite is verified and the satellite selected for analysis, followed by computation of the GNSS reflected signals' characteristics for the selected satellite (SV).

In order to relate the signal power received to the surface type, we must estimate the specular reflection point and correlate it with independent measurements of the surface type at that site. Figure 6.2 describes the surface verification and reflected signal power DDM, SNR, and SR computation process. To determine the surface condition at the point at which a GNSS signal is reflected, an SP-lidar-camera map is generated. This map illustrates the SPs' positions in an ENU coordinate system, overlaid with lidar and camera data to indicate the surface condition at those positions. To generate the SP-lidar-camera map, the sensor position is estimated from the direct GPS signal, and the visible satellites' locations in the ENU coordinate system are estimated using a Yuma almanac. Given the lidar range data surface height d from Eq.(C.7) and satellite positions, the SPs are computed. Next, using the lidar and camera data as described in [33], the ENU SP-lidar-camera map is created. From this map, a satellites whose SP can be confirmed visually to be on a specific surface type is selected. The DDM is computed using Eq. (5.15) as described in Chapter 5. To compute the signal-to-noise ratio (SNR) in this work, Eq. 6.2 is used.

$$SNR = \frac{P_{max} - P_{noise}}{P_{noise}} \tag{6.2}$$

In this equation, P_{max} is the maximum of auto-correlation power and P_{noise} is mean value of the noise. To find these values, the scattered power after pre-conditioning (see Chapter 2) is correlated with replica of the code of the selected PRN for the traditional auto-correlation power (square of the auto-correlation, see Chapter 2). The peak of the auto-correlation is P_{max}. To compute P_{noise}, the mean value of the auto-correlation function excluding points within $\pm 1\, T_{C/A}$ ($T_{C/A}$ length of a PRN code chip) is taken. One of the surface characteristics of interest from the reflected GNSS signals is surface reflectivity, which is the ratio between the incident signal power to the reflected signal power from a surface. The SR is computed using Eq.(2.26), repeated here for convenience:

$$\begin{aligned} SR \;\propto\; & SNR - 10\log(P_r^t) - 10\log(G^t) - 10\log(G^r) - 20\log(\lambda) \\ & +20\log(R_{ts} + R_{sr}) + 20\log(4\pi) \end{aligned} \tag{6.3}$$

where SNR is the signal-to-noise ratio computed previously, $P_r^t = 17.4$ dB is the transmitted right hand circular polarization power (RHCP), G^t is the gain of the transmitting antenna, $\lambda = 0.19$ m is the GPS L1 carrier wavelength , $G^r = f(\phi)$ is the gain of the reflected antenna (a function of the antenna gain pattern [16]), R_{ts} is the distance form the transmitter to the SP and finally, R_{sr} is the distance from the SP to the reflected antenna.

Note the quantity in dB in Eq. (6.3), which we refer to as SR, is actually proportional to the fractional surface reflectivity. All quantities are known or estimated from the geometry. To compute a quantity proportional to the SR, the reflected antenna zenith angle ϕ of the line-of-sight to the SP must be computed in order to account for the receiving antenna gain (see Section 2.6.4). The antenna zenith angle calculation is discussed in detail in Appendix B.

6.3 Data Campaign 8 (Location B) ice analysis

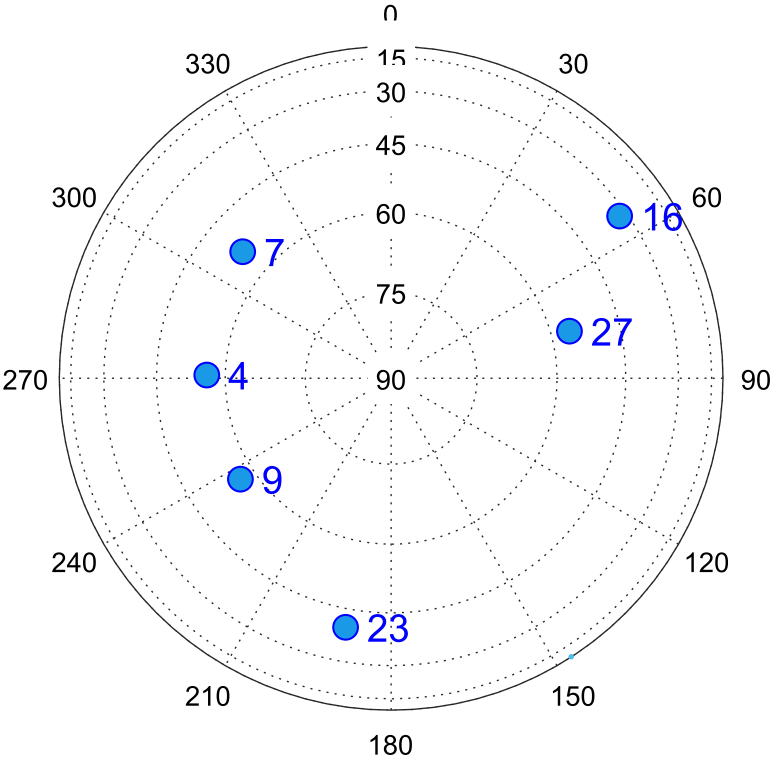

Figure 6.3. Sky plot for Data Campaign 8 (Location B).

Figure 6.3 is a sky plot of the satellites visible during Data Campaign 8 (Location B). In this plot, azimuth angles are measured clockwise from north. Elevation 90 degrees in the center of the skyplot indicates the zenith of direct antenna. Blue circles are satellites acquired in the direct antenna data using the baseline SDR (the MDI detection technique described in Chapter 5 is not used). Six PRNs are acquired for positioning.

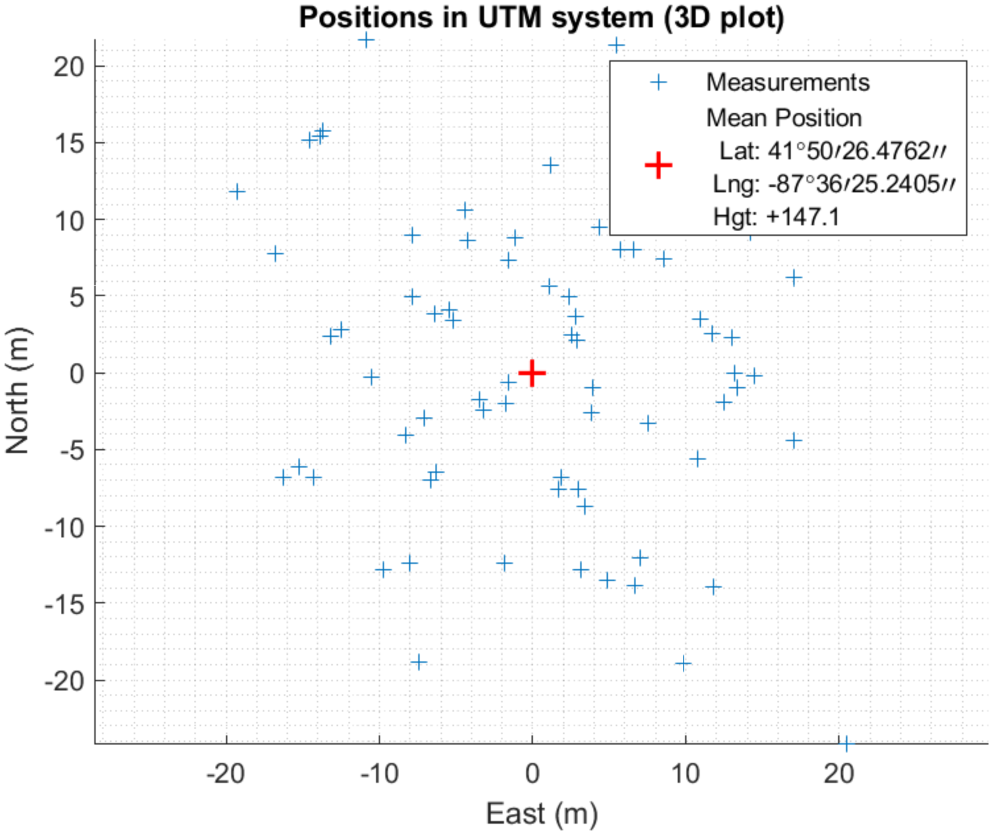

Figure 6.4. Scatter plot of sensor position estimated with GPS L1 direct antenna data for Data Campaign 8 (Location B) relative to average position (red).

The navigation solution for Data Campaign 8 based on the SDR is shown in Figure 6.4. The vertical and horizontal axes indicate meters north and east, respectively, of the direct antenna. The red cross is the average sensor position ($\bar{\hat{x}}$) over approximately $N = 64$ position estimates made by the SDR (each blue cross is a estimation of the sensor location $\hat{x}_n$).

$$\bar{\hat{x}} = \frac{1}{N}\sum_{n=1}^{N}\hat{x}_n$$

From this estimation, the WGS-84 height of the direct antenna is 147.1 m, and coordinates are $(41°50'26.4762"\ \mathrm{N}, 87°36'25.2405"\ \mathrm{W})$ for Data Campaign 8 (Location

B).

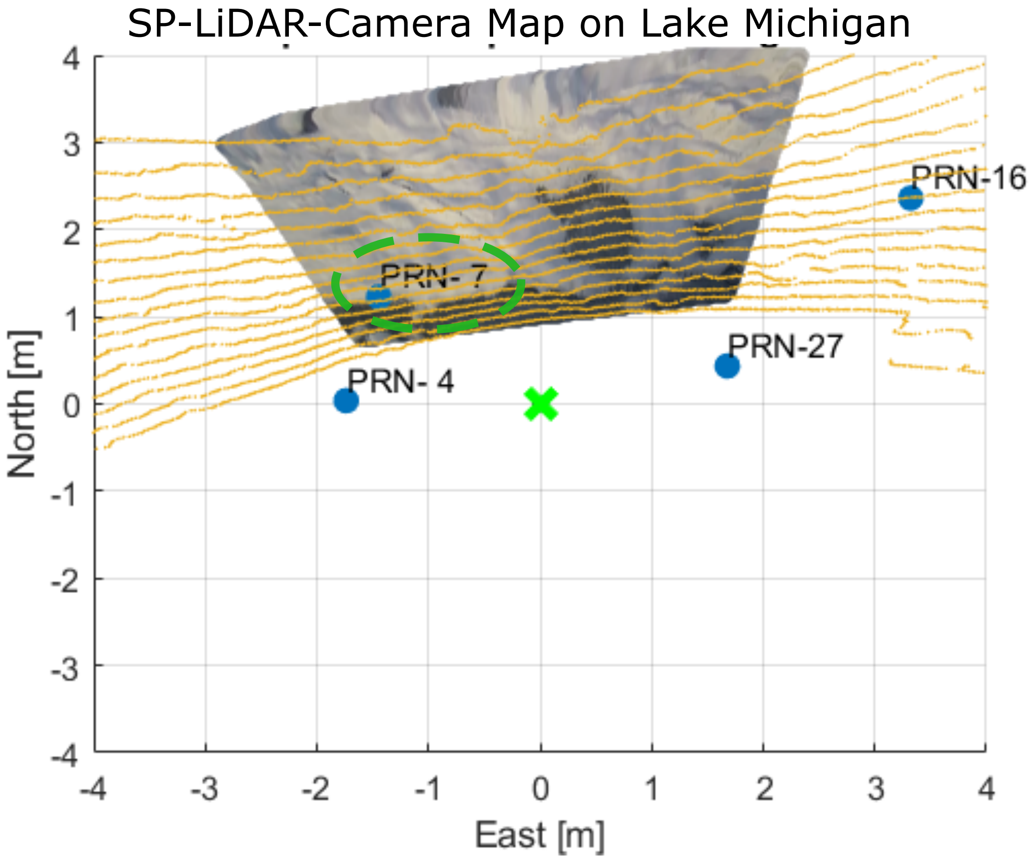

Figure 6.5. SP-lidar-camera map in ENU coordinates with origin at the reflected antenna. The green cross marks the reflected antenna position, SPs are blue circles, lidar point cloud is yellow dots, and camera pixels are projected in the trapezoidal area.

Figure 6.5 illustrates the SP-lidar-camera map for Data Campaign 8 (Location B). Blue circles are the SPs of the visible satellites to the north of the sensor system. The green cross is the center of the reflected antenna. The vertical axis is the north direction and horizontal axis is the east direction. Yellow points are the lidar point cloud and the camera picture transformed to have the origin at the reflected antenna. The lidar point cloud is transformed to the reflected antenna reference frame with rotation and translation (for more details about the lidar point cloud and camera data processing see [33]). Figure 6.5 indicates that PRN 07's SP is on the ice surface. The

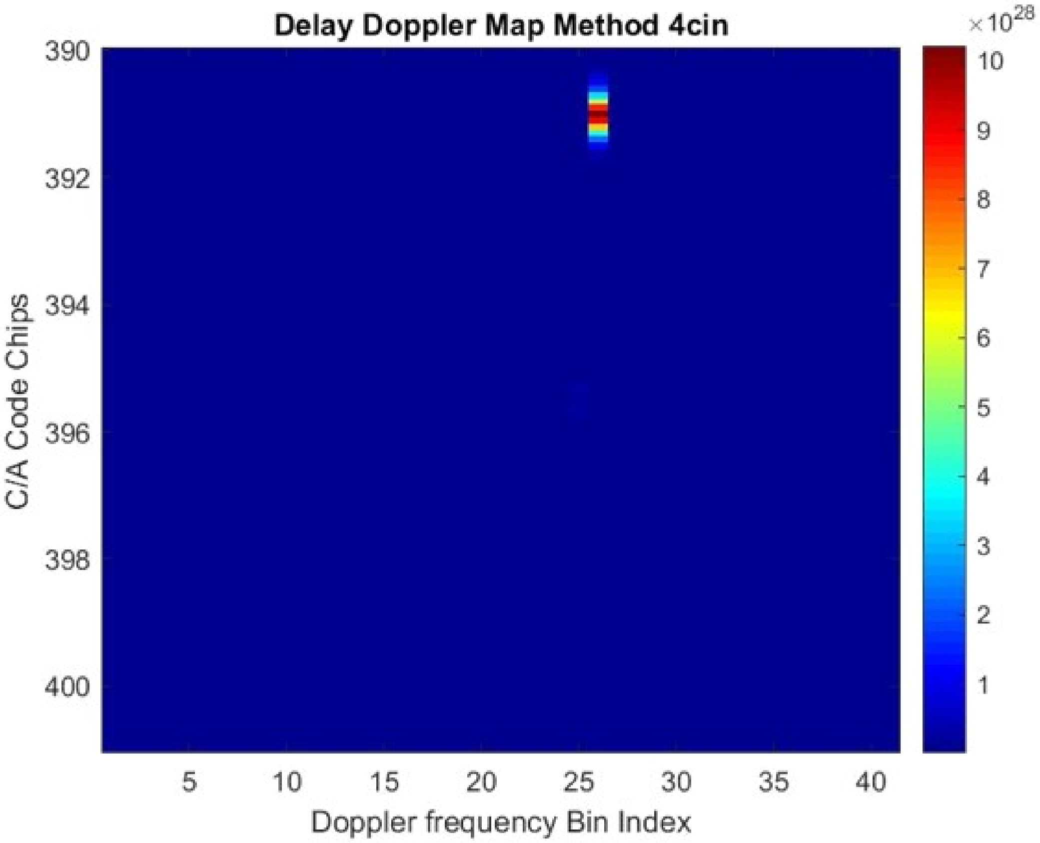

Figure 6.6. Delay Doppler Map of PRN 07 of reflected signals

presence of lidar returns indicates a solid rather than liquid surface, and the camera image shows whiter pixels indicating the ice may be covered with a layer of snow. In contrast, PRNs 04 and 27 are beyond the field of view of the lidar and the camera, so the surface type cannot be verified. PRN 16 is likely reflecting from ice since there are lidar returns, but is beyond the field of view of the camera. Therefore, PRN 07 is selected for GNSS-R analysis.

The Delay Doppler Map of the reflected signal for PRN 07 of Data Campaign 8 (Location B) is shown in Figure 6.6. In this figure, the vertical axis is the time delay (C/A code chips delay) and the horizontal axis is the Doppler frequency bin index (Doppler frequency search index). The color here indicates the square of auto-

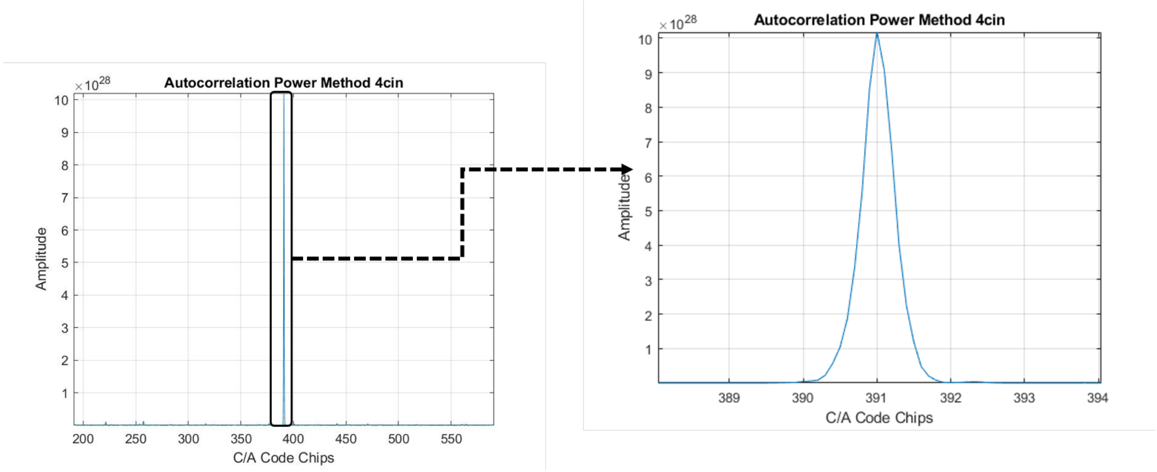

Figure 6.7. MDI Auto-correlation of the PRN 07 of reflected signal (right) 5.

correlation power $\hat{S}(S_{MDI})$ using the Method 4 (Section 5.3.4) $T_{coh} = 1ms$, and incoherent detection $T_1 = T_2 = T_{inc} = 1000ms$ (see chapter 5 for signal processing, Eq.(5.6)). To generate the DDM, the Modified Differential integration method (MDI) is used. As seen from Figure 6.6 a peak appears at $\tau = 391$ C/A code chips delay and $f_D = 26$ Doppler frequency bin index. A strong reflected GNSS signal is detected. Due to our sensor system height above the surface being only about 2 m, we expected a single peak without any spread in C/A code delay.

The auto-correlation of the reflected signal for PRN 07 is presented in Figure 6.7. A zoomed-in view of the auto-correlation peak is shown to the right. Auto-correlation is the slice of the DDM the Doppler frequency bin of peak power. As with the DDM, the C/A code chips delay is $\tau = 391$C/A chips. Also, a clean auto-correlation is achieved with the MDI method.

Figure 6.8 illustrates the SNR of the reflected signal for PRN 07 for 1 second. For a given integration time T_{coh}, T_{inc} (Eq.(2.13) and Eq.(5.6)), multiple estimates of SNR are made over the course of 1 s. In this plot, 2 peaks are greater than 1

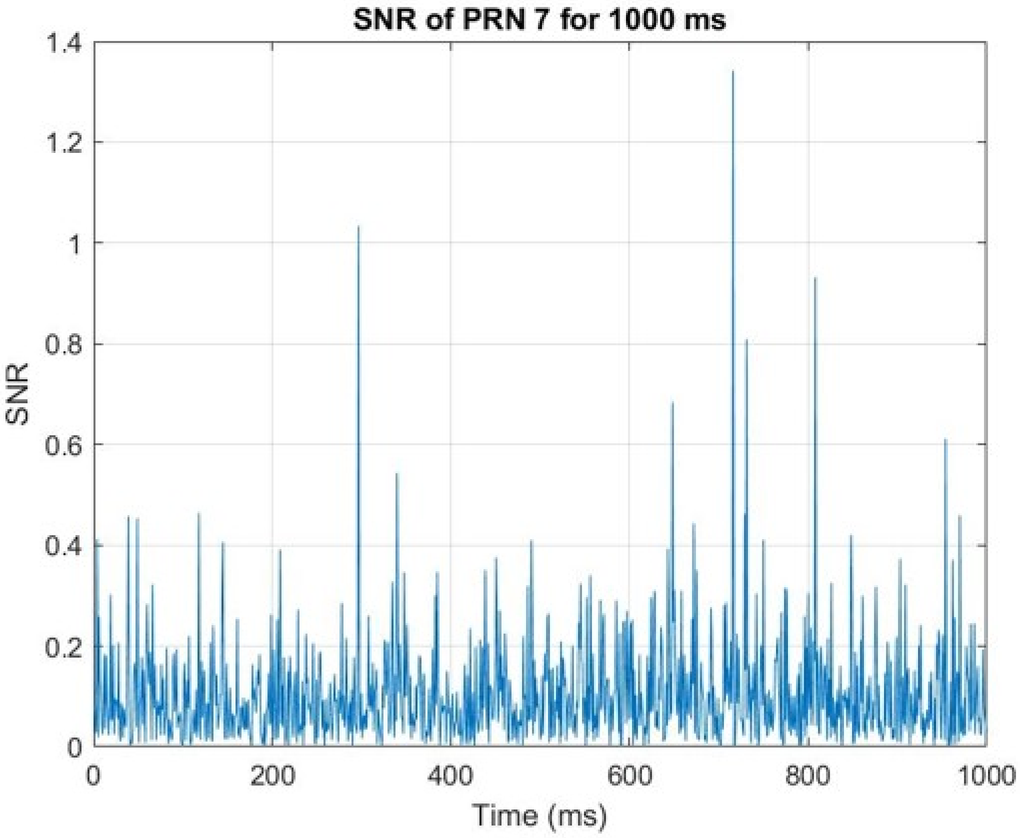

Figure 6.8. Signal-to-noise ratio (SNR) of PRN 07 from Data Campaign 8 (Location B) of reflected signal for 1 second.

(around 300 ms and 750 ms), which means that P_{max} is at least 2 times greater than P_{noise}. Surface reflectivity derived from the PRN 07 SNR is shown in Figure 6.9 for 1 second. Multiple spikes appear in the SR plot which are consistent with the SNR plot of Figure 6.8. The sub-second trend of the SR plot follows that of the SNR. Given that SP does not move over the surface rapidly, the mean value of SR over a minute and its variation over an hour can help us to detect ice versus water. However, to discriminate ice from water, a surface with heterogeneous water conditions is needed. The next section shows results from mixed surface conditions.

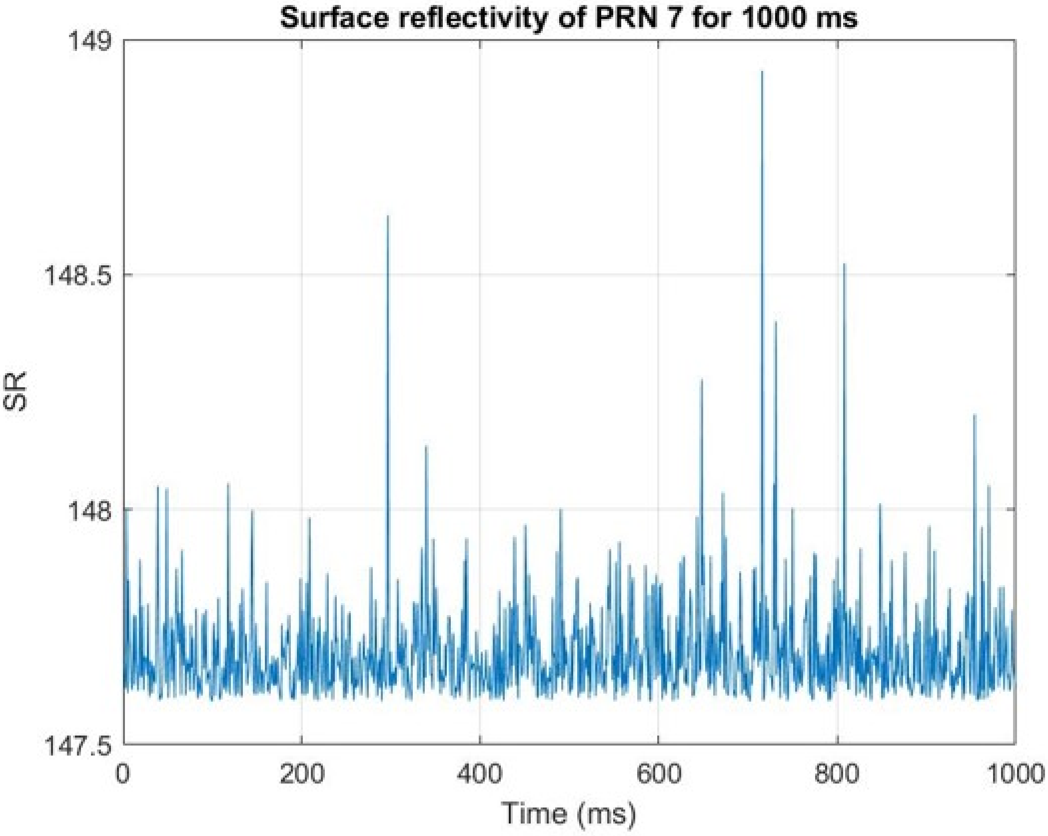

Figure 6.9. Surface reflectivity (SR) of PRN 07 from Data Campaign 8 (Location B) of reflected signal for 1 second.

6.4 Data Campaign 11 mixed ice-and-water analysis

Data Campaign 11 was conducted when the surface was a heterogeneous mix of ice and water. The purpose of this section is to show how the SNR and SR vary over time as a PRN's specular point scans over different parts of the surface. Parts 1, 2 and 3 of the data are used, from time 11:58 to 13:03 CT. While there are three cameras in the system for this campaign, only images from the center camera are shown. The satellites present in the sky at 11:58 CT which is the start of the time interval of the data analyzed are shown in Figure 6.10, based on the Yuma almanac. Visible satellites are indicated with blue circles. With the lake to the east of the sensor

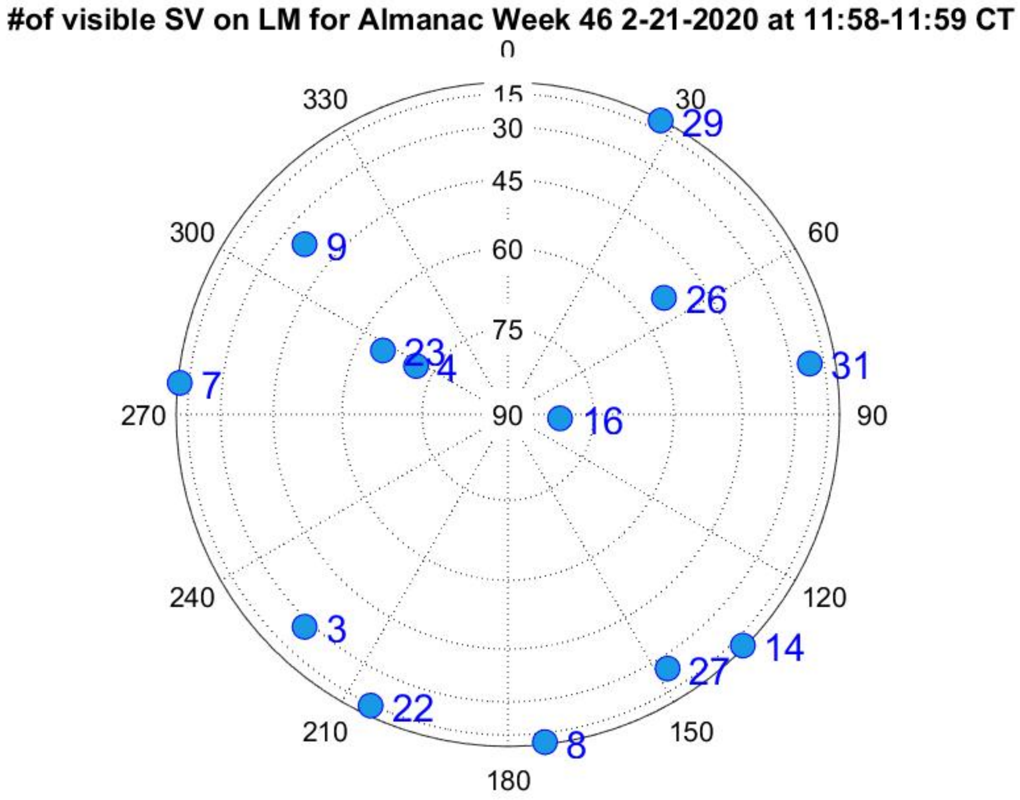

Figure 6.10. Yuma almanac-based sky plot at 11:58 Central Time (CT) for Data Campaign 11.

system (see Figure 4.14), the satellites in the eastern part of the sky are anticipated to produce specular points reflecting from the lake surface. In particular, note that PRN 16 is at high elevation in the sky. PRN 27 is at low elevation but rising in the sky over the duration of this data campaign. PRNS 16 and 27 will be analyzed in the next subsections, respectively.

6.4.1 PRN 16: Water then ice. Since the surface condition was mixed water and ice, the SP-lidar-camera map is generated for the whole 20-minute time interval to see which PRNs scan over both ice and water during the data campaign. Figure 6.11(a) presents the SP-lidar-camera map at the beginning of part 1 of the campaign

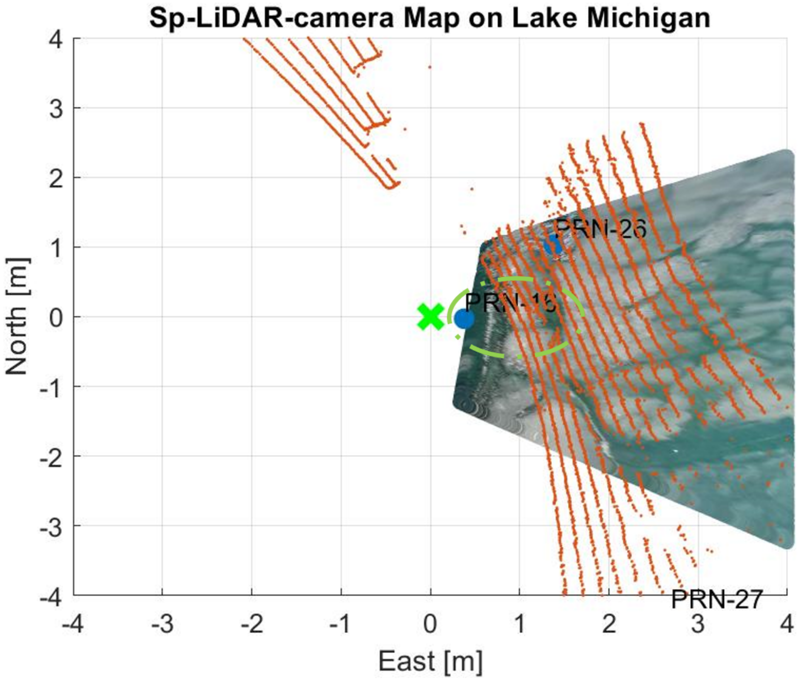

(a) 11:58 CT.

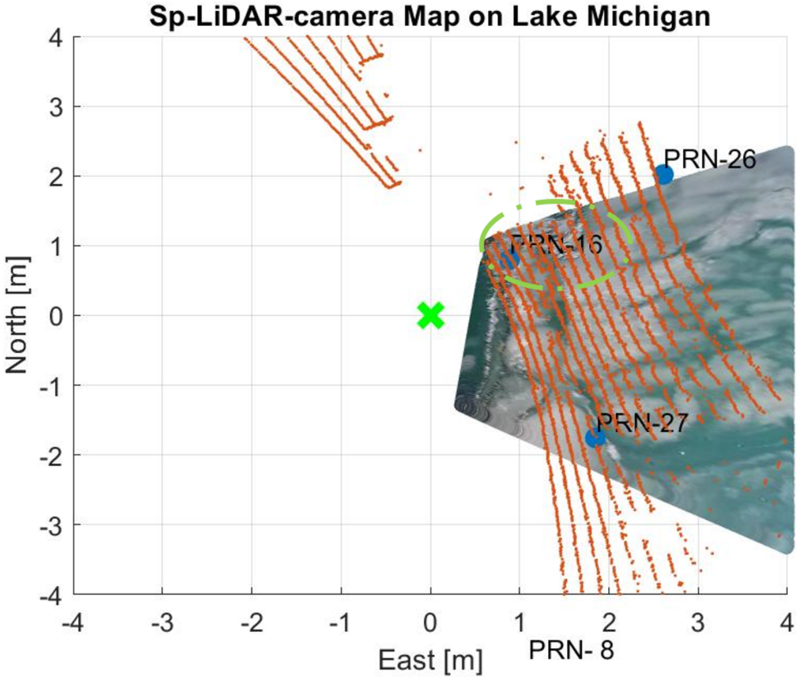

(b) 12:18 CT.

Figure 6.11. SP-lidar-camera maps of Data Campaign 11 at (a) 11:58 CT and (b) 12:18 CT. The Sensor origin is marked with a green cross. The Lidar point cloud is marked with orange dots. The Camera image from the central camera is projected onto the map in color. Specular points are blue labeled by satellite PRN number.

(11:58 CT). This figure shows that the SP of PRN 16, circled with a dashed green line, is on the water. We conclude this based on the camera image, even though the SP is beyond the field-of-view of the lidar scan. Figure 6.11(b) is the SP-lidar-camera map 20 minutes later at 12:18 CT. From this figure the SP of PRN 16 is on the ice, based on both camera image and lidar point cloud. Figure 6.11 shows that the SP of PRN 16 is on the water at the beginning of Data Campaign 11 and gradually moves over the ice.

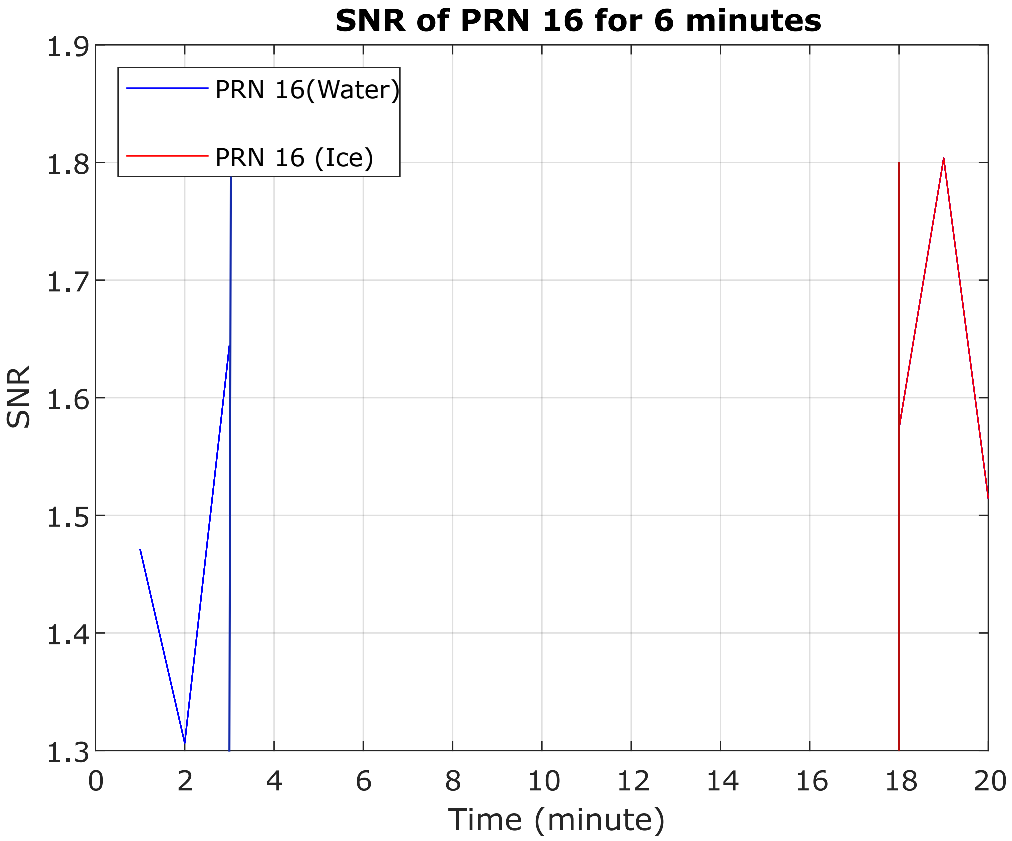

Figure 6.12. Signal-to-noise ratio (SNR) of PRN 16 over time, in minutes since 11:57 CT. Blue indicates times visually identified on the SP-lidar-camera map to correspond to water reflection, and red indicates times corresponding to ice reflection.

The SNR of PRN 16 for Data campaign 11 is plotted over time in Figure 6.12. Since computing SNR is computationally intensive, the SNR is calculated for minutes 1-3 (11:58-12:01 CT) and for minutes 18-20 (12:16-12:18 CT) of the data set. For this calculation, T_{coh} = 1ms coherent integration and T_{incoh} = 1000ms incoherent detection. The SNR is averaged over each minute. The GNSS-R SNR from the freshwater surface is shown with blue, while red in Figure 6.12 indicates an icy surface. From this figure, the SNR from the peak of icy surface is higher on average than from the water surface.

However, the SNR includes the receiving antenna gain pattern. Taking the gain pattern into account, the SR of PRN 16 is shown in Figure 6.13. The red segment corresponds to ice and the blue segment corresponds to water as visually determined by the SP-lidar-camera maps. As shown in Figure 6.13, the average SR over time is lower for water than for ice by about 0.5 dB. From this we conclude that it may be possible to use SR derived from reflected GNSS-R signals to discriminate between surface ice and water.

6.4.2 PRN 27: Ice to water to ice. Figures 6.14 and 6.15 include three SP-lidar-camera maps of Data Campaign 11 at 12:43 CT, 12:54 CT and 13:03 CT. The SP of PRN 27 circled in green is scanning the surface toward the northwest direction. PRN 27 is crossing the surface at a point at which the phase of the water changes. The surface ice is melting along cracks, visible as blue water between the white ice. In Figure 6.14(a) the SP of the PRN 27 on the ice. Figure 6.14(b) is a snapshot of the SP-lidar-camera map when the SP of PRN 27 appears to be on water. We estimate this because there is a gap in the lidar point cloud at the SP that coincides with blue (water) on the camera image, indicating this reflection point is water. The third snapshot in Figure 6.15 shows the SP of PRN 27 as it leaves the mixed and re-enters the surface ice, based on the presence of lidar returns (which only scatter off ice, but not off water). From the Figures we conclude that the SP of PRN 27 is scanning the surface over this time period reflecting off different phases of water.

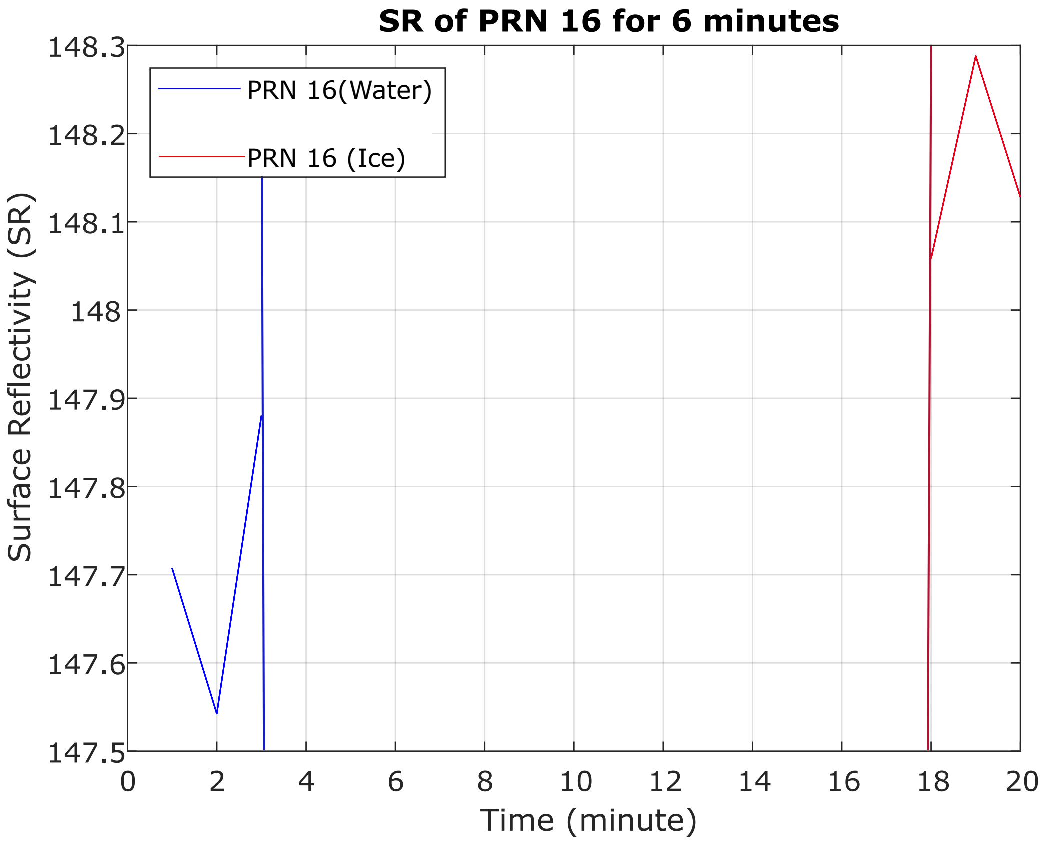

Figure 6.13. Surface reflectivity (SR) of PRN 16 over time, in minutes since 11:57 CT. Blue indicates times visually identified on the SP-lidar-camera map to correspond to water reflection, and red indicates times corresponding to ice reflection.

Figure 6.16 describes the SNR of PRN 27 of Data campaign 11, part 3. The twenty minutes of data from 12:43-13:03 CT are divided into 3 segments (early, middle, and late) corresponding to the times whose maps are shown in Figures 6.14 and 6.15. Segments 1 and 3 were visually determined to be likely ice and are plotted in red. Segment 2 was estimated to be on the water, and is plotted in blue. A rapid rise in the SNR of segment 1 is seen in Figure 6.16. In segment 2 the SNR begins high at nearly 3, drops and begins to recover. In segment 3 the SNR remains high. Figure 6.17 shows the SR over time for PRN 27 during the early, middle, and late segments. Segments 1 and 3 are in red, meaning that the surface condition was visually determined to be ice. Segment 2 is blue, whose surface condition was visually determined to be water. Here there is less clear of a difference in SR values between the ice and water segments. One possible reason is that PRN 27 passes over a water-filled crack in the ice surface whose size is less than 1 m square. Most energy is typically scattered from the first Fresnel zone [6]. Given the height of the reflected antenna above the lake surface, we expect the scattering area to be on the order of 1 m^2, In these three segments, it is possible that the scattered GNSS-R signal includes scatter from a mixture of sub-meter scale water and ice, which are averaged together in the SNR and resulting SR. However, still the maximum and mean value of the red sections are greater than the maximum of the blue section by about 0.3 dB.

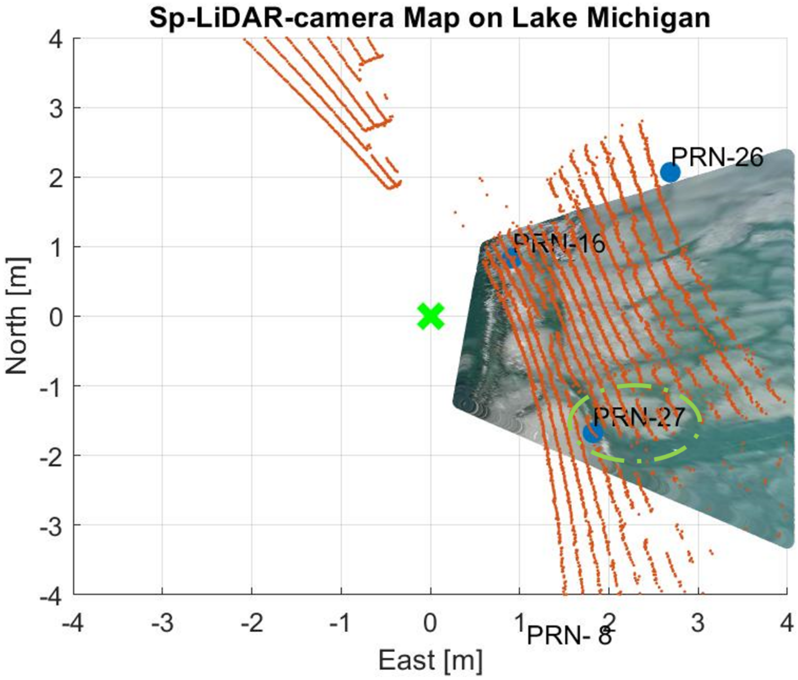

(a) 12:43 CT.

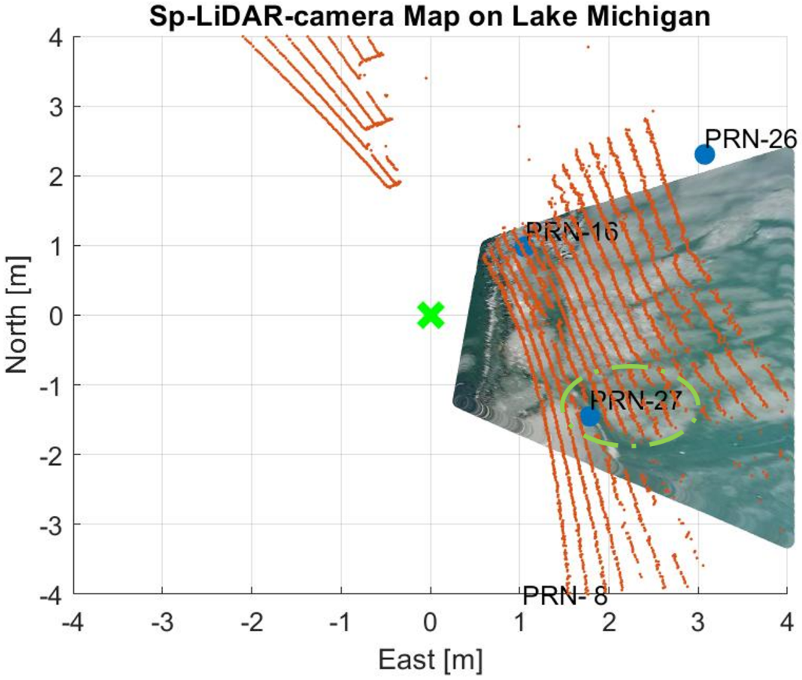

(b) 12:54 CT.

Figure 6.14. SP-lidar-camera maps of Data Campaign 11 at (a) 11:58 CT and (b) 12:18 CT. Sensor origin is marked with a green cross. Lidar point cloud are orange dots. Camera image from the central camera is projected onto the map in color. Specular points are blue labeled by satellite PRN number.

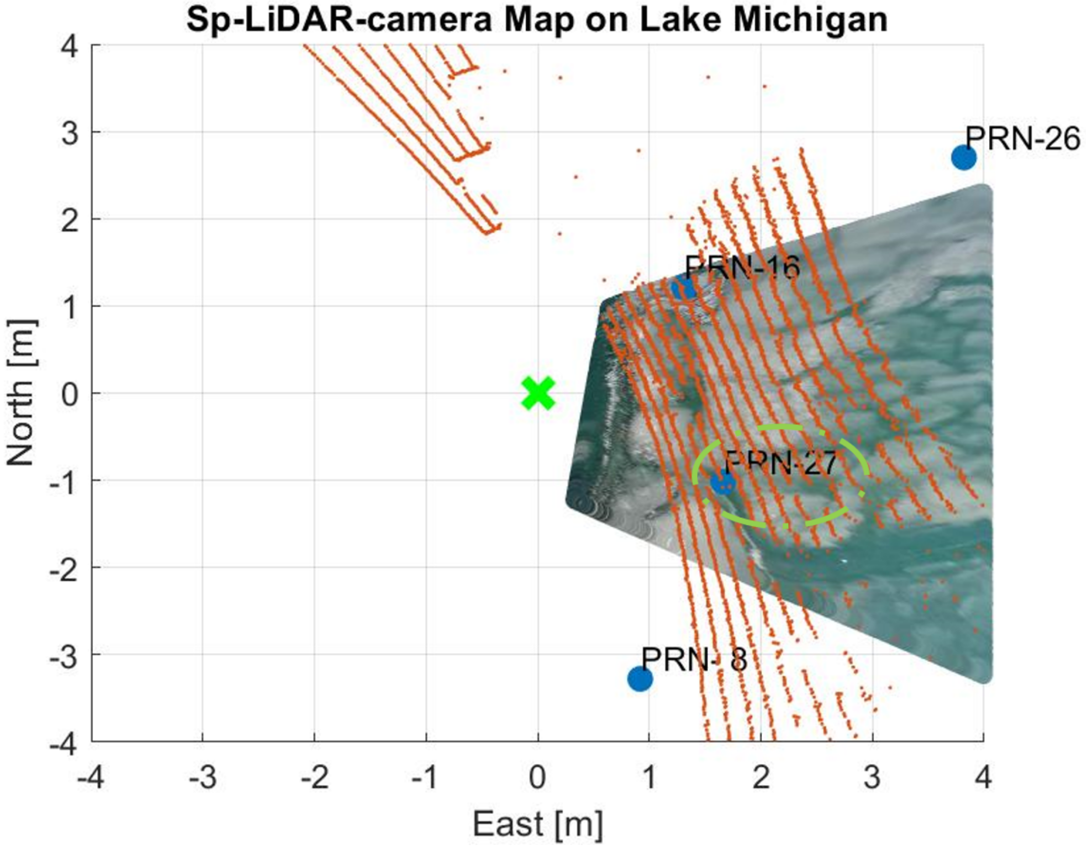

Figure 6.15. SP-lidar-camera maps of Data Campaign 11 at 13:03 CT. Sensor origin is marked with a green cross. Lidar point cloud are orange dots. Camera image from the central camera is projected onto the map in color. Specular points are blue labeled by satellite PRN number.

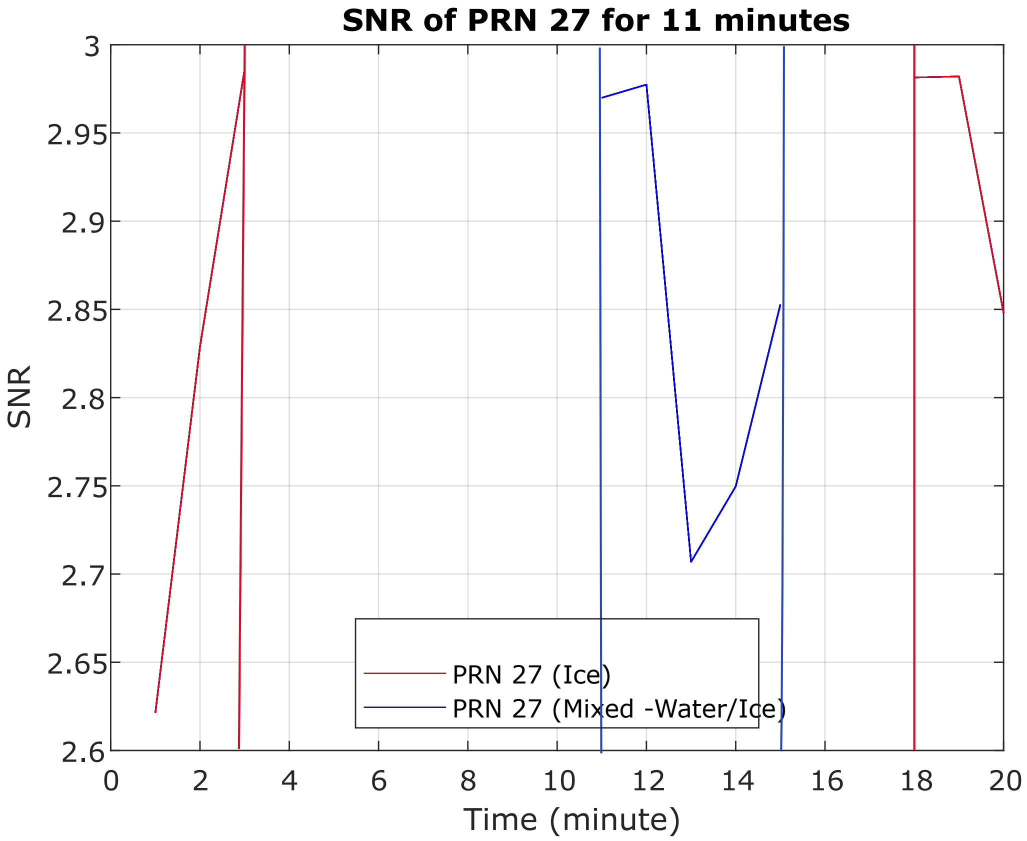

Figure 6.16. Signal-to-noise ratio (SNR) of PRN 27 over time, in minutes since 12:43 CT. Blue indicates times visually identified on the SP-lidar-camera map to correspond to water reflection, and red indicates times corresponding to ice reflection.

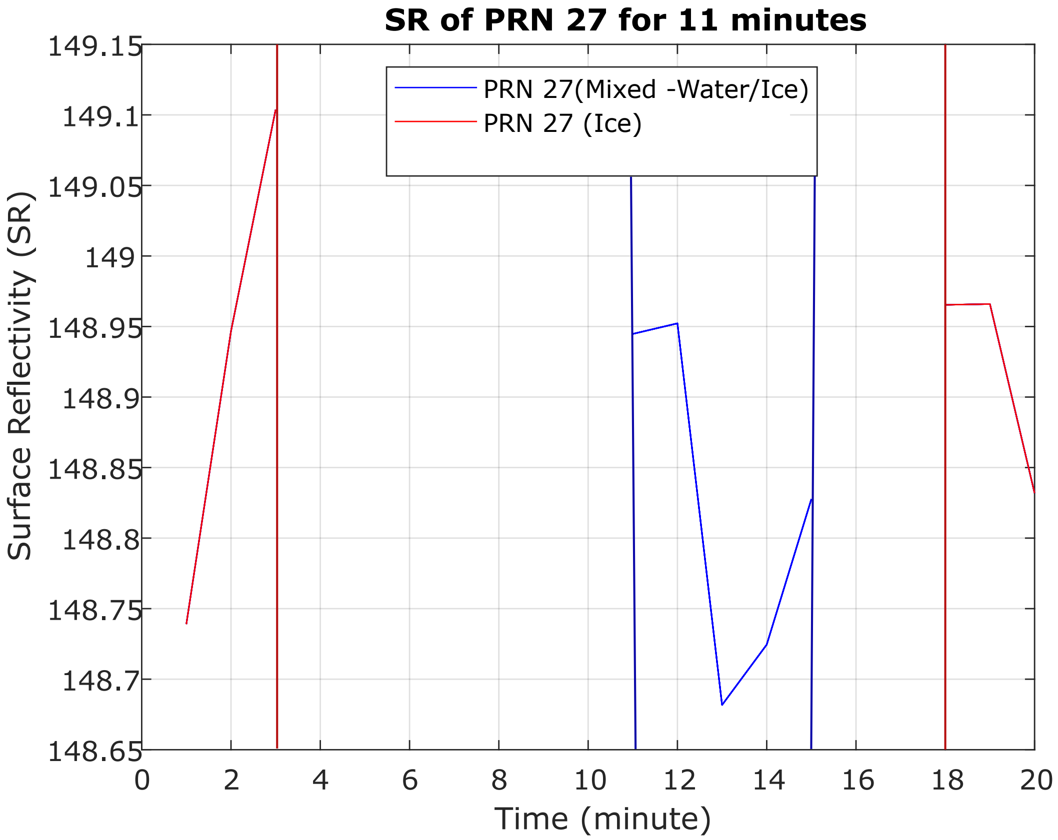

Figure 6.17. Surface reflectivity (SR) of PRN 27 over time, in minutes since 12:43 CT. Blue indicates times visually identified on the SP-lidar-camera map to correspond to water reflection, and red indicates times corresponding to ice reflection.

CHAPTER 7
CONCLUSION

7.1 Summary

This dissertation has presented a system for studying reflected Global Navigation Satellite System (GNSS) signal characteristics for remotely sensing Earth's environment. The portable ground-based system collects GNSS-R signals and auxiliary lidar and camera outputs for correlating reflected GNSS signals to reflection surface type. The system hardware was designed and fabricated, and used for collecting reflections from ice and water surfaces at Lake Michigan. After fieldwork, GNSS-R front-end data were preconditioned for signal processing. New GNSS signal processing for weak GNSS signal detection was developed. GNSS-R signal Delay Doppler Maps (DDM), signal-to-noise ratio (SNR), and surface reflectivity (SR) were computed for different surface types. The main contributions include:

1. development of a hardware sensor suite and software GNSS-R receiver;
2. datasets collected from 11 Lake Michigan field campaigns conducted at 31st St. Beach, Chicago, on the Lake Michigan shore during different seasonal surface conditions;
3. a new GNSS signal processing method for acquiring weak signals, evaluated against existing GNSS signal processing methods for both GNSS direct and reflected signals;
4. the system is demonstrated by using GNSS reflected signals detected from ice and water surface types, as determined by the lidar and camera, to calculate the DDM, SNR, and SR.

Chapter 3 presented a design of the sensor system to collect both GNSS direct and reflected GNSS signals. Two GNSS antennas, one for direct GNSS signals and one for reflected GNSS signals, are used in the sensor suite. To process the GNSS signals, two Universal Software-defined Radio Peripherals (USRP) served as GNSS receivers. To prepare the USRPs for the GNSS-R application, USRPs were tested and evaluated in the lab using a GNSS simulator. USRP outputs are preconditioned before feeding into the GNSS signal processing. For direct GNSS signals, an existing software-defined GNSS receiver (SDR) is used to estimate the sensor location and satellites' position in the sky. Auxiliary sensors include a lidar and cameras; they are collocated with the GNSS antennas to provide a truth reference for the GNSS reflected signals. Auxiliary sensors assist us to identify the surface condition at a GNSS satellite's specular reflection point.

Chapter 4 described the configuration and field conditions for the 11 Lake Michigan data campaigns that were conducted at 31st Street Beach, Chicago, Lake Michigan. Eleven Lake Michigan tests are accomplished during different times of the year to have a variety of lake surface conditions, in particular ice and water. For each data campaign, the date, approximate sensor position and orientation, lidar and camera orientation angles, USRP sampling rate, and surface condition are provided. Also, the objective of each field test is described in this chapter. In this way, the sensor suite is gradually improved by field testing. For example, ground plane size is changed and a bigger ground plane are used for both antennas in Tests 5-11. For data campaigns 1-5, the USRPs' internal clock is used; from Test 6 onward, a GPS-disciplined oscillator (GPSDO) connected to the direct antenna is added to each USRP, for more stable timing and synchronization. Also, from Test 9 onward, two cameras are added to the sensor suite to image more of the lake surface.

Chapter 5 proposed a new GNSS signal processing technique to acquire a weak

GNSS signal for both direct and reflected GNSS signals. A new GNSS signal processing method, Modified differential coherent integration (MDI), is analysed. MDI is evaluated against coherent, incoherent and differential coherent integration using GNSS data acquired from the field tests. The new signal method is evaluated in terms of the number of detected satellites actually present in the sky and signal acquisition metric. Visible satellites are computed using almanac information and sensor position estimated from a Google Map. Given that the visible satellites and their positions in the sky during the test are known, the MDI signal method is analyzed along with other standard methods for both the direct and reflected GNSS signals. With the direct USRP data and 1 ms coheretn integration ($T_{coh} = 1\text{ms}$), MDI acquires more satellites. In the case of the reflected USRP data, only the MDI method is able to detect any satellites. The satellites detected are at high elevation and the reflected antenna points downward so we conclude that the signal detected is reflected from the surface.

Chapter 6 demonstrated different reflected signal properties (DDM, SNR, SR) for different surface types. To this end, specular points of the visible satellites are computed in an east-north-up (ENU) coordinate system centered at the reflected antenna. Then lidar point clouds and camera data are superimposed on the same map, referred to as the SP-lidar-camera map. After an SP-lidar-camera map is generated, satellites whose SPs are verified via lidar and camera images as being on a particular surface type (ice or water) are selected for GNSS-R signal processing. The scattered GNSS signals are a function of the time delay and Doppler frequency. Therefore, for the chosen satellite, the Delay Doppler Map (DDM), which shows the power received as a function of time delay and frequency, is generated. For a high-altitude antenna, the shape of the DDM would tell us about the surface condition and wind speed. However, our system antenna is not tall enough to show any significant spread in power.

Next, the signal-to-noise ratio (SNR) for the selected satellite is computed. Some studies have shown that the SNR of the reflected signals relate to the surface phase change (PRN 16 of test 11). Surface reflectivity also depends on the surface type and is related to SNR, but to estimate the SR the antenna gain pattern must be taken into account. The specular points are transformed into the reflected antenna coordinate system to compute the reflected antenna gain in that direction. With SNR, antenna gain, and satellite distance to the SPs and reflected antenna, the SR for the chosen satellite is calculated.

In both examples over a heterogeneous surface, the surface reflectivity of the ice was greater than that of water, which is expected for L-band signals. This system is a demonstration that SR computed from GNSS-R can be used to map ice and water surfaces.

7.2 Future Work

7.2.1 Weather station synchronization and hardware system improvement.

In this work the weather station temperature, wind speed and direction were collected in the field manually. In future an automated weather station can be synchronized with the other sensors and data stored automatically to enable the system to operate unattended. The weather station information becomes particularly useful in the case of using DDMs to estimate wind speed.

Also, the communications capacity of the sensors connected to the laptop led to occasional buffer overruns that limited continuous collection of no more than 20-minute segments of data. In future, we will try to solve the overflow problem so a user will be able to collect longer data. One solution to the overflow problem may be using a raspberry pi for each USRP since USRPs have higher sample rate. The use of a raspberry pi controller may also eliminate the need for a laptop in the field for data collection.

A new electronics box is being designed for safer and easier operation. Software scripts need to be updated, especially to command all cameras for collecting and saving multiple cameras' images.

7.2.2 Additional data campaigns with mixed ice and water surface conditions. So far 11 Lake Michigan data campaigns have been conducted, the first several of which were for testing the configuration for usability. The later tests had a consistent configuration across the tests, but few days had mixed surface conditions. New data campaigns will be carried out targeting mixed ice and water surface, weather permitting, In future, we will aim to have an opportunity to collect GNSS-R data reflected from the Lake Michigan mixed ice/water surface in a lower multi-path environment (i.e., over the open water instead of in the harbor and docks), and be able to operate the sensor suite for a longer time. Moreover, the sensor suite design will be updated for setting up at sites of interest for cryospheric scientists, such as Antarctica, to study and monitor the ice surface.

7.2.3 Signal processing. To compute the sensor position and satellites' position at the sky, at least 4 visible satellites must be detected in the direct GNSS signal. Since the basic SDR detected fewer than 4 satellites for some of the Lake Michigan data campaigns, almanac information instead of the GNSS direct signals had to be used for those data campaigns for computing the specular points.

The modified differential integration signal processing was studied and evaluated for signal acquisition for both reflected and direct GNSS signals. The GNSS signal tracking section with this new technique will be evaluated, with an eye toward enabling position estimation directly from the direct antenna. Also, the MDI may be a good candidate for tracking weak GNSS signals more generally in other applications.

7.2.4 Additional data analysis. While data from 11 tests were collected, only a small part have been analyzed. In future, the remaining data will be analyzed. The SNR, SR, and DDMs for the entire dataset will be generated and analyzed to develop a GNSS-R ice/water discriminator, particularly for Tests 10 and 11. To this end, the SP-lidar-camera map for the whole data set needs to be created. Then for the satellites whose SPs cross both ice and water over time, the SNR, SR, and DDMs will be analyzed over time. Finally, since our sensor suite's height is low (2 m) in comparison with the GNSS C/A code wave length, it is worth looking into the phase information for possible higher resolution surface characteristics.

APPENDIX A

SPECULAR POINT POSITION

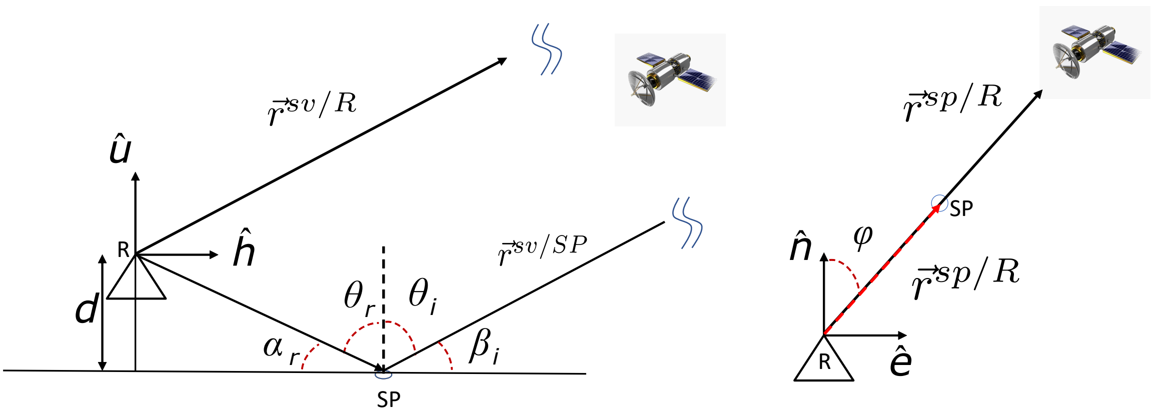

Figure A.1. Geometry for specular point position estimation. Left: side view of the plane of propagation for the specularly reflecting ray. Right: top view of the horizontal plane and position of the satellite and SP.

The direct GPS antenna and receiver may be used to decode the navigation message, estimate the direct antenna position, and compute satellite positions $\vec{r}^{sv/D}$ relative to the direct antenna D. Then the position of the satellite sv relative to the reflected antenna R is:

$$\begin{aligned} \vec{r}^{sv/R} &= \vec{r}^{sv/D} - \vec{r}^{D/R} && \text{(A.1)} \\ &= E\hat{e} + N\hat{n} + U\hat{u} && \text{(A.2)} \end{aligned}$$

where E, N, U are the component distances of the satellite position relative to the reflected antenna's position (lat, lon, alt).

Given $\vec{r}^{sv/R}$, the possible specular points (SPs) $\vec{r}^{sp/R}$ relative to the reflected antenna from satellites in the sky are computed as follows. We assume a horizontal flat Earth, which is reasonable within the few-meter region of interest at the field sites. We also assume a smooth surface for the purposes of SP estimation, and use the law of reflection.

Figure A.1 illustrates the geometry. In the plane of propagation, a 2D coordinate system with horizontal unit vector $\hat{h}$ and vertical unit vector $\hat{u}$ is placed with origin at the reflected antenna (Figure A.1, Left). The position of the satellite relative to this origin is $\vec{r}^{sv/R}$ and is known from Eq. (A.2). The horizontal component of the satellite position is related to components E, N through the azimuth angle ϕ to the satellite (Figure A.1, Right). The position of the specular point $\vec{r}^{sp/R}$ is unknown but will have the same azimuth angle ϕ. Meanwhile, the specular point is on the surface at a height d below the antenna. So, to estimate $\vec{r}^{sp/R}$ we need only the horizontal distance from the antenna to the specular point, $\vec{r}^{sp/R} \cdot \hat{h}$:

$$\vec{r}^{sp/R} = |\vec{r}^{sp/R} \cdot \hat{h}| \sin\phi \hat{e} + |\vec{r}^{sp/R} \cdot \hat{h}| \cos\phi \hat{n} + d\hat{u} \tag{A.3}$$

For specular reflection, the angle of incidence equals the angle of reflection (Eq. (A.4)). Assuming a smooth flat surface, the complementary angles are also equal (Eq. (A.5)). Note that the complementary angle β_i may be considered as the satellite elevation angle as well, since the incoming rays will be almost perfectly parallel (Eq. (A.6)).

$$\begin{aligned}
\theta_i &= \theta_r && \text{(A.4)} \\
\tan\beta_i &= \tan\alpha_r && \text{(A.5)} \\
\frac{|\vec{r}^{sp/R} \cdot \hat{u}|}{|\vec{r}^{sp/R} \cdot \hat{h}|} &= \frac{|\vec{r}^{sv/sp} \cdot \hat{u}|}{|\vec{r}^{sv/sp} \cdot \hat{h}|} \approx \frac{|\vec{r}^{sv/R} \cdot \hat{u}|}{|\vec{r}^{sv/R} \cdot \hat{h}|} && \text{(A.6)} \\
|\vec{r}^{sp/R} \cdot \hat{h}| &= \frac{|\vec{r}^{sp/R} \cdot \hat{u}||\vec{r}^{sv/R} \cdot \hat{h}|}{|\vec{r}^{sv/R} \cdot \hat{u}|} && \text{(A.7)} \\
&= \frac{|d|\sqrt{E^2 + N^2}}{|U|} && \text{(A.8)}
\end{aligned}$$

Equation A.8 gives the horizontal distance to the specular reflection point in terms of the satellite position $\vec{r}^{sv/R}$ and the vertical distance d from the antenna to the reflecting surface. This value is then substituted into Eq. (A.3) for the specular point positions.

APPENDIX B

SURFACE REFLECTIVITY (SR) COMPUTATION

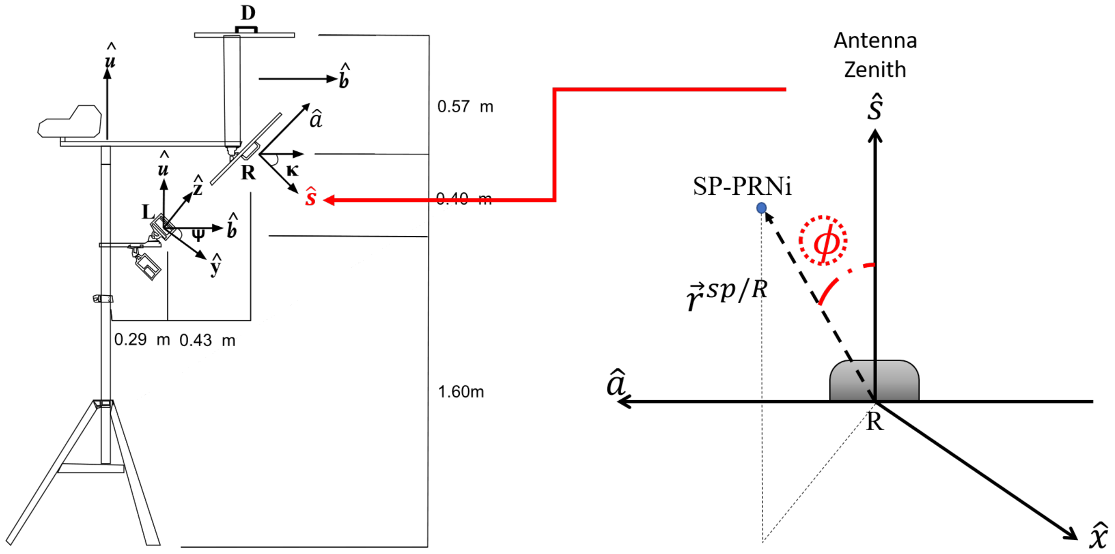

Figure B.1. Left: Boom coordinate system of the tripod $\hat{x}, \hat{b}, \hat{u}$. Right: the reflected antenna coordinate system $\hat{x}, \hat{s}, \hat{a}$ and definition of antenna-zenith angle ϕ.

To compute the reflected antenna gain (G^r in Eq.(6.3)), SPs in the ENU coordinate system of reflected antenna are rotated into the boom coordinate system $\hat{x}, \hat{b}, \hat{u}$, as shown in Figure B.1. Eq.(B.1) indicates the rotation of the SPs from ENU to the boom coordinate system.

$$\vec{r}^{sp/R} = {}^{xbu}\mathbf{R}^{enu}\vec{r}^{sp/R} \tag{B.1}$$

$${}^{xbu}\mathbf{R}^{enu} = \begin{bmatrix} \cos\mu & -\sin\mu & 0 \\ \sin\mu & \cos\mu & 0 \\ 0 & 0 & 1 \end{bmatrix} \tag{B.2}$$

for heading angle μ.

After the SPs are expressed in the boom coordinate system, they are rotated to the reflected antenna's body coordinate system $\hat{x}, \hat{s}, \hat{a}$, shown in Figure B.1(right), using rotation Eq. (B.3).

$$\begin{aligned} \vec{r}^{sp/R} &= {}^{xsa}\mathbf{R}^{xbu}\vec{r}^{sp/R} && \text{(B.3)} \\ {}^{xsa}\mathbf{R}^{xbu} &= \begin{bmatrix} 1 & 0 & 0 \\ 0 & \cos\kappa & \sin\kappa \\ 0 & -\sin\kappa & \cos\kappa \end{bmatrix} && \text{(B.4)} \end{aligned}$$

where κ is the elevation angle of the reflected antenna.

Next, the SP's position vector is mapped into the $\hat{x}, \hat{s}$ plane and ϕ angle for each SP is computed based on Eq. (B.5).

$$\begin{aligned} \hat{r}^{sp/R} &= \frac{\vec{r}^{sp/R}}{||\vec{r}^{sp/R}||} && \text{(B.5)} \\ \hat{r}^{sp/R} \cdot \hat{s} &= \cos\phi && \text{(B.6)} \end{aligned}$$

Based on the ϕ angle of each specular point, the gain of the reflected antenna (Eq.B.7) is computed from Table B.1 derived from the reflected antenna gain pattern [16]).

$$G^r = 42 - Lost; \qquad \text{(B.7)}$$

where 42 dB is the maximum gain of the reflected antenna at zenith.

Table B.1. Gain lost of the reflected antenna based on the Phi angle

Lost (dB)	ϕ degree
3	$0 \leq \phi < 20$
4	$20 \leq \phi < 30$
5	$30 \leq \phi < 40$
6	$40 \leq \phi < 55$
7	$55 \leq \phi < 65$
8	$65 \leq \phi < 70$
9	$70 \leq \phi < 75$
10	$75 \leq \phi < 85$
11	$85 \leq \phi < 90$
14	$90 \leq \phi < 105$
20	$105 \leq \phi < 120$
22	$120 \leq \phi < 140$
30	$140 \leq \phi < 150$
40	$150 \leq \phi < 180$

APPENDIX C

POINT CLOUD PROCESSING

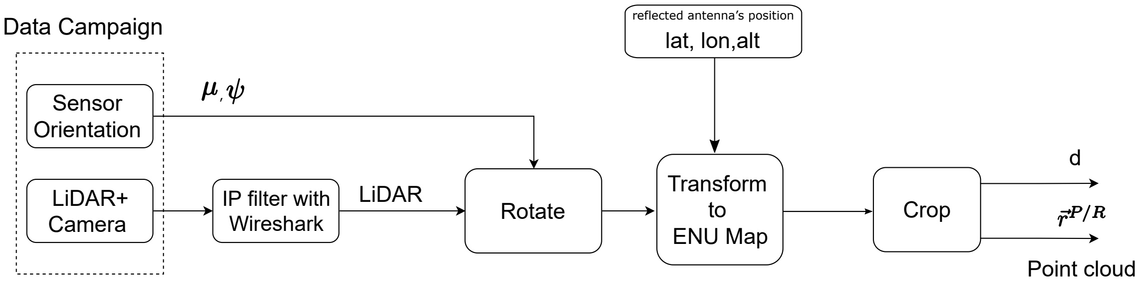

Figure C.1. Lidar processing flowchart

In this section the point cloud, a set of points from which lidar reflections are received, is transformed from lidar body coordinates $\hat{x}, \hat{y}, \hat{z}$ to a local East-North-Up (ENU) system $\hat{e}, \hat{n}, \hat{u}$ whose origin is at the reflected antenna point R as indicated in Figure 4.2. The Velodyne VLP-16 is a 16-channel lidar that has a measurement range of 100 m accurate at ±3 cm, a vertical field of view of ±15° about the lidar body $\hat{x}$ axis, a horizontal field of view of 360° about the $\hat{z}$ axis, and can measure the range and intensity of approximately 300,000 points/second in single return mode. In this work we use the range data.

Figure C.1 describes the lidar processing flow. The lidar elevation ψ and boom heading angle μ are manually recorded upon site setup before each data campaign. A python script starts and ends data collection from all instruments simultaneously. The open source packet analyzer Wireshark records packets of data transferred from the auxiliary-instruments' (i.e., lidar) ethernet switch in pcap format. Using Wireshark, we filter and export the data coming from only the lidar IP address.

We then rotate each point P of the point cloud from the lidar body coordinates $(\hat{x}, \hat{y}, \hat{z})$ to $(\hat{e}, \hat{n}, \hat{u})$, transform to put the origin at the reflected antenna, and crop the data to the desired field of view.

For each position $\vec{r}^{P/L}$ of point P relative to the lidar L, we rotate to $\hat{x}, \hat{b}, \hat{u}$ coordinates as shown in Figure 4.2 using the matrix ${}^{xbu}\mathbf{R}^{xyz}$ with $\psi = -45°$:

$$\vec{r}^{P/L} = {}^{xbu}\mathbf{R}^{xyz}\vec{r}^{P/L} \tag{C.1}$$

$${}^{xbu}\mathbf{R}^{xyz} = \begin{bmatrix} 1 & 0 & 0 \\ 0 & \cos\psi & -\sin\psi \\ 0 & \sin\psi & \cos\psi \end{bmatrix} \tag{C.2}$$

After the data are rotated, we translate the origin to the reflected antenna to give the point cloud positions $\vec{r}^{P/R}$ of points P relative to the reflected antenna R as:

$$\vec{r}^{P/R} = \vec{r}^{P/L} - \vec{r}^{R/L} \tag{C.3}$$

where $\vec{r}^{R/L} = 0.43\hat{b} + 0.4\hat{u}$ m is the position of the reflection antenna R with respect to the lidar L. One more rotation ${}^{enu}\mathbf{R}^{xbu}$ by heading angle μ, which is measured with respect to $\hat{n}$ and defined as positive for angles east of north, gives:

$$\vec{r}^{P/R} = {}^{enu}\mathbf{R}^{xbu}\vec{r}^{P/R} \tag{C.4}$$

$${}^{enu}\mathbf{R}^{xbu} = \begin{bmatrix} \cos\mu & \sin\mu & 0 \\ -\sin\mu & \cos\mu & 0 \\ 0 & 0 & 1 \end{bmatrix} \tag{C.5}$$

Since the lake water level is below the dock, we crop out all the reflection points that are above ground level (i.e., 2 m below the reflected antenna). The heading angle $\mu = 70°$ for test 11 (see Table 4.11)is oriented northward, so we include in the cropped set of points PC only those within 10 meters east or west of the lidar, and points P within 10 m to the north of the LiDAR.

$$\begin{aligned} PC = \{P : \vec{r}^{P/R} \cdot \hat{u} &< -1.6 \text{ m}\} \cap \{P : 0 < |\vec{r}^{P/R} \cdot \hat{e}| < 10 \text{ m}\} \\ &\cap \{P : 10 \text{ m} > \vec{r}^{P/R} \cdot \hat{n} > -10\} \end{aligned} \tag{C.6}$$

To map the specular points' positions on the lake, the height d of the reflected antenna from the water surface is averaged over the cropped point cloud PC:

$$d \;=\; \mathbf{E}(\vec{r}^{P/R} \cdot \hat{u}) \tag{C.7}$$

With d and the lidar point cloud $\vec{r}^{P/R}$, the combined SP-lidar map in an ENU coordinate system can be generated.

BIBLIOGRAPHY

[1] Satellite navigation, wikipedia, GNSS. `https://en.wikipedia.org/wiki/SatelliteNavigation`, May 2015.

[2] Vlp-16u ser manual. Technical report, https://greenvalleyintl.com/wp-content/uploads/2019/02/Velodyne-LiDAR-VLP-16-User-Manual.pdf, 2016.

[3] The science of GPS. `https://www.bliptrackgps.com/science-of-gps.php`, May 2017.

[4] Modis true color images of lake michigan ice coverage 8 marc 2014. `https://coastwatch.glerl.noaa.gov/modis/modis.html`, May 2018.

[5] GPS signals. `https://en.wikipedia.org/wiki/{GPS}signals`, May 2019.

[6] Petr Beckmann and Andre Spizzichino. The scattering of electromagnetic waves from rough surfaces. *Norwood, MA, Artech House, Inc., 1987, 511 p.*, 1987.

[7] Daniele Borio and Dennis Akos. Noncoherent integrations for GNSS detection: Analysis and comparisons. *IEEE transactions on Aerospace and electronic systems*, 45(1):360–375, 2009.

[8] Kai Borre, Dennis M Akos, Nicolaj Bertelsen, Peter Rinder, and Søren Holdt Jensen. *A software-defined GPS and Galileo receiver: a single-frequency approach*. Springer Science & Business Media, 2007.

[9] Jens Bösenberg. Ground-based differential absorption lidar for water-vapor and temperature profiling: methodology. *Applied Optics*, 37(18):3845–3860, 1998.

[10] Centre Tecnològic de Telecomunicacions de Catalunya (CTTC). *GNSS-SDR Input Signal*.

[11] J. Chaput, R. C. Aster, D. McGrath, M. Baker, R. Anthony, P. Gerstoft, and L. Stevens. Near-surface environmentally forced changes in the ross ice shelf observed with ambient seismic noise. *Geophysical Research Letters*, 45, 2018.

[12] Clara Chew, John T Reager, and Eric Small. Cygnss data map flood inundation during the 2017 atlantic hurricane season. *Scientific reports*, 8(1):1–8, 2018.

[13] Weathernews Inc Chihito Kusabiraki. Wnisat-1r. `https://global.weathernews.com/infrastructure/wnisat-1/`, May 2013.

[14] Maria Paola Clarizia. *Investigating the effect of ocean waves on GNSS-R microwave remote sensing measurements*. PhD thesis, University of Southampton, Southampton, October 2012.

[15] Antcom Corporation. P/n: G8ant-3a4tb1. unpublished, unpublished.

[16] Antcom Corporation. P/n: G8ant-3a4tb1. unpublished, unpublished.

[17] S. Datta-Barua, R. Parvizi, E. Donarski, S. Stevanovic, N. Wang, K. Herron, and B. Pervan. Great lake surface characterization with GNSS reflectometry. In *Proceedings of the 29th International Technical Meeting of The Satellite Division of the Institute of Navigation (ION GNSS+ 2016)*, Portland, Oregon, September 2016.

[18] Dariush Divsalar and Marvin K Simon. Multiple-symbol differential detection of mpsk. *IEEE Transactions on Communications*, 38(3):300–308, 1990.

[19] Fabio Dovis, Tung Hai Ta, and J Shuanggen. High sensitivity techniques for GNSS signal acquisition. In *Global Navigation Satellite Systems: Signal, Theory and Applications*. InTech, 2012.

[20] Paulo Esteves, Mohamed Sahmoudi, and Marie-Laure Boucheret. Sensitivity characterization of differential detectors for acquisition of weak GNSS signals. *IEEE Transactions on Aerospace and Electronic Systems*, 52(1):pp–20, 2016.

[21] Ettus Research, https://kb.ettus.com/index.php?title=N200/N210 oldid=2899. *USRP N200/N210.*

[22] F. Fabra, E. Cardellach, A. Rius, S. Ribo, S. Oliveras, O. Nogues-Correig, M. B. Rivas, M. Semmling, and S. D'Addio. Phase altimetry with dual polarization GNSS-R over sea ice. *IEEE Transactions on Geoscience and Remote Sensing*, 50(6):2112–2121, 2012.

[23] Fran Fabra, Estel Cardellach, Oleguer Nogués-Correig, Santi Oliveras, Serni Ribo, Antonio Rius, Maria Belmonte-Rivas, Maximilian Semmling, Giovanni Macelloni, Simone Pettinato, et al. "monitoring sea-ice and dry snow with GNSS reflections. In *Geoscience and Remote Sensing Symposium (IGARSS), 2010 IEEE International*, pages 3837–3840. IEEE, 2010.

[24] R. Pincus National Center for Atmospheric Research Staff(Eds). The climate data guide: Cloud observations from modis. `https://climatedataguide.ucar.edu/climate-data/cloud-observations-modis`, February 2016.

[25] James L Garrison, Stephen J Katzberg, and Michael I Hill. Effect of sea roughness on bistatically scattered range coded signals from the global positioning system. *Geophysical research letters*, 25(13):2257–2260, 1998.

[26] Scott Gleason. *Remote sensing of ocean, ice and land surfaces using bistatically scattered "GNSS" signals from low earth orbit.* PhD thesis, University of Surrey, Guildford, UK, December 2006.

[27] Scott Gleason, Stephen Hodgart, Yiping Sun, Christine Gommenginger, Stephen Mackin, Mounir Adjrad, and Martin Unwin. Detection and processing of bistatically reflected GPS signals from low earth orbit for the purpose of ocean remote sensing. *IEEE Transactions on Geoscience and Remote Sensing*, 43(6):1229–1241, 2005.

[28] Scott Gleason and Christopher Ruf. Overview of the delay doppler mapping instrument (ddmi) for the cyclone global navigation satellite systems mission (cygnss). In *Microwave Symposium (IMS), 2015 IEEE MTT-S International*, pages 1–4. IEEE, 2015.

[29] EP Glennon, AG Dempster, and C Rizos. Feasibility of air target detection using gps as a bistatic radar. *Positioning*, 1(10):0, 2006.

[30] Sinan Hasirlioglu and Andreas Riener. Challenges in object detection under rainy weather conditions. In *First International Conference on Intelligent Transport Systems*, pages 53–65. Springer, 2018.

[31] Jari Iinatti and Ari Pouttu. Differentially coherent code acquisition in doppler. In *Gateway to 21st Century Communications Village. VTC 1999-Fall. IEEE VTS 50th Vehicular Technology Conference (Cat. No. 99CH36324)*, volume 2, pages 703–707. IEEE, 1999.

[32] M. Junered, S. Esterhuizen, D. Akos, and P. Axelrad. A modular GPS remote sensing software receiver for small platforms. In *Proceedings of the 19th International Technical Meeting of the Satellite Division of The Institute of Navigation (ION GNSS 2006*, pages 634–642. IEEE, 2016. Fort Worth, TX, September 2006.

[33] Shahrukh Khan. 3d reconstruction of lake surface usingcamera and lidar sensor fusion. Master's thesis, TIllinois Institute of Technology, 2020.

[34] F. Koch, P. Henkel, F. Appel, L. Schmid, H. Bach, M. Lamm, M. Prasch, J. Schweizer, and W. Mauser. Retrieval of snow water equivalent, liquid water content, and snow height of dry and wet snow by combining GPS signal attenuation and time delay. *Water Resources Research*, 55, 2019.

[35] A. Komjathy, J. Maslanik, V. U. Zavorotny, P. Axelrad, and S. J. Katzberg. Sea ice remote sensing using surface reflected GPS signals. In *Geoscience and Remote Sensing Symposium, 2000, Proceedings*, pages 2855–2857. IEEE, 2000.

[36] Kristine M Larson. Unanticipated uses of the global positioning system. *Annual Rev. Earth and Planet. Sci.*, 47:19–40, 2019.

[37] Kristine M Larson, Johan S Löfgren, and Rüdiger Haas. Coastal sea level measurements using a single geodetic GPS receiver. *Advances in Space Research*, 51(8):1301–1310, 2013.

[38] Kristine M Larson and Eric E Small. Estimation of snow depth using L1 GPS signal-to-noise ratio data. *IEEE Journal of Selected Topics in Applied Earth Observations and Remote Sensing*, 9(10):4802–4808, 2016.

[39] Stephen T Lowe, John L LaBrecque, Cinzia Zuffada, Larry J Romans, Larry E Young, and George A Hajj. First spaceborne observation of an earth-reflected GPS signal. *Radio Science*, 37(1):7–1, 2002.

[40] D. R. MacAyeal. Seismology gets under the skin of the antarctic ice sheet. *Geophysical Research Letters*, 45:11,173–11,176, 2018.

[41] Manuel Martin-Neira et al. A passive reflectometry and interferometry system (paris): Application to ocean altimetry. *ESA journal*, 17(4):331–355, 1993.

[42] Jake Mashburn, Penina Axelrad, Stephen T Lowe, and Kristine M Larson. Global ocean altimetry with GNSS reflections from TechDemoSat-1. *IEEE Transactions on Geoscience and Remote Sensing*, 56(7):4088–4097, 2018.

[43] Pratap Misra and Per Enge. Global positioning system: Signals, measurements and performance second edition. *Massachusetts: Ganga-Jamuna Press*, 2006.

[44] Cillian O'Driscoll. *Performance analysis of the parallel acquisition of weak GPS signals.* PhD thesis, University College Cork, Ireland, January 2007.

[45] R. Parvizi and S. Datta-Barua. Surface ice reflectometry with a dedicated GNSS receiver ii: Signal processing enabling acquisition from reflected signals. under review, N.D.

[46] R. Parvizi, B. Pervan, and S. Datta-Barua. Surface ice reflectometry with a dedicated gnss receiver i: Hardware and field test. under review, N.D.

[47] R. Parvizi, H. S. Zadeh, L. Pan, B. Pervan, and S. Datta-Barua. Multi-sensor study of lake michigan's surface using GNSS-Reflectometry. In *Proceedings of the 31th International Technical Meeting of The Satellite Division of the Institute of Navigation (ION GNSS+ 2018)*, Miami, Florida, September 2018.

[48] Roohollah Parvizi and Seebany Datta-Barua. De-noising GNSS-Reflectometry measurements from a freshwater surface. In *2019 URSI Asia-Pacific Radio Science Conference (AP-RASC)*, pages 1–1. IEEE, 2019.

[49] S. Ribo, J. C. Arco-Fernandez, E. Cardellach, F. Fabra, W. Li, O. Nogues-Correig, A. Rius, and M. Martin-Neira. A software-defined GNSS Reflectometry recording receiver withwide-bandwidth, multi-band capability and digital beamforming. *Remote Sens*, 9:450, 2017.

[50] Maria Belmonte Rivas, James A Maslanik, and Penina Axelrad. Bistatic scattering of GPS signals off arctic sea ice. *IEEE Transactions on Geoscience and Remote Sensing*, 48(3):1548–1553, 2010.

[51] JA Avila Rodriguez, Thomas Pany, and Bernd Eissfeller. A theoretical analysis of acquisition algorithms for indoor positioning. In *Proceedings of the 2nd ESA Workshop on Satellite Navigation User Equipment Technologies NAVITEC*, 2004.

[52] R.Parvizi, J.Henry, N. Honda, E.Donarski, B. S. Pervan, and S. Datta-Barua. Coordination of GNSS Signals with lidar for Reflectometry. In *Proceedings of the 30th International Technical Meeting of The Satellite Division of the Institute of Navigation (ION GNSS+ 2017)*, Portland, Oregon, September 2017.

[53] Surendran K Shanmugam, John Nielsen, and Gérard Lachapelle. Enhanced differential detection scheme for weak GPS signal acquisition. In *ION GNSS*, page 14, 2007.

[54] David E Shean, Knut Christianson, Kristine M Larson, Stefan RM Ligtenberg, Ian R Joughin, Ben E Smith, C Max Stevens, Mitchell Bushuk, and David M Holland. GPS-derived estimates of surface mass balance and ocean-induced basal melt for pine island glacier ice shelf, antarctica. *The Cryosphere*, 11(6), 2017.

[55] MR Siegfried, B Medley, KM Larson, HA Fricker, and S Tulaczyk. Snow accumulation variability on a west antarctic ice stream observed with GPS reflectometry, 2007–2017. *Geophysical Research Letters*, 44(15):7808–7816, 2017.

[56] National Snow and Ice Data Center. What are the limitations of modis data? `https://nsidc.org/support/21553418-What-are-the-limitations-of-MODIS-data`, June 2016.

[57] Elizabeth A Thompson, Nathan Clem, Isaac Renninger, and Timothy Loos. Software-defined gps receiver on usrp-platform. *Journal of Network and Computer Applications*, 35(4):1352–1360, 2012.

[58] James Bao-Yen Tsui. *Fundamentals of global positioning system receivers: a software approach*, volume 173. John Wiley & Sons, 2005.

[59] M Unwin, P Jales, S Duncan, A Palfreyman, C Gommenginger, G Foti, P Moore, J Guo, and J Rosello. *GNSS enabling new capabilities in space on the TechDemoSat-1 Satellite*, 2017.

[60] US. Department of Homeland Security, https://www.navcen.uscg.gov-pageName=GPSAlmanacs. *navigation center-United States Coast Guard.*

[61] B. Legresy Wiehl, M. and R. Dietrich. Potential of reflected gnss signals for ice sheet remote sensing. *Progress In Electromagnetics Research*, 40:177–205, 2003.

[62] Wikipedia, https://en.wikipedia.org/wiki/Electromagnetic-absorption-by-water. *Electromagnetic absorption by water.*

[63] Chun Yang, Mikel Miller, Erik Blasch, and Thao Nguyen. Comparative study of coherent, non-coherent, and semi-coherent integration schemes for GNSS receivers. In *Proceedings of the 63rd Annual Meeting of the Institute of Navigation*, pages 572–588, 2001.

[64] Chun Yang, Thao Nguyen, Erik Blasch, and Mikel Miller. Post-correlation semi-coherent integration for high-dynamic and weak GPS signal acquisition. In *2008 IEEE/ION Position, Location and Navigation Symposium*, pages 1341–1349. IEEE, 2008.

[65] Mohammad H Zarrabizadeh and Elvino S Sousa. Analysis of a differentially coherent spread-spectrum acquisition receiver. In *Proceedings IEEE International Conference on Communications ICC'95*, volume 3, pages 1732–1736. IEEE, 1995.

[66] Mohammad H Zarrabizadeh and Elvino S Sousa. A differentially coherent pn code acquisition receiver for cdma systems. *IEEE Transactions on communications*, 45(11):1456–1465, 1997.

[67] Valery U Zavorotny, Scott Gleason, Estel Cardellach, and Adriano Camps. Tutorial on remote sensing using GNSS bistatic radar of opportunity. *IEEE Geoscience and Remote Sensing Magazine*, 2(4):8–45, 2014.

[68] Valery U Zavorotny and Alexander G Voronovich. Scattering of GPS signals from the ocean with wind remote sensing application. *IEEE Transactions on Geoscience and Remote Sensing*, 38(2):951–964, 2000.